Aerodynamic Development of a Contra-Rotating Shrouded Rotor System for a UAV

by

Heinrich Jacques Geldenhuys

Thesis presented in partial fulfilment of the requirements for the degree of Master of Science in Engineering (Mechanical) in the Faculty of Engineering at Stellenbosch University

Supervisor: Dr S.J. van der Spuy
Co-supervisor: Prof T.W. von Backström

March 2015

DECLARATION

By submitting this thesis electronically, I declare that the entirety of the work contained therein is my own, original work, that I am the sole author thereof (save to the extent explicitly otherwise stated), that reproduction and publication thereof by Stellenbosch University will not infringe any third party rights and that I have not previously in its entirety or in part submitted it for obtaining any qualification.

Signature:

Date:

ABSTRACT

Aerodynamic Development of a Contra-Rotating Shrouded Rotor System for a UAV

H.J. Geldenhuys

Department of Mechanical and Mechatronic Engineering, Stellenbosch University,
Private Bag X1, Matieland 7602, South Africa
Thesis: *MSc. Eng.* (Mech)

March 2015

Unmanned aerial vehicles with vertical take-off and landing capabilities have received extensive attention worldwide in the last decade. Their low detectability, high manoeuvrability in confined spaces, and their capability for out-of-sight operations make them practical solutions for an array of military and civilian missions.

The main advantage of shrouded rotors in hover and low speed conditions is the decreased blade tip induced drag when the tip gap is small enough. A well-designed shroud augments the rotor thrust in hover and low axial flight conditions. It also provides noise reduction and safety. A contra-rotating rotor system eliminates the need for separate anti-torque devices, thus producing a smaller footprint and a more compact vehicle.

In this study a more efficient coaxial rotor for the ducted coaxial rotor system as published by (Lee 2010) was developed.

The first phase of the design process consisted of the selection and numerical analysis of the best suited parent airfoils for the rotors by using XFOIL and XFLR 5.

The second phase dealt with the design of a counter-rotating rotor system for the existing cambered shroud as published by (Lee, 2010), using the DFDC-070ES2a two dimensional code, specifically written for ducted rotor optimization.

The final phase of the study dealt with the Computational Fluid Dynamic (CFD) verification of the design in ANSYS-CFX 15.07.

A comparison between the CFX predictions of the newly designed rotor system and the reference design indicates a 33% improvement in hover thrust at the design power input.

OPSOMMING

Aerodinamiese Ontwikkeling van ‘n Kontra-roterende Gehulde Rotorstelsel vir ‘n Onbemande Lugvaartuig

H.J. Geldenhuys

Departement van Meganiese and Megatroniese Ingenieurswese,
Universiteit van Stellenbosch,
Privaatsak X1, Matieland 7602, Suid-Afrika
Tesis: MSc. Ing. (Meg)

Maart 2015

Onbemande lugvaartuie met vertikale opstyg en landings vermoëns het uitgebreide aandag wêreldwyd in die laaste dekade geniet. Hul lae waarneembaarheid, hoë beweegbaarheid in beperkte ruimtes, en hul vermoë om buite-sig operasies uit te voer maak dat hulle praktiese oplossings vir 'n verskeidenheid van militêre en burgerlike missies is.

Die grootste voordeel van gehulde rotors in hangvlug en lae spoed omstandighede is die afname in die lem punt sleepkrag wanneer die lem punt gaping klein genoeg is. 'n Goed ontwerpde omhulsel dra by tot die rotor stukrag in hangvlug en lae aksiale vlug omstandighede. Dit bied ook geraasreduksie en veiligheid. 'n Kontra-roterende rotorstelsel skakel die vereiste van afsonderlike anti-wringkrag toestelle uit, wat lei tot 'n kleiner voetspoor en 'n meer kompakte voertuig.

In hierdie studie is 'n meer doeltreffende koaksiale rotor vir die gehulde koaksiale rotor stelsel soos gepubliseer deur (Lee 2010) ontwikkel.

Die eerste fase van die ontwerp-proses het bestaan uit die seleksie en numeriese analise van die mees geskikte lemprofiele vir die rotors deur die gebruik van XFOIL en XFLR 5.

Fase twee het die ontwerp van 'n teen-roterende rotor stelsel vir die bestaande omhulsel soos gebruik in (Lee, 2010) se publikasie behels. Die ontwerp is met behulp van DFDC-070ES2a, ‘n twee dimensionele kode wat spesifiek vir gehul-rotor optimering geskryf is, gedoen.

Die verifikasie van die nuwe ontwerp is in die finale fase met behulp van die berekeings vloeidinamika sagteware, ANSYS-CFX 15.07 gedoen.

‘n Vergelyking tussen die CFX prestasie voorspelling vir die nuwe rotorstelsel en die gepubliseerde data van (Lee, 2010) toon ‘n 33% toename in hangvlug stukrag by die ontwerpsdrywing.

ACKNOWLEDGEMENTS

My sincere thanks are due to several people, without whom the lessons that I have learned during this research would never have occurred;

My wife, Lucresia. You are my most precious gift. Thank you for your unselfish support and encouragement.

My supervisors, Dr S.J. van der Spuy and Prof T.W. von Backström for their insight and continued support throughout the time of my study.

Heartfelt thanks to my friend, Bosman van der Merwe. He has been an irreplaceable source of advice and inspiration. This work would not have been possible without his valuable contributions.

Philip Carter, the founder and owner of Esotec Developments, Madeira Park, BC, Canada, for your help and constant guidance with the Ducted Fan Development Code (DFDC).

My sincere thanks to my wonderful family for their support and encouragement.

Lastly, eternal thanks to God – to Him be the glory.

CONTENTS

page

TABLES

FIGURES

page

page

ACRONYMS AND ABBREVIATIONS

AFDD	Aero Flight Dynamics Directorate
AoA	Angle of attack
ATE	Advanced Technologies and Engineering
BEMT	Blade element momentum theory
BET	Blade element theory
CFD	Computational Fluid Dynamics
CSCRS	Cambered Shroud Coaxial Rotor System
DFDC	Ducted fan design code
DL	Disk loading = Trotor/A
FM	Figure of merit = Pi/P
FVM	Finite volume method
GGI	General grid interface
IMT	Institute of Maritime Technology, Simon's Town, South Africa
LADF	Lift augmented ducted fan
L/D	Lift to drag ratio
MAV	Mini aerial vehicles
MIT	Massachusetts Institute of Technology
MRF	Multi reference frame
MUAV	Mini UAV
NACA	National Advisory Committee for Aeronautics
NASA	National Aeronautics and Aerospace Administration
PL	Power loading = T/P
RMS	Root mean square residual
SCRS	Shrouded coaxial rotor system
SDR	Shrouded/ducted rotor
SLADe	Surface launched aerial decoy
SST	Shear stress transport
UAV	Unmanned aerial vehicle
VTOL	Vertical take-off and landing
V/STOL	Vertical/short take-off and landing

NOMENCLATURE

A	rotor disk area or shroud throat cross-sectional area $= \pi \left({D_t}/{2}\right)^2$
A_R	rotor disk area, corrected for blade root cut-out $= \pi(R^2 - R_0^2)$
A_e	diffuser exit area
a	airfoil lift-curve slope = $dCL/d\alpha$
CL	lift coefficient = L/_A(R)2
C_d	2D drag coefficient
C_l	2D lift coefficient
$\tilde{C}_l$	corrected two dimensional lift coefficient of the blade-element
C_P	power coefficient = $\frac{P}{\pi R^2}$
C_T	thrust coefficient = $\frac{T}{\pi R^2}$
c	rotor blade chord
c_d	shroud/duct chord
D	drag
D_R	rotor diameter
D_t	shroud throat diameter (minimum inner diameter)
J	propeller advance ratio = v1/nDR
$K_{1\ldots4}$	Küchemann constants
L	lift
L_d	shroud diffuser length
M	Mach number
ṁ	mass flow = ρAv
N_b	number of blades
n_{crit}	transition criteria in XFOIL
n	rotor rotational speed, rev/s
p	local static pressure
p_{atm}	ambient atmospheric pressure
P	rotor shaft power = Pi + Po = actual power
P_i	ideal/induced power
P_0	profile power
P_z	wake helical pitch
Q	rotor torque
R	shroud/duct radius
R	rotor radius = $\frac{D_R}{2}$
R_i	shroud/duct inner radius
R_m	shroud/duct outer radius
R_0	rotor blade root cut-out
Re	Reynolds number
r	non-dimensional radial coordinate = y/R
T	thrust
T_{total}	total shrouded-rotor thrust = T_{rotor} + T_{shroud}
t/c	thickness to chord ratio
t_d	shroud wall thickness
U	resultant velocity at rotor blade element
U_R	radial component of velocity at rotor blade element
U_T	tangential component of velocity at rotor blade element
V_c	climb velocity
V_F	flight velocity
v	induced velocity at rotor plane
v_i	(ideal) induced velocity at rotor plane
w	induced velocity in far wake of rotor

w_a	axial component of the induced velocity on the helical pitch in far wake of rotor
w_t	tangential component of the induced velocity on the helical pitch in far wake of rotor
Y	the wake contraction coefficient
y	radial coordinate
z	axial coordinate, positive downstream from rotor

Greek symbols

α	effective angle of attack; blade element aerodynamic angle of attack
δ_{tip}	blade tip clearance
θ_d	diffuser angle
ϕ	induced inflow angle
κ	induced power correction factor; Goldstein's coefficient of interference velocity
λ	advance ratio in the far wake
λ_i	induced inflow ratio = $v_i/(\Omega R)$
Ω	rotor rotational speed, rad/s
ρ	air density
μ	viscosity
ν	kinematic viscosity
ω	induced velocity in far wake of rotor
σ	rotor solidity = $N_b c/(\pi R)$
σ_d	shroud diffuser expansion ratio $= \frac{A_e}{A}$
σ_d^*	expansion ratio, corrected for rotor hub blockage $= \frac{A_e}{A_R} = \frac{\sigma_d}{\left(1-\left(\frac{R_0}{R}\right)^2\right)}$

Subscripts

OR or IR	refers to open (un-shrouded or isolated) rotor
SR	refers to Shrouded Rotor
c	refers to value in the climb condition
h	refers to value in the hover condition
i	refers to the shroud interior
inlet	refers to component due to shroud inlet
m	refers to the shroud exterior
rotor	refers to component due to rotor
shroud	refers to component due to shroud
l	lower
u	upper

Model Parameter Nomenclature

C	cambered shroud
L	lower rotor
P1	upper rotor at a distance of 0.10*cd* from the shroud leading edge
P2	upper rotor at a distance of 0.33*cd* from the shroud leading edge
P3	lower rotor at a distance of 0.67*cd* from the shroud leading edge
P4	lower rotor at a distance of 0.90*cd* from the shroud leading edge
R	rotor loads only
S	symmetric shroud
S1	0.15*R* rotor-to-rotor spacing
S2	0.20*R* rotor-to-rotor spacing
S3	0.30*R* rotor-to-rotor spacing

S4	0.35*R* rotor-to-rotor spacing
T	total loads
TG1	Tip Gap = 0.01R
TG3	Tip Gap = 0.03R
U	upper rotor

CHAPTER 1: INTRODUCTION

1.1 BACKGROUND

This thesis documents the aerodynamic development of a contra-rotating shrouded rotor system for unmanned aerial vehicles (UAVs).

Unmanned aerial vehicles and mini aerial vehicles (MAVs) with vertical/short take-off and landing (V/STOL) capabilities have received extensive worldwide attention in the last decade. Their low noise signature, low detectability, high manoeuvrability in confined spaces and their ability to perform out-of-sight operations, make them practical solutions for an array of military and civilian missions. Their potential applications are mainly in the field of dangerous missions where manned flight would be either unfeasible or uneconomical. These missions could include visual reconnaissance, biological, chemical or nuclear agent sensing, communications relay, ship decoys, border patrol, traffic monitoring, meteorological studies and power-line inspections (Ko et al., 2007).

In South Africa, the firm Advanced Technologies and Engineering (ATE) produces the 5.2 meter wingspan Vulture reconnaissance UAV while Denel Dynamics, a division of Denel, produces the Seeker II+ and the updated Seeker 400 tactical UAV surveillance systems with a wingspan of approximately 4.4 meters. These systems operate at ranges of up to 250 km from their base and can be used for real-time day and night surveillance, target location, artillery fire support, electronic intelligence, border patrol and marine patrol. Denel Dynamics also produces the Hungwe catapult-launched and skip-landed UAV real-time communication system, enabling communication up to 100 km from its base (Denel, 2014).

The definition of small UAVs is somewhat arbitrary, but vehicles with a wing span of less than approximately 6 m and a mass less than 25 kg are usually considered in this category. Low altitude UAVs are typically required to operate at flight speeds between 0 and 100 km/h at altitudes that may vary from 3 to 300 m in all weather conditions for a couple of hours.

Figure 1.1 shows the relation between the total mass and wing chord Reynolds number (Re) for flight vehicles, where the wing chord Re is defined as the cruise speed multiplied by the mean wing chord divided by the kinematic viscosity of the air. Figure 1.2 illustrates the mass versus wingspan for various flight vehicles. It is clear that the small UAV regime, which includes the MAVs, is well below that of conventional aircraft (Mueller & DeLaurier, 2003).

The definition of mini and micro UAVs varies according to different sources, but generally a mini UAV (MUAV) has a wing span between 0.305 and 2.5 m and weighs in the order of 1 to 10 kg. Micro aerial vehicles (MAVs) refer to a size less than 0.15 m in length, width and height. They weigh roughly 100 g and have an endurance of approximately one hour. Whether mini or micro vehicles, all of them are:

- Small, lightweight and portable and can be deployed and controlled remotely by a single person.
- They are fully autonomous or semi-autonomous or remotely controlled and as such eliminate the need for a human to be on site.

- Lastly, they are inexpensive and dispensable or easy-to-repair vehicles that carry the dedicated sensors required for their specific civilian or military mission (Kotwani, n.d.).

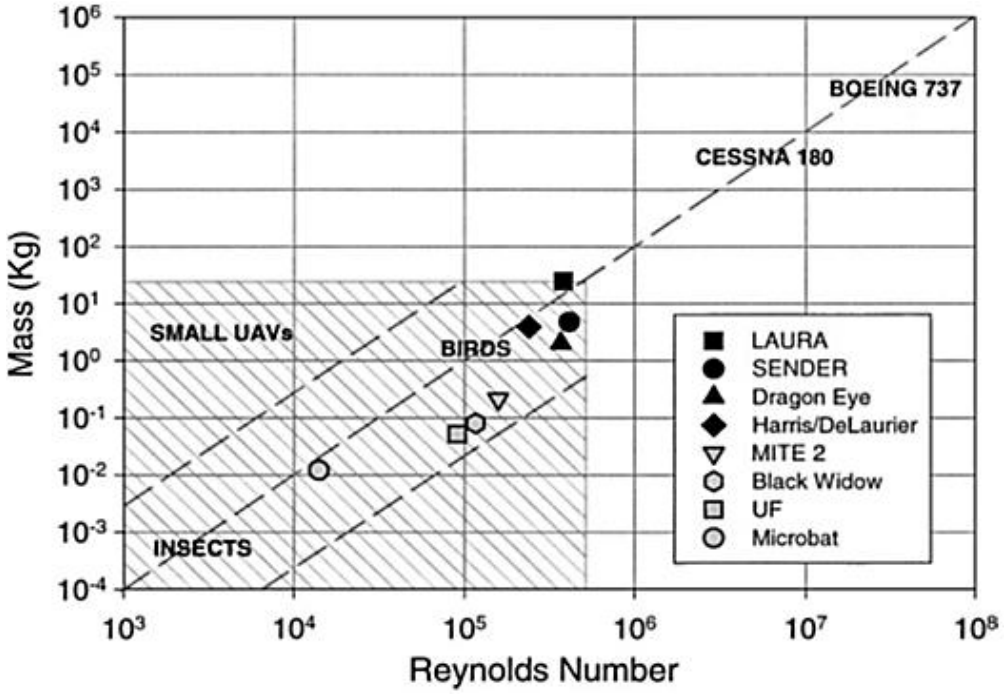

Figure 1.1: Mass versus Reynolds number range for flight vehicles (Mueller & DeLaurier, 2003).

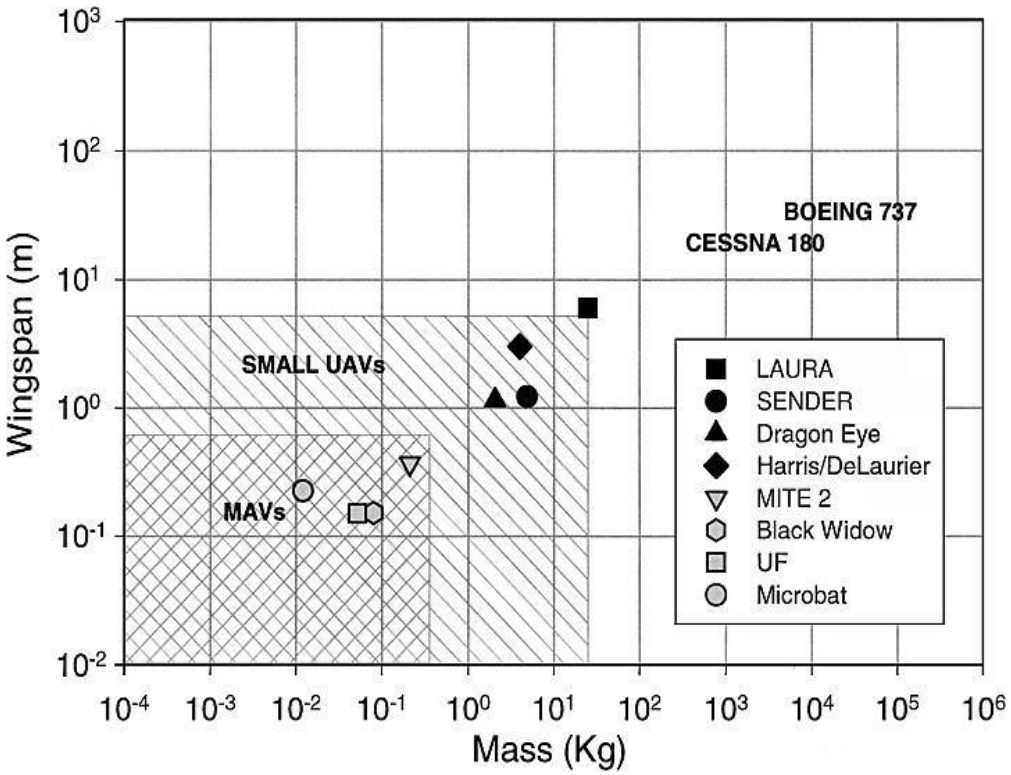

Figure 1.2: Wingspan versus mass for small UAVs and MAVs (Mueller & DeLaurier, 2003).

The configuration of existing MAVs may be classified as: fixed wing; flapping wing; tilt-rotor; and vertical take-off and landing rotary wing MAVs.

The fixed-wing MAVs were the first to be developed, of which the Black Widow is an example (Kotwani, n.d.). The conventional fixed-wing configuration will be superior when the task at hand involves outdoor missions over longer distances or for longer flight durations, such as monitoring traffic, forestry and wild-life surveys, and border surveillance.

The flapping wing MAVs are inspired by insect-based flight. These vehicles cannot hover and are mechanically very complex to manufacture. There is a great deal of wear and tear on the components caused by the high frequency back-and-forth motion of the wings. Recently Aerovirnoment designed and tested their Nano Hummingbird, shown in Figure 1.3. It is capable of agile manoeuvring, has a low noise signature, weighs 19 g and has a hover endurance of 11 minutes (Hrishikeshavan, 2011).

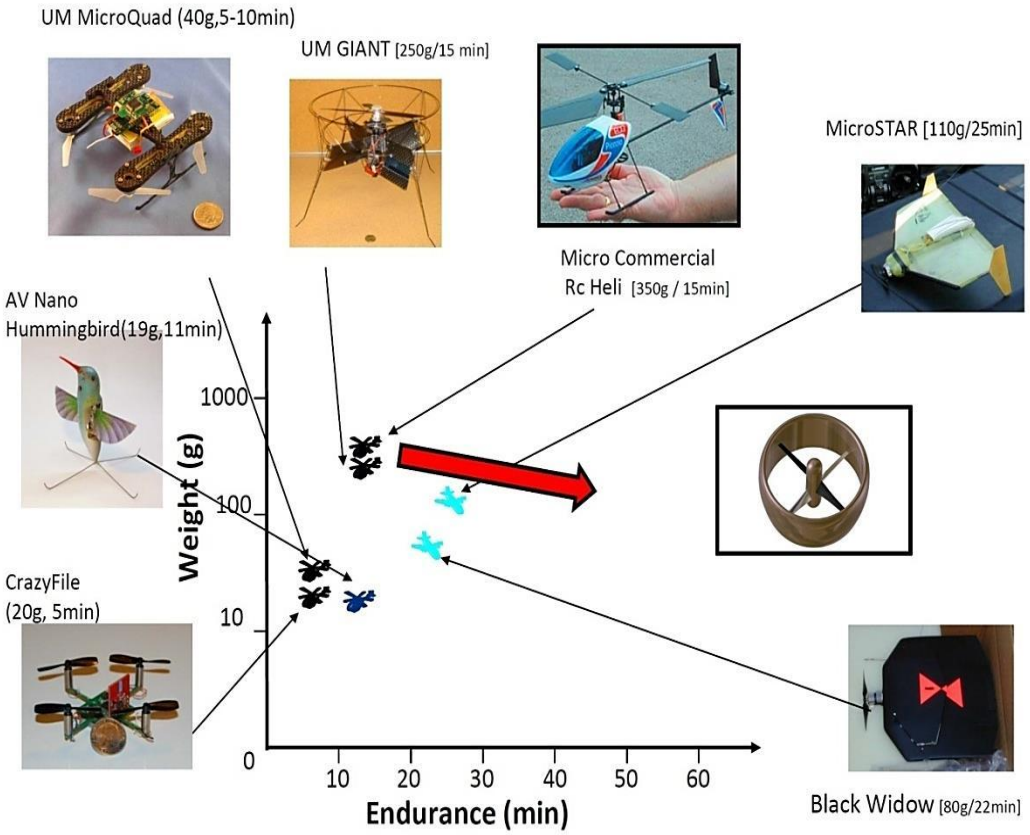

Figure 1.3: Endurance of existing micro air vehicles (Hrishikeshavan, 2011).

The tilt-rotor UAV has the ability to hover directly over a target and to fly at high speeds. Bell Helicopters, a US company, has done a lot of research on tilt-rotor UAVs, but the researchers at the Korea Aerospace Research Institute did extensive studies, using computational fluid dynamics, to investigate the rotor performance and the rotor wake of the tilt-rotor UAV to improve the aircraft's stability and air speed (Miller *et al*., 2006).

The VTOL rotary wing MAVs, with their ability to "perch and stare" for extended periods of time with a low risk of being detected during tactical reconnaissance and surveillance missions, make the rotary wing configurations very attractive.

Some of the many rotary wing MAVs that have been developed are the micro commercial helicopter, the Crazyfile quad rotor and micro coaxial rotors. These vehicles operate in the low Re flow regime (between 10^4 and 10^5) where the highly viscous and separation prone flow conditions result in a low hover endurance. The flight mechanics of these vehicles are inherently unstable due to considerable cross coupling in lateral and longitudinal motions.

1.2 THE PERFORMANCE OF SMALL SCALE ROTORS

The figure of merit (FM) and power loading (PL) values are two metrics used to compare the performance of various rotary wing and VTOL MAV designs.

The rotor FM is given by:

$$FM = \frac{Ideal\ power\ required\ to\ hover}{Actual\ power\ required\ to\ hover} = \frac{P_{ideal}}{Induced\ power + Profile\ power} \tag{1.1}$$

where the actual power supplied to the rotor is the sum of the induced power and the profile power. The Ideal power is given by the simple momentum theory which assumes no viscous losses and is thus entirely induced in origin. The induced power compensates for the non-uniform flow with compressibility, swirl, the tip losses and a finite number of blades. The profile power is determined by the power required to overcome the drag on the rotor blades. In reality, the viscous effects are present in the induced power and profile power contributions and are thus always present in the actual power measurements. (Leishman, 2006).

The PL is the ratio of the thrust to power required to hover and is often expressed in terms of the rotor FM, air density and disc loading (DL is the ratio of thrust to rotor disc area) or in terms of the thrust and power coefficients (Leishman, 2006):

$$PL = \frac{T}{P} = FM\sqrt{2\rho/DL} \tag{1.2}$$

Studies done by Pines and Bohorquez (2006) indicated that the FM of full scale rotors is between 0.75 and 0.90 whereas the values for MAVs are between 0.60 and 0.75. It was found that the profile power (P_o) for full scale rotors is in the order of 30% whereas this value is closer to 45% at the MAV scale. C_P/C_T values between 12 and 14 can be expected for full scale rotors, while the maximum values at MAV scale are between 5 and 6.

Currently the rotor-based hovering platforms are the most advanced. The coaxial configuration is more compact than the conventional single main rotor with a tail rotor and the quad rotor configurations, but they can be less efficient in hover due to the aerodynamic interference between the rotors. It is thus important to investigate the shrouded coaxial rotor systems for MAVs to improve their compactness and efficiency.

1.3 THE SHROUDED/DUCTED ROTOR (SDR) CONFIGURATION

The iSTAR, developed by Allied Aerospace and shown in Figure 1.4, is an example of an SDR-VTOL MAV that uses a lift augmented ducted fan (LADF).

A shroud or duct, also known as a ring-wing or an annular airfoil, is the main lifting surface of a ducted fan vehicle. The shroud consists of an inlet and a diffuser section. The diffuser recovers the kinetic energy of the slipstream and increases the mass flow rate through the rotor. The rotation of the rotor causes a

low pressure above the rotor plane, which accelerates the flow over the shroud inlet surface. This causes a low pressure over the shroud inlet area which results in an added lift force.

The geometry is formed by revolving an airfoil cross section about an offset centreline (Ko *et al*., 2007). The terms, “ducted-fan” and “shrouded-propeller” are used interchangeably. Normally a “duct” has a length that is equal to or longer than its diameter - it has a low width-to-length ratio. Shorter “ducts” are referred to as “shrouds” and have a high width-to-length ratio. In the same way a “fan” normally has five or more blades, whereas a “propeller” generally has four or fewer blades. Each blade of a propeller, rotor or fan is essentially a rotating wing, twisted and varying in airfoil section from root to tip to achieve maximum efficiency in the generation of lift. Propellers are commonly used to convert the power of an aircraft engine into a propulsive force in a forward direction, namely thrust.

Figure 1.4: iSTAR SDR-VTOL MUAV (Kotwani, n.d.).

Rotors generally rotate in approximately a horizontal plane about a common axis which produces upwards lift and forward thrust for hovercraft.

The main difficulty with rotary wing vehicles is to achieve better performance because of the large amount of power required to hover. Hover is an inherently high power flight state with considerably larger energy requirements than cruise for fixed wing vehicles where the lift generated by the wings in forward flight equals the weight of the craft. If a significant part of a mission involves stationary flight, hover efficiency becomes a key vehicle requirement.

In South Africa, the need for a small surface launched aerial decoy (SLADe) was identified by The Institute of Maritime Technology (IMT) in Simon’s Town. A SCRS-VTOL MUAV was developed in 2006 under the guidance of Prof Thomas Jones of the Electrical and Electronic Engineering Department of Stellenbosch University to serve as a technology demonstrator for SLADe. The focus of the project was primarily on the control system design and as such the development of the technology demonstrator was successful, but the aerodynamic design was not optimised. The details of the development of the initial technology demonstrator can be found in an article by Heise *et al*. (2006). In 2007 Dr S.J. van der Spuy, under the guidance of Prof T.W von Backström, evaluated the

existing SLADe demonstrator and suggested that, amongst others, the coaxial rotor system could be redesigned to improve the aerodynamic efficiency of the demonstrator (Van der Spuy & Von Backström, 2007). Unfortunately the SLADE demonstrator was damaged beyond repair shortly after the evaluation.

In an investigation done by Bohorquez (2007), initial hover rotor testing showed that small-scale rotors with airfoils and blade geometries similar to those of full-scale vehicles had a maximum FM in the vicinity of 0.35. Given that full-scale helicopters can reach maximum FMs in the order of 0.8, this is a very low value. However, since efficiency depends largely on airfoil characteristics, such as the L/D ratios, it is expected that the low Reynolds number sub-scale MUAV rotors will have a lower hovering efficiency than full-scale ones. In order to improve these numbers it will not only be necessary to consider two-dimensional airfoil characteristics, but the complete rotor design. Blade parameters such as taper, twist and collective will have to be modified for the vastly different flow conditions.

The hovering shrouded/ducted rotor system (single or coaxial) is normally more aerodynamically efficient than a single rotor system since additional duct forces increase the rotor performance (Lee, 2010). The SDR configuration for VTOL MAVs and MUAVs has proved to be a popular design and offers the following potential advantages:

- The shroud augments the lift/thrust produced by the rotor, which is crucial for these miniature class vehicles. A carefully designed shroud/duct augments static thrust by about 10% over that produced by an open rotor of the same diameter (Heise *et al*., 2006).
- The shroud protects the rotor from tip strikes, thus improving ruggedness and making it safer for people operating it in confined areas.
- The shroud dampens the noise of the rotor considerably since a shrouded propeller can be run under optimum flow and loading conditions, eliminating propeller-tip "buzz," which is a large component of propeller-driven aeroplane noise.
- The shroud/duct can be used to support the rotors and vanes. It can also serve as a housing for various avionics, sensors, the propulsion system, fuel, payload and other equipment.

One of the reasons for the thrust increase in SDRs is the small tip clearance between the rotor tips and the shroud, which results in reduced tip losses and thus an increase in thrust. In a cleverly designed shroud the upstream and slipstream flow of the rotor may cause a pressure distribution on the shroud that can result in additional thrust or lift. For a given rotor, this extra force will depend on parameters such as the size and profile of the shroud, the tip clearance of the rotor as well as its location along the vertical axis of the shroud (Kotwani, n.d.).

One of the biggest disadvantages to the use of a shroud on a rotating-wing platform is the extra weight of the shroud itself. Extra care must also be taken to ensure a sufficient clearance between the rotor tip and the shroud wall to avoid possible blade strikes. The aerodynamic benefits of shrouding are the greatest in hover, and may not necessarily render improvements in forward flight.

A major advantage of the contra-rotating coaxial rotor system is that it does not require a separate means of anti-torque, since the rotor torques offset each other. This results in a smaller footprint compared to conventional rotorcraft that require a tail rotor for anti-torque. Vehicle compactness is improved, since the disc area of each rotor in a contra-rotating system may be smaller than for a single rotor system in a vehicle with the same weight and disc loading.

In contrast, the rotor-to-rotor aerodynamic interference with the coaxial system is likely to increase the net power requirements, dictating a bigger power source for the same thrust, which reduces the available payload, endurance, range and overall capability for the same vehicle weight. The more complex rotor hub for the coaxial system will also increase the vehicle weight and ultimately raise the maintenance costs.

In order to make a final decision on the suitability of a shrouded contra-rotating configuration for a UAV, the potential benefits of greater aerodynamic efficiency, vehicle ruggedness and compactness must be weighed against the decreased vehicle capability resulting from higher structural weight requirements.

1.4 PREVIOUS RESEARCH OF SHROUDED ROTOR SYSTEMS

Early research on larger scale shrouded propellers and ducted fans done by Krŭger (1949) and Sacks & Brunell (1962) led to a better understanding in this field. The National Aeronautics and Aerospace Administration (NASA) was involved in extensive research on the full scale 1.219 m (4 ft) diameter ducted propeller of the Doak VZ-4DA. Yaggy & Mort (1961), Yaggy & Goodson (1960) and Mort (1965) documented numerous experiments on the performance of the ducted propeller by changing the incidence angles with regard to the free stream in hover and forward flight. These experiments indicated a maximum propulsive efficiency of 0.60 at an advance ratio (J) of 0.6 and a maximum FM of 0.78 at blade angles between 11° and 20°.

Platt (1948) performed static tests on 1.219 m (4 ft) diameter shrouded and isolated counter rotating propellers. Three different shrouds that varied in length and diffuser angle were used. The power consumption for all the tests was within 10% of each other, but the shrouded propellers produced nearly twice the thrust of the unshrouded propellers. Alterations in the diffuser angle and shroud length had little effect on the performance of the shrouded propellers. Further wind tunnel experiments were done by Mort and Gamse (1967) on the 2.134 m (7 ft) diameter ducted propeller of the Bell X-22A tilt rotor. They found a maximum FM of 0.81 and a maximum propulsive efficiency of 0.74. They reported a decrease of nearly 20% in thrust when the tip clearance was increased. Mort and Gamse (1967) indicated that the design criteria of a shrouded propeller in axial flight and in hover flight are normally in conflict.

An extensive investigation on the effects of various duct parameters was done by Black *et al.* (1968). They used twelve different duct models on a 0.762 m (30 inch) diameter propeller to investigate the effects of the duct chord, lip shape, duct external shape, blade tip clearance, the position of the propeller in the duct, the number of blades and the exit expansion ratio. They obtained up to 67% increase in thrust for the same ideal power and found that the duct exit expansion ratio was the overriding shrouded propeller variable. Their investigation indicated that shroud performance is increased by increasing the rotational speed of the rotor or by increasing the blade angle of attack, since this resulted in higher suction forces on the shroud inlet. The shroud performance deteriorated in axial flow due to the drag from the shroud and the fact that the slipstream contraction, which is extensive at static conditions for the isolated rotor, becomes less pronounced at higher flight speeds.

The theoretical ideal thrust produced in static conditions by a shrouded propeller with an expansion ratio of unity is 26% more than for the same isolated propeller, with the thrust produced by the rotor and the shroud being approximately equal. With larger expansion ratios, the ideal static thrust growth increases as the cube

root of the ratio. Black *et al*. (1968) found that, depending upon the duct design, a shrouded rotor with a 30% to 40% smaller diameter would produce the same thrust as the isolated rotor. Lower duct expansion ratios were required in axial flow. Their investigation indicated that positioning the propeller forward in the duct resulted in better performance in axial flight whereas a rearward position is preferred in static conditions.

With the focus on UAV development, research was done on smaller scale shroud rotor systems. Experiments on a shrouded counter rotating rotor system done by Cycon, Rosen & Whyte (1992) indicated that performance increased with an increase in the shroud leading edge radius. Varying the shroud length from 100% shroud throat diameter (D_t) to 5% (D_t) resulted in a thrust reduction of only 10%, which is important in terms of weight-saving considerations.

Martin and Tung (2004) experimented on a 10 inch diameter shroud rotor model using two different shroud shapes to investigate the effects of leading edge radius. The tip gap on each shroud could also vary between 1% and 4% rotor radius (R). A 37% increase in thrust over the isolated rotor was measured when they used the shroud with the highest leading edge radius and the smallest rotor tip gap. With the rotor tip shroud gap at 4% R the FM was 0.44 which was close to the value for the open rotor. At low propeller rotational speed the shroud resulted in a negative thrust on the system which was caused by the internal flow losses in the shroud at low Re.

Martin and Boxwell (2005) did additional experiments on a 10 inch diameter shrouded rotor model using two new shroud internal shapes, with changes near the rotor tip path plane, to further investigate the effect of rotor tip gap on hover performance. The one shroud had a stepped internal geometry while the other had a notch for the rotor tip. Their experiments indicated that for the same power, the stepped shroud delivered less thrust while the notched shroud delivered the same amount of thrust as the original shroud.

Pereira and Chopra (2009) did thorough investigations on the performance of a 0.16 m (6.3 inch) ducted rotor MAV. Performance gains in static conditions of up to 50% were obtained with optimal settings for the inlet leading edge radius. tip gap, diffuser length (50% D_t) and diffuser angle (10°). It was found that about 80% of the duct thrust was generated by the inner half of the inlet lip.

Lee (2010) did extensive experiments on the shrouded counter rotating rotor system indicated in Figure 1.5, where better static performance was recorded with the rotors positioned further down within the shroud. The hover performance of the shrouded coaxial rotor system was more sensitive to the rotor position within the duct than to the spacing between the two rotors, with the best performance recorded when the rotor spacing was the smallest. In general, reducing the rotor blade tip clearance to the shroud increased the system performance. For the axial flight performance, the trends of rotor position within the shroud and rotor-to-rotor spacing as recorded in the static conditions prevailed. A smaller rotor tip gap resulted in better axial performance, at least whilst the inflow velocities were not too high.

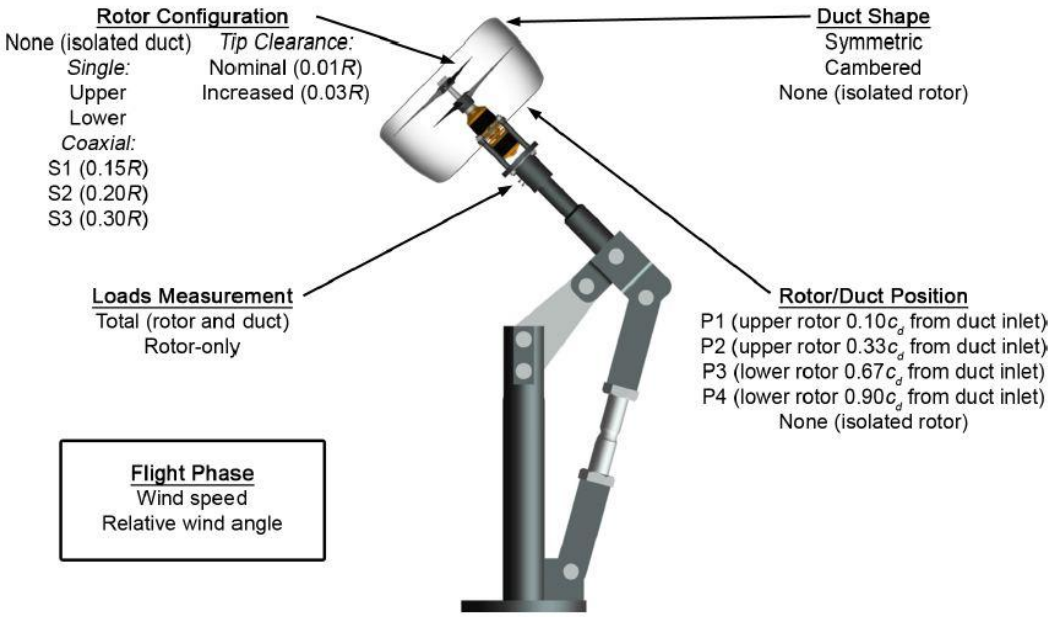

Figure 1.5: The test parameters and flight conditions of the experiments done by Lee and their possible settings (Lee, 2010).

Lee (2010) indicated that the rotors used for his research were downscaled, close variants of the Bell XV-15 tilt-rotor blades and not optimum for his experiments. He argued that the low solidity of the rotors and their small blade chords clearly resulted in lower thrust values than would be expected from a MUAV on that scale. He suggested the redesigning of the coaxial rotor blades and rotor system to match the shroud and available power from the motors.

It is thus clear that the performance of a shrouded rotor system on MUAV scale mainly depends on the following factors:

- The design of the shroud;
- The performance of the rotor system itself at MUAV scale, where the frictional losses are greater and the aerodynamic efficiencies are low due to the relatively low blade chord Reynolds numbers;
- The aerodynamic interaction between the shroud and the rotor at MUAV scale where the relatively low Reynolds number flow causes the boundary layers to be thicker which may influence the system performance differently at this scale. Parameters to be considered here may include the rotor tip gap, the rotor-to-rotor spacing and the axial placement of the rotors in the shroud;
- The flow conditions at the shroud inlet, in hover and forward flight.

A better understanding of these factors is required for the design of more efficient shrouded rotor MUAVs.

1.5 OBJECTIVES OF THIS THESIS

The primary objectives of this study are twofold: Firstly, the aerodynamic development of an efficient contra-rotating shrouded rotor system for a UAV using a freeware code named “Ducted Fan Design Code” (DFDC), which was developed by professor Mark Drela, Massachusetts Institute of Technology (MIT) Aero & Astro and Harold Youngren, Aerocraft Associates, Inc. Secondly, to verify the design by comparing the results of the DFDC to an ANSYS-CFX CFD

simulation and published experimental data. In order to satisfy these objectives the work was divided into several phases.

The first phase of the study was to obtain published experimental data of a shrouded contra-rotating rotor system in hover and forward flight in terms of thrust, torque and power to be used as a benchmark for the new design. This turned out to be a daunting task since sufficient geometric information on a ducted coaxial rotor system together with published experimental data to reconstruct the design and simulate the performance was not entirely possible. The present work is based on the Aero Flight Dynamics Directorate (AFDD) ducted coaxial rotor system and experimental data as published by Lee (2010). The description of the rotors used by Lee proved to be insufficient to accurately reproduce them. It was thus decided to design a new set of rotors for the existing shroud.

Normally the first phase in the aerodynamic design of a shrouded rotor system would be to design the shroud. In this study the shroud used by Lee (2010) is used. The second phase of the study to design a more efficient coaxial rotor system, as suggested by Lee (2010), was the selection of new rotor blade profiles by doing a detailed airfoil section analysis using XFOIL. Only profiles with a high lift to drag ratio in low Reynolds number flow and optimal geometry for design were considered.

The third phase was the design of a new coaxial rotor system using the Mark Drela DFDC_070E2a code. The performance of the new ducted coaxial rotor system was compared with several configurations of the experimental data, including variations in rotor separation distance, position of the rotors within the duct and tip clearances to investigate the aerodynamic impact of these parameters on the performance of the rotor system.

The fourth phase was to verify the DFDC results in ANSYS CFX. The numerical representation was done by using three areas, namely the far-field area, an immediate-field area where the shrouded rotor and the hub were placed, and moving reference frames for the rotors.

The ultimate objective of this study was to design a more efficient coaxial rotor system for the AFDD cambered shroud that Lee (2010) used. The design was done using DFDC which was verified with CFD simulations. In this way it was proved that DFDC could be used as a valuable preliminary design tool for the development of shrouded coaxial rotor systems for UAVs.

CHAPTER 2: ROTOR AERODYNAMICS

2.1 INTRODUCTION

This chapter discusses some of the mathematical models used to study the aerodynamics and performance of rotary wings. One-dimensional momentum theory allows for the approximation of downwash velocities and rotor efficiencies, but a more thorough aerodynamic theory like blade element theory is needed to predict blade geometry, blade sectional orientation and blade twist. Blade element theory (BET) and momentum theory were combined in the blade element momentum theory (BEMT) to incorporate the effect of drag and blade geometry on rotor performance.

In blade-element models each propeller blade is divided into a number of small independent sections. It is assumed that each section behaves aerodynamically as a wing in two-dimensional flow. The flight velocity and rotational velocity are usually known, but the induced velocity components are unknown and must be found by using other models like the momentum model. By using the induced velocity as input to the blade-element model, the aerodynamic loads along the blade are calculated by an iterative scheme. The integration of the aerodynamic loads along the blades results in the calculation of the propeller's thrust and required power.

The momentum and blade element theories presented in this study were developed from Johnson (1980) and Leishman (2006), which are both frequently quoted.

2.2 MOMENTUM THEORY FOR SHROUDED ROTORS

In a ducted fan or shrouded rotor design, the thrust consists of two parts, the thrust of the rotor or fan and the thrust from the shroud or duct as illustrated in Figure 2.1.

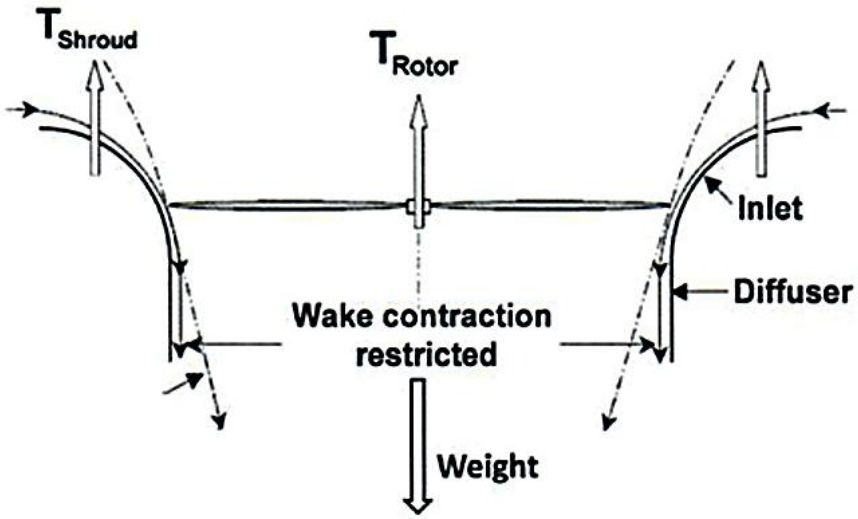

Figure 2.1: Shrouded rotor operating theory (Hrishikeshavan, 2011).

The shroud consists of an inlet and a diffuser section. Considering a case where the same total thrust is being produced by a shrouded and an isolated rotor, the diffuser recovers the kinetic energy of the slipstream and increases the mass flow rate through the rotor.

The rotation of the rotor causes a low pressure above the rotor plane, which accelerates the flow over the shroud inlet surface. This causes a low pressure over the shroud inlet area which results in an added lift force. In order to explain the improvements in hover performance with a shrouded rotor, an outline of the momentum theory applied to a shrouded rotor is given below. The full derivations of these results can be found in Leishman (2006) and Pereira (2008).

Figure 2.2 illustrates the 2-dimensional rotor wake for the shrouded rotor. The assumptions made in the momentum theory are: steady, frictionless, incompressible, and quasi 1-dimensional flow. The rotor imparts only axial momentum with no rotation in the wake. It is further assumed that the wake of the shrouded rotor expanded to the atmospheric pressure at the diffuser exit plane.

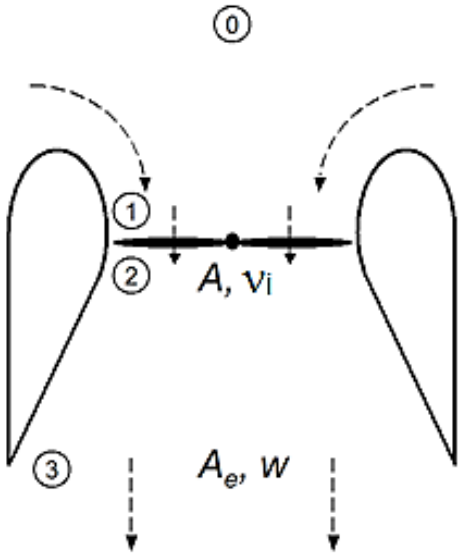

Figure 2.2: The 2-dimensional rotor wake for the shrouded rotor (Pereira, 2008).

For the shrouded rotor in hover flight (V_c = 0 m/s) or climbing flight with the climb velocity V_c and w the induced velocity in the far wake of the rotor, the following velocities and identities at the different stations in Figure 2.2 arise:

$$v_0 = \mathrm{V_c} \tag{2.1}$$

$$v_1 = v_2 = \mathrm{V_c} + v_i \tag{2.2}$$

$$v_3 = \mathrm{V_c} + \mathrm{w} \tag{2.3}$$

$$A_1 = \mathrm{A_2} = \mathrm{A} \tag{2.4}$$

$$A_3 = \mathrm{A_e} = \sigma_d A \tag{2.5}$$

$$p_0 = p_3 = p_e \tag{2.6}$$

$$\Delta \mathrm{p_{shroud}} = p_2 - p_3 \tag{2.7}$$

Assuming complete expansion at the shroud exit plane it follows from the conservation of mass that the mass flow rate is given as:

$$\dot{m} = \rho A(V_c + v_i) = \rho A_e(V_c + \mathrm{w}) \tag{2.8}$$

The expansion ratio can be expressed as:

$$\sigma_d = \frac{A_e}{A} = \frac{(V_c + v_i)}{(V_c + \mathrm{w})} \tag{2.9}$$

Since $\mathrm{w} = 2v_i$ for the isolated rotor, it follows that the expansion ratio for the isolated case varies between ½ and 1.0, depending on the climb velocity (Pereira, 2008). For a shrouded rotor, σ_d is constant at all climb velocities and depends on the geometry of the diffuser.

$$\Rightarrow w = \frac{(V_c + v_i)}{\sigma_d} - V_c \tag{2.10}$$

From the conservation of momentum on the shrouded rotor system, it follows that:

$$T_{total} = T_{rotor} + T_{shroud} = \dot{m}w \tag{2.11}$$

Substituting Equation 2.1 for $V_c = 0$ into Equation 2.11 results in the ideal induced velocity, for the shrouded rotor in a hover flight condition:

$$v_h = \sqrt{\frac{\sigma_d T_{total}}{\rho A}} \tag{2.12}$$

Solving these equations yields the expression for the ratio of the ideal induced velocities is given by (Pereira, 2008):

$$\frac{v_i}{v_h} = \frac{V_c}{2v_h}(\sigma_d - 2) + \sqrt{\left(\frac{\sigma_d V_c}{2v_h}\right)^2 + 1} \tag{2.13}$$

Applying the actuator-disc theory, the thrust generated by the rotor alone yields:

$$T_{rotor} = \Delta p \cdot A = (p_2 - p_1) \cdot A \tag{2.14}$$

Applying Bernoulli equation between positions 0 and 1 and between positions 2 and 3 in Figure 2.2 and solving these equations for the pressure increase across the rotor yields:

$$\Delta p = \frac{1}{2}\rho(V_c + \mathrm{w})^2 - \frac{1}{2}\rho {V_c}^2 = \rho \mathrm{w}\left(\frac{\mathrm{w}}{2} + V_c\right) \tag{2.15}$$

From Equations 2.11 and 2.15 it follows that the rotor thrust fraction can be given as:

$$\frac{T_{rotor}}{T_{total}} = \frac{(p_2 - p_1) \cdot A}{\dot{m}\mathrm{w}} = \frac{\left(V_c + \frac{\mathrm{w}}{2}\right)}{(V_c + v_i)} = \frac{v_i + V_c(\sigma_d + 1)}{2\sigma_d(V_c + v_i)} \tag{2.16}$$

Equation 2.16 shows that even though the total thrust is constant in a steady climb, the rotor thrust varies, depending on the climb velocity.

The ratio of the rotor thrust in hover and in climbing flight is given by:

$$\frac{(T_{rotor})_c}{(T_{rotor})_h} = \frac{(T_{rotor}/T_{total})_c}{(T_{rotor}/T_{total})_h} = \frac{v_i + V_c(\sigma_d + 1)}{(V_c + v_i)} \tag{2.17}$$

The product of the velocity of the air through the rotor and the rotor thrust represents the ideal power required and can be written as:

$$P_c = (T_{rotor})_c \cdot (V_c + v_i) = (T_{rotor})_h \cdot [v_i + V_c(\sigma_d + 1)] \tag{2.18}$$

The ideal power to hover for a shrouded rotor is the product of the thrust in hover and the air flow through the rotor disc, v_h as given in Equation 2.12:

$$P_h = (T_{rotor})_h \cdot v_h = \frac{T_{total}^{3/2}}{\sqrt{4\sigma_d \rho A}} \tag{2.19}$$

The ratio of the power required to climb versus the hover power for a shrouded rotor can be expressed as:

$$\frac{P_c}{P_h} = \frac{v_i + V_c(\sigma_d + 1)}{v_h} = \left(3\sigma_d \frac{V_c}{2v_h}\right) + \sqrt{\left(\frac{\sigma_d V_c}{2v_h}\right)^2 + 1} \tag{2.20}$$

It should be noted that although these equations represent the shrouded rotor performance, by changing the value of the expansion ratio as given in Equation 2.9, these equations reduce to the isolated rotor case. By setting V_c = 0 m/s they reduce to the hover flight conditions. In particular, for the shrouded rotor in hover flight, it is proven by Pereira (2008) that the total thrust of the shrouded rotor system consists of contributions from the rotor, the inlet section and diffuser and are summarised as follows:

The ideal power:

$$P_i = \frac{T_{total}^{3/2}}{\sqrt{4\sigma_d \rho A}} \tag{2.21}$$

The rotor thrust in terms of the total thrust of the shrouded rotor system in hover:

$$T_{rotor} = \frac{T_{total}}{2\sigma_d} \tag{2.22}$$

The diffuser thrust:

$$T_{diffuser} = -\frac{T_{total}(\sigma_d - 1)^2}{2\sigma_d} \tag{2.23}$$

The inlet thrust:

$$T_{inlet} = \frac{T_{total} \cdot \sigma_d}{2} \tag{2.24}$$

The thrust ratio between the shroud and the rotor is:

$$\frac{T_{shroud}}{T_{rotor}} = (2\sigma_d - 1) \tag{2.25}$$

This shows that as $\sigma_d = \frac{A_e}{A}$ increases, the shroud gradually reduces the proportional load on the rotor. The diffuser increases the downward force (negative thrust) on the shrouded rotor system, the rotor thrust decreases and the inlet thrust increases. For a straight diffuser, where $\sigma_d = 1$, the rotor and shroud inlet share about 50% of the total thrust.

Using Equation 2.18 and 2.19 for an isolated rotor, where the rotor thrust is equal to the total thrust and remains constant, it can be shown that the ratio of the power required to climb versus the hover power is:

$$\frac{P_c}{P_h} = \frac{v_i + V_c}{v_h} = \frac{V_c}{2v_h} + \sqrt{\left(\frac{V_c}{2v_h}\right)^2 + 1} \tag{2.26}$$

Figure 2.3 shows a comparison of the power requirements of a shrouded rotor versus an open rotor in terms of the climb velocity, normalised by the ideal induced velocity of the open rotor in hover. This comparison was done with the two configurations producing the same total thrust and having the same disc area. From the figure it follows that the shrouded rotor requires less power up to a climb velocity close to $v_{h,OR}$ and that the shroud with the higher expansion ratio results in the most savings when the climb velocity is less than $v_{h,OR}$.

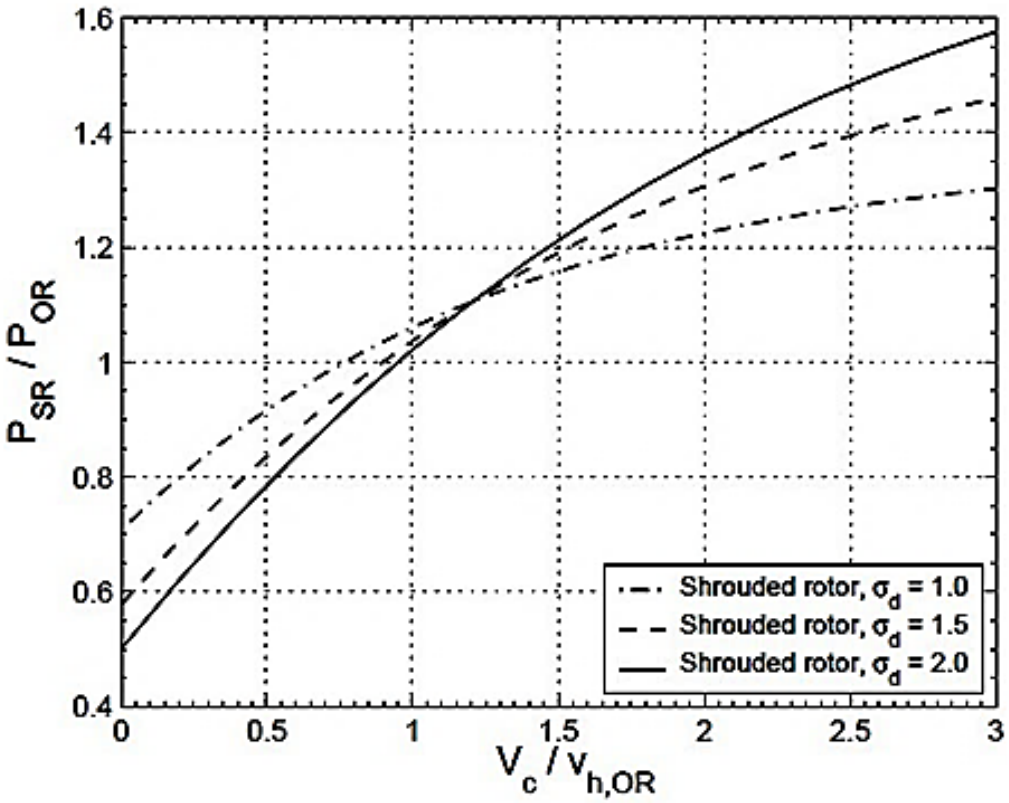

Figure 2.3: A comparison of the required power for an open and shrouded rotor in climbing flight (Pereira, 2008).

2.2.1 Figure of merit (FM) and other measures of rotor efficiency

The efficiency of a rotor is difficult to define since there are many parameters involved and their effects on performance may not be the same on different rotors. The FM is equivalent to the static thrust efficiency and is a ratio of the ideal power required to hover, which assumes no viscous losses, to the actual power required to hover by the rotor. The FM may be used to compare two rotors, in which case they need to operate at the same disc loading (DL), where the DL of a rotor is the ratio of the total thrust to the rotor disc area. For an open rotor the FM is defined as:

$$\begin{aligned} FM &= \frac{Ideal\ power\ required\ to\ hover}{Actual\ power\ required\ to\ hover} \\ &= \frac{Ideal\ power}{Induced\ power + Profile\ power} \\ &= \frac{P_i}{\kappa P_i + P_0} = \frac{\frac{C_T^{3/2}}{\sqrt{2}}}{\kappa\frac{C_T^{3/2}}{\sqrt{2}} + \frac{\sigma C_{d_0}}{8}} \end{aligned} \tag{2.27}$$

The induced power is the product of κ and the ideal power and κ, the ideal power correction factor derived from rotor measurements and compensating for non-uniform flow with compressibility, swirl, the tip losses and a finite number of blades. The profile power is determined by the power required to overcome the drag on the rotor blades. Experimental results indicated that in hovering flight a typical average value of κ for open rotors is 1.15, whilst a first estimation for $C_{d_0} \approx 0.01$ (Leishman, 2006). The rotor solidity, $\sigma = \frac{N_b c R}{A}$ is the ratio of the rotor blade area to the rotor disc area, with typical values for a helicopter rotor ranging between 0.05 and 0.12. $P_h = (T_{rotor})_h \cdot v_h$

For a shrouded rotor, the wake development is influenced by the geometry of the shroud and the expression for the ideal power (P_i) and ideal power coefficient (C_{Pi}) needs to incorporate the diffuser's expansion ratio σ_d and is given by:

$$\mathrm{P_i} = \mathrm{T_{rotor}} \cdot v_i = \frac{\mathrm{T}}{2\sigma_\mathrm{d}} \cdot \sqrt{\frac{\sigma_\mathrm{d}\mathrm{T}}{\rho\mathrm{A}}} = \frac{\mathrm{T}^{3/2}}{\sqrt{4\sigma_\mathrm{d}\rho\mathrm{A}}} \tag{2.28}$$

$$\mathrm{C_{P_i}} = \mathrm{C_{T_{rotor}}} \cdot \lambda_\mathrm{i} = \frac{\mathrm{T}}{2\sigma_\mathrm{d}} \cdot \sqrt{\sigma_\mathrm{d}\mathrm{C_T}} = \frac{\mathrm{C_T}^{3/2}}{\sqrt{4\sigma_\mathrm{d}}} \tag{2.29}$$

where λ_i is the induced inflow ratio, $\lambda_\mathrm{i} = \frac{v_i}{\Omega \mathrm{R}}$ and $T = \mathrm{T_{total}} = \mathrm{T_{rotor}} + \mathrm{T_{shroud}}$ is the total thrust. The relation between the power loading (PL) and the $^{\mathrm{C_T}}/_{\mathrm{C_P}}$ ratio is also applicable to the shrouded rotor as a measure of efficiency at the same tip speed:

$$\mathrm{PL} = \frac{\mathrm{T}}{\mathrm{P}} = \frac{1}{v_{tip}} \cdot \frac{\mathrm{C_T}}{\mathrm{C_P}} \tag{2.30}$$

The expression for the disc loading (DL) of a shrouded rotor is given as:

$$\mathrm{DL} = \frac{\mathrm{T_{rotor}}}{\mathrm{A}} = \frac{\mathrm{T}}{2\sigma_\mathrm{d}\mathrm{A}} \tag{2.31}$$

Substituting Equation 2.31 into Equation 2.28 for the ideal power:

$$\mathrm{P_i} = \mathrm{T} \cdot \sqrt{\frac{\mathrm{DL}}{2\rho}} \tag{2.32}$$

With the figure of merit defined as $FM = {}^{\mathrm{P_i}}/_{P}$, using the relation between the power loading and FM for open rotors and the expression for the DL of shrouded rotors, it follows that :

$$\frac{\mathrm{T}}{\mathrm{P}} = \sqrt{\frac{2\rho}{\mathrm{DL}}} \cdot \mathrm{FM} = \sqrt{\frac{4\sigma_\mathrm{d}\rho\mathrm{A}}{\mathrm{T}}} \cdot \mathrm{FM} = \sqrt{\frac{4\rho\mathrm{A}}{\mathrm{T}}} \cdot \mathrm{FM}\sqrt{\sigma_\mathrm{d}} \tag{2.33}$$

Equation 2.33 is known as the “generalised” figure of merit and indicates that for a fixed total thrust and rotor disc area, the power is inversely proportional to $\mathrm{FM} \cdot \sqrt{\sigma_\mathrm{d}}$. Equation 2.33 can also be rearranged to indicate that for a fixed power and disc area the thrust produced will be directly proportional to $\left(\mathrm{FM}\sqrt{\sigma_\mathrm{d}}\right)^{2/3}$. Substituting Equation 2.30 into Equation 2.33 gives a relation between $\frac{\mathrm{C_T}}{\mathrm{C_P}}$ and the generalised FM:

$$\frac{\mathrm{C_T}}{\mathrm{C_P}} = \frac{2}{\sqrt{\mathrm{C_T}}} \cdot \mathrm{FM}\sqrt{\sigma_\mathrm{d}} \tag{2.34}$$

It is important to note that the equations above also hold for the open rotor case where the expansion ratio $\sigma_\mathrm{d} = 0.5$ (Pereira, 2008).

2.3 MOMENTUM THEORY FOR COAXIAL ROTORS

In order to understand the coaxial counter rotating shrouded rotor system, a simple momentum analysis of an open coaxial rotor system in hover will be considered first. It is assumed that the two coaxial rotors are closely spaced to ensure minimum wake contraction before it passes through the lower rotor. This will ensure that the areas of the upper and lower rotors are the same, $A_u = A_l = A$ as indicated in Figure 2.4. This is also true for the shrouded coaxial rotor system under consideration in this study, even though there is some vertical separation between the rotors. Based on the conservation of mass, the induced velocity through each disc will be the same, from which it follows that each disc will produce the same thrust T so that the total system thrust is $2T$ where

$$T_u = T_l = T = W/2 \tag{2.35}$$

Based on simple momentum theory and from Equation 2.12, the effective induced velocity of this coaxial rotor configuration will be

$$(v_i)_e = \sqrt{\frac{2T}{2\rho A}} = \sqrt{\frac{T}{\rho A}} = \sqrt{\frac{W}{2\rho A}} \tag{2.36}$$

And from Equation 2.19 and 2.36, the ideal power, P_i, is

$$(P_i)_{coax} = 2T(v_i)_e = 2T\sqrt{\frac{2T}{2\rho A}} = \frac{(2T)^{3/2}}{\sqrt{2\rho A}} = \frac{W^{3/2}}{\sqrt{2\rho A}} \tag{2.37}$$

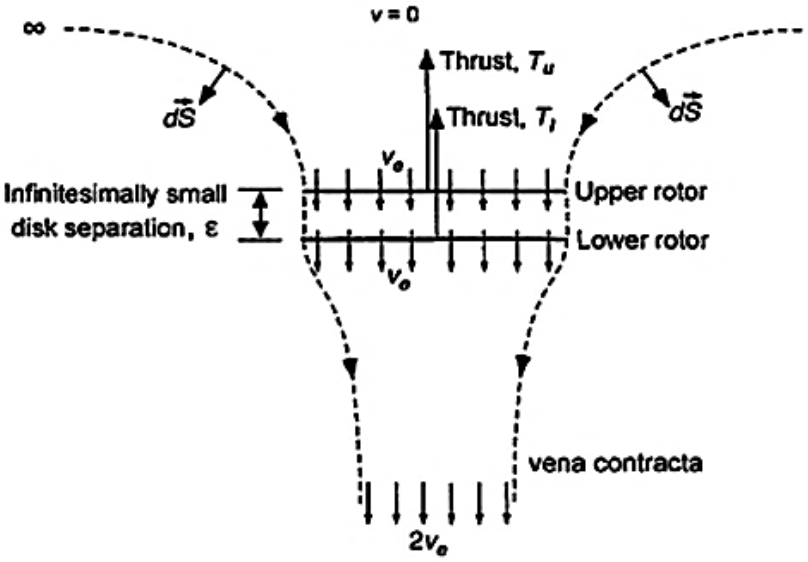

Figure 2.4: Control volume for a coaxial rotor system with rotors in the same plane and sharing the same induced velocity (Leishman, 2008).

If one considers the ideal power required of the coaxial rotors as if they were operating as separate rotors, isolated from each other, the ideal power for each rotor will be Tv_i and the total ideal power for the two separate rotors will be:

$$(P_i)_{isolated} = 2\left(\frac{T^{3/2}}{\sqrt{2\rho A}}\right) = \frac{2T^{3/2}}{\sqrt{2\rho A}} = \frac{W^{3/2}}{\sqrt{4\rho A}} \tag{2.38}$$

Let the interference-induced loss factor κ_{int} related to the coaxial rotor system be defined as:

$$\kappa_{int} = \frac{(P_i)_{coax}}{(P_i)_{isolated}} = \left(\frac{W^{3/2}}{\sqrt{2\rho A}}\right)\Big/\left(\frac{W^{3/2}}{\sqrt{4\rho A}}\right) = \sqrt{2} = 1.41 \tag{2.39}$$

From the equation above, it follows that there is a 41% increase in ideal power required by this coaxial system compared to the power required for the two rotors operating in isolation. The total ideal power required of the coaxial rotor system is thus:

$$(P_i)_{coax} = 2\kappa_{int}\left(\frac{T^{3/2}}{\sqrt{2\rho A}}\right) = \kappa_{int}\frac{W^{3/2}}{\sqrt{4\rho A}} \tag{2.40}$$

In the event where the two coaxial rotors are operated closely to each other to give zero resultant torque it can be shown that $\kappa_{int} = \sqrt{2} = 1.41$ (Leishman & Syal, 2008). Note that when the two coaxial rotors operate closely in the same plane, a torque balance can only be reached if $T_u = T_l$.

According to various experimental results given in the article by Coleman (1997) the forgoing momentum analysis over-predicts the ideal power required by the closely spaced coaxial rotors. One reason for the over prediction of the power may be the fact that there needs to be finite spacing between the rotors to prevent inter-rotor blade collisions. This causes the lower rotor to almost always operate in the fully developed slipstream of the upper rotor, since experiments by Taylor (1950) indicated that the wake of the upper rotor contracts within 0.25R below the rotor. In the article of Leishman (2006) the ideal wake contraction ratio is 0.707, but in reality it is found to be in the order of 0.80. If it is assumed that the wake contraction of the upper rotor is not directly affected by the lower rotor, then from the ideal flow considerations, half of the rotor area of the lower rotor will operate in the fully developed slipstream of the upper rotor as indicated in Figure 2.5. Leishman (2006) analysed this flow condition using similar principles to the simple non-viscous momentum theory for two flow conditions. In the first case it was assumed that the two rotors produce the same thrust, $T_u = T_l = T$, in which case the interference power factor κ_{int} is given by:

$$\kappa_{int} = \frac{(P_i)_{coax}}{(2P_i)_{isolated}} = \frac{2.562Tv_h}{2Tv_h} = 1.281 \tag{2.41}$$

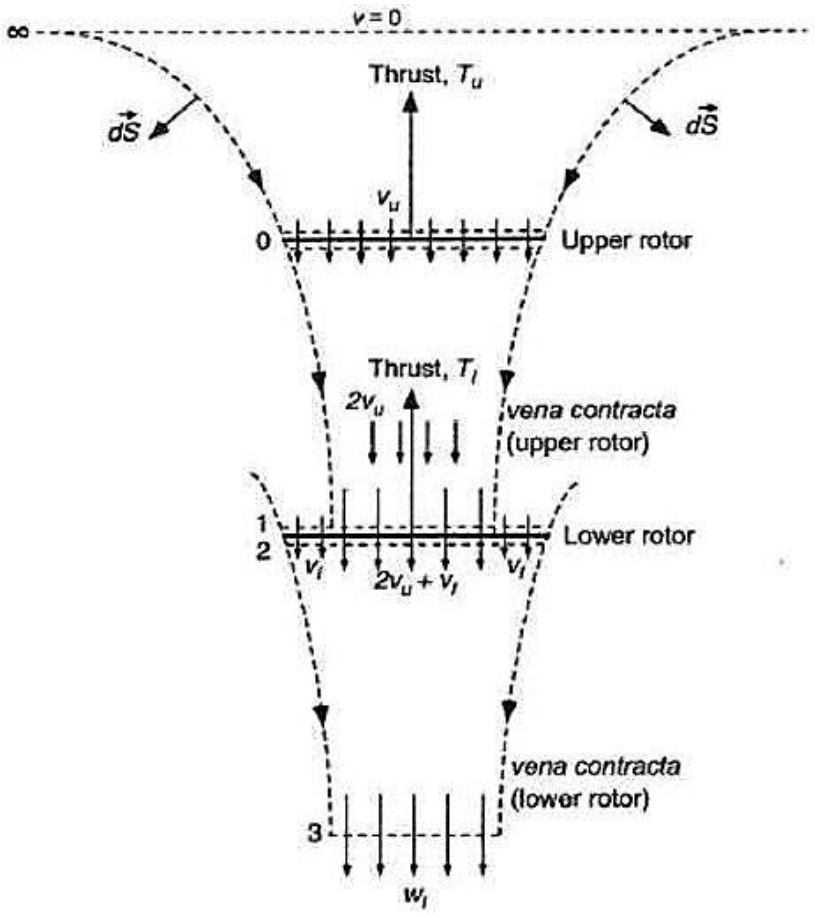

Figure 2.5: Flow model for a coaxial rotor system with the lower rotor operating in the fully developed slipstream of the upper rotor (Leishman, 2006).

This gives a 28% increase in induced losses, which compares much better to the 41% increase when the two rotors have no vertical separation. In the second case it was assumed that the two coaxial rotors are operating at equal but opposite torque, in which case the interference power factor κ_{int} is given by

$$\kappa_{int} = \frac{2.4375 v_h}{2 v_h} = 1.219 \tag{2.42}$$

and suggests a 22% increase in interference losses, compared to the case when the two rotors have no vertical separation. Leishman & Syal (2008) investigated an option where the two rotors are operated independently but with the same thrust sharing as for the torque balanced case, which resulted in an interference-induced power factor $\kappa_{int} = 1.2657$.

These results indicate that as the vertical distance increases, the interference losses decrease. Note that these results indicate the minimum induced losses for the different coaxial configuration and set a basis for comparison with real coaxial rotor systems.

2.3.1 Figure of merit (FM) for coaxial rotors

To compare the relative efficiency of single and coaxial rotors they must be operated at the same effective disc loading. If this is true, the figure of merit for the coaxial system can be defined as:

$$\mathrm{FM} = \frac{P_{ideal}}{\kappa P_{ideal} + P_0} = \frac{\frac{C_T^{3/2}}{\sqrt{2}}}{\kappa_{int}\kappa\frac{C_T^{3/2}}{\sqrt{2}} + \frac{\sigma C_{d_0}}{8}} \tag{2.43}$$

Where $\kappa_{int} = 1$ for an unshrouded single rotor (Leishman, 2006). A new FM expression for a coaxial rotor was developed by Leishman & Syal (2008) from the momentum theory solutions for a coaxial rotor. Their expression also incorporated the effect of relative thrust sharing between the rotors which would result in different disc loadings and efficiencies of the rotors and can be written as:

$$FM = \frac{1.2657\frac{C_{T_l}^{3/2}}{\sqrt{2}}\left[\left(\frac{C_{T_u}}{C_{T_l}}\right)^{3/2} + 1\right]}{\kappa_{int}\kappa\frac{C_{T_l}^{3/2}}{\sqrt{2}}\left[\left(\frac{C_{T_u}}{C_{T_l}}\right)^{3/2} + 1\right] + \frac{\sigma C_{d_0}}{4}} \tag{2.44}$$

where $\kappa_{int} \geq 1.2657$. Generally $\kappa_{int} = 1.28$, $\kappa \approx 1.10 - 1.20$, $C_{d_0} \approx 0.011$ and $\sigma(coaxial) = 2\sigma(single)$. The special case of $C_{T_u} = C_{T_l} = C_w/2$ can also be treated in general at torque balance $C_{T_u}/C_{T_l} > 1$.

2.4 BLADE ELEMENT THEORY

The momentum theory provides no information regarding the design of the rotor blades in order to produce a specified thrust. This method also ignores the profile drag losses. In blade element theory (BET) each propeller blade is divided into a number of small independent airfoil sections. It is assumed that each section behaves aerodynamically as a wing in a two-dimensional flow, with each element considered independent of the adjoining elements. The section lift and drag coefficients are functions of the local angle-of-attack, Mach number, and Reynolds number. These parameters are functions of the cross-sectional

resultant velocity, which in turn is found by summing all the contributions of the flight velocity, rotation of the blade and induced velocity. Tip losses, the influence of the wake and other empirical factors may be applied to accommodate three dimensional effects. Lift and drag forces per unit span are then calculated from this resultant velocity acting on the airfoil. The rotor performance such as the thrust and torque are obtained by integrating the individual contribution of each element along the blade radius and multiplying this with the number of blades, N_b.

BET can form the basis of design for the rotor blades in terms of blade twist, planform distribution and airfoil shape in order to provide a specified overall rotor performance. Figure 2.6 shows the flow environment and the aerodynamic forces on a typical blade element on the rotor that will be used for the derivation of the BET.

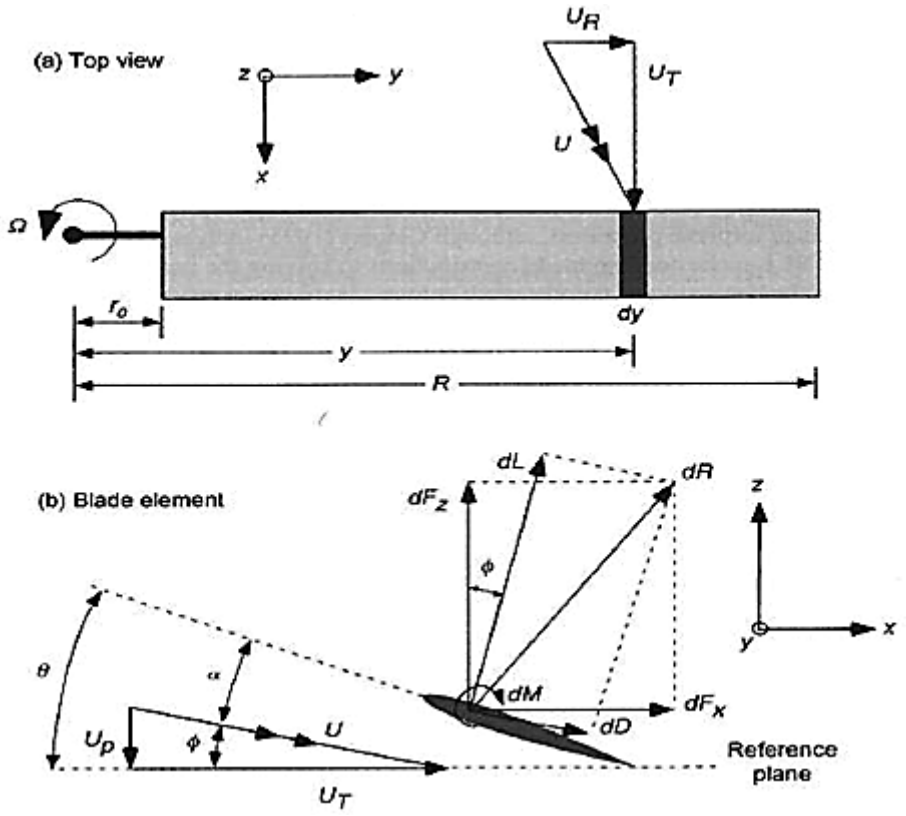

Figure 2.6: Incident velocities and aerodynamic forces on a typical rotor blade element (Leishman, 2006).

The blade is divided into finite radial elements of width dy, where each element is defined by its radial position y. Figure 2.6 (a) illustrates the top view of the element and Figure 2.6 (b) shows the vector velocities and the aerodynamic forces acting in the plane perpendicular to the rotor axis of rotation. It is assumed that the aerodynamic forces arise entirely from the velocity and angle of attack, (AoA) normal to the leading edge of the blade section. From Figure 2.6 the geometric pitch angle of the blade element relative to the plane of rotation is θ, the climbing speed is V_c and the local induced velocity v_i. $U_P = V_c + v_i$ is normal to the rotor plane and $U_T = \Omega y$, parallel to the rotor blade due to blade rotation in the disc plane, so that the resultant velocity at the blade element is

$$U = \sqrt{U_T^2 + U_P^2 + U_R^2} \approx \sqrt{U_T^2 + U_P^2} \tag{2.45}$$

Since only airflow perpendicular to the blade axis is considered in simple blade element theory, the total velocity is represented by the rightmost part of Equation 2.45. The relative inflow angle or the induced angle of attack at the blade element for small angles is

$$\phi = \tan^{-1}\left(\frac{U_P}{U_T}\right) = \tan^{-1}\left(\frac{V_c + v_i}{\Omega y}\right) \approx \frac{U_P}{U_T} \tag{2.46}$$

and the aerodynamic or effective AoA for small inflow angles is

$$\alpha = \theta - \emptyset = \theta - \frac{U_P}{U_T} \tag{2.47}$$

The incremental lift and drag per unit span of the blade element are

$$dL = \frac{1}{2}\rho U^2 c C_l dy \; and \; dD = \frac{1}{2}\rho U^2 c C_d dy \tag{2.48}$$

where c is the local blade chord and the coefficient of lift, C_l , and the coefficient of drag, C_d , are functions of the angle of attack, α, Reynolds number, Re, and Mach number, M, although the last two are sometimes ignored. The lift coefficient is often approximated by a linear function of α with a slope $C_{l_\alpha} = 2\pi$. According to Bramwell *et al*. (2001), a typical coefficient of drag for a rotor blade can be expressed as

$$C_d = 0.0087 - 0.0216\alpha + 0.4\alpha^2 \tag{2.49}$$

From Figure 2.6 the incremental lift and drag forces can be resolved perpendicular and parallel to the rotor disc plane as

$$dF_z = dL\cos\phi - dD\sin\phi \quad and \quad dF_x = dL\sin\phi + dD\cos\phi \tag{2.50}$$

The contributions to the thrust, torque and power of the rotor with N_b number of blades are

$$dT = N_b dF_z, \qquad dQ = N_b dF_x y \; and \; dP = N_b dF_x \Omega y. \tag{2.51}$$

Substituting the results for dF_x and dF_z of Equation 2.50 into Equation 2.51 and noting that for helicopter rotors $U_P \ll U_T$, so that $\sqrt{U_T^2 + U_P^2} \approx U_T$; and that the induced angle $\emptyset$ is small, so that $\emptyset \approx \frac{U_P}{U_T}$, $\sin\emptyset \approx \emptyset \; and \; \cos\emptyset \approx 1$; also, the drag is at least one order less than the lift, so that $dD\sin\phi$ is negligible, giving

$$dT = N_b(dL\cos\phi - dD\sin\phi) \approx N_b dL \tag{2.52}$$

$$dQ = N_b(dL\sin\phi + dD\cos\phi)y \approx N_b(\phi dL + dD)y \tag{2.53}$$

$$dP = N_b(dL\sin\phi + dD\cos\phi)\Omega y \approx N_b\Omega(\phi dL + dD)y \tag{2.54}$$

The non-dimensional quantities are introduced by dividing lengths by R and velocities by ΩR.

Thus, $r = y/R$, and $U/\Omega R = \Omega y/\Omega R = y/R = r$.

Note that $dC_T = dT/\rho A(\Omega R)^2$, $dC_Q = dQ/\rho A(\Omega R)^2 R$ and $dC_P = dP/\rho A(\Omega R)^3$ and $\sigma_{rotor} = Blade\ area/disk\ area = N_b c/\pi R$ for a rectangular blade with a constant chord.

The inflow ratio can now be written as

$$\lambda = \frac{V_c+v_i}{\Omega R} = \frac{V_c+v_i}{\Omega y}\left(\frac{\Omega y}{\Omega \mathrm{R}}\right) = \frac{U_P}{\Omega \mathrm{R}}\left(\frac{y}{\mathrm{R}}\right) = \phi r \tag{2.55}$$

The thrust and power are the integral sums over the radius of the equations above

$$T = \int_0^R dT = \int_0^R N_b dL = \frac{1}{2}\rho N_b \int_0^R U^2 c C_l dy \tag{2.56}$$

$$\begin{aligned} P = \int_0^R dP &= \int_0^R N_b \Omega(\phi dL + dD)\mathrm{y}\mathrm{d}y \\ &= \frac{1}{2}\rho N_b \int_0^R U^2 c(\phi C_l + C_d)\Omega y dy \end{aligned} \tag{2.57}$$

The incremental thrust coefficient is

$$\begin{aligned} dC_T &= \frac{N_b dL}{\rho A(\Omega R)^2} = \frac{N_b\left(\frac{1}{2}\rho U_T^2 c C_l dy\right)}{\rho(\pi R^2)(\Omega R)^2} \\ &= \frac{1}{2}\left(\frac{N_b c}{\pi R}\right) C_l \left(\frac{y}{R}\right)^2 d\left(\frac{y}{R}\right) = \frac{1}{2}\sigma_{rotor} C_l r^2 dr \end{aligned} \tag{2.58}$$

Similarly it can be shown that the incremental torque and power coefficients are

$$dC_Q = \frac{N_b(\phi dL + dD)y}{\rho A(\Omega R)^2 \mathrm{R}} \tag{2.59}$$

$$dC_P = \frac{N_b(\phi dL + dD)\Omega y}{\rho A(\Omega R)^3} \tag{2.60}$$

$$\begin{aligned} dC_Q \equiv dC_P &= \frac{N_b(\phi dL + dD)y}{\rho A(\Omega R)^2 R} = \frac{1}{2}\left(\frac{N_b c}{\pi R}\right)(\phi C_l + C_d) r^3 dr \\ &= \frac{1}{2}\sigma_{rotor}(\phi C_l + C_d) r^3 dr \end{aligned} \tag{2.61}$$

Substituting Equation 2.55 into Equation 2.61 gives

$$dC_P = \frac{1}{2}\sigma_{rotor}(\lambda_i C_l r^2 + C_d r^3) dr \tag{2.62}$$

Based on the linear lift curve where $C_l = \alpha \cdot C_{l_\alpha}$ and from Figure 2.6 and Equation 2.55 it follows that

$$\alpha = \theta - \phi = \theta - \lambda/r \tag{2.63}$$

The incremental thrust coefficient in Equation 2.59 can now be written as

$$dC_T = \frac{1}{2}\sigma_{rotor} C_l r^2 dr = \frac{\sigma_{rotor} C_{l_\alpha}}{2}(\theta r^2 - \lambda r)dr \tag{2.64}$$

Integrating Equations 2.59 and 2.60 along the blade from the root to the tip and assuming a rectangular blade, results in the total C_T and $C_Q \equiv C_P$.

$$C_T = \frac{1}{2}\sigma_{rotor}\int_0^1 C_l r^2 dr \tag{2.65}$$

$$C_Q \equiv C_P = \frac{1}{2}\sigma_{rotor}\int_0^1 (\phi C_l + C_d) r^3 dr = \frac{1}{2}\sigma_{rotor} \tag{2.66}$$

To calculate the coefficient of thrust and torque of the equations above, the spanwise variation in the inflow, λ and the sectional coefficients of lift and drag, C_l and C_d, must be known. Assuming two-dimensional aerodynamics, $C_l = C_l(\alpha, \mathrm{Re}, \mathrm{M})$, $C_d = C_d(\alpha, \mathrm{Re}, \mathrm{M})$, $\alpha = \alpha(V_c, \theta, v_i)$ and $v_i = (r)$. Since these effects cannot generally be expressed as simple equations a numerical solution is needed to solve for C_T and C_P.

2.5 BLADE ELEMENT MOMENTUM THEORY (BEMT) FOR COAXIAL ROTORS

The BEMT is a two-dimensional theory that assumes varying inflow over the rotor blades and that consecutive annuli on the rotor disc have no shared influence on each other. The flow model used for the BEMT analysis is given in Figure 2.7.

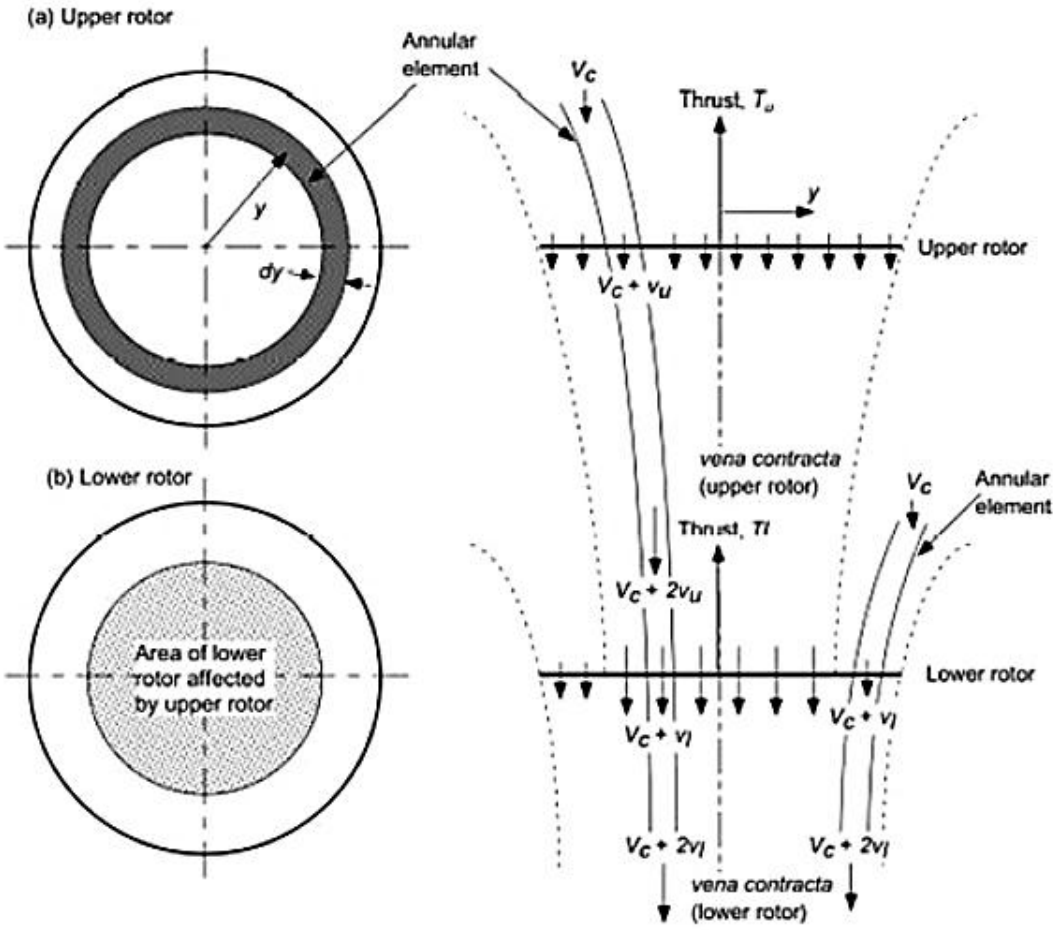

Figure 2.7: Flow model used for the BEMT analysis (Leishman 2006).

Assume that the wake of the upper rotor affects the flow into the lower rotor, but the upper rotor is not largely affected by the lower rotor. Consider the upper rotor with an axial climb velocity, $V_c = V_\infty$, as discussed by Leishman (2006), then the differential mass flow rate through and thrust on the rotor annulus, is given as

$$d\dot{m} = \rho dA(V_\infty + v_u) = 2\pi\rho(V_\infty + v_u)ydy \tag{2.67}$$

and

$$dT_u = 2\rho(V_\infty + v_u)v_u dA = 4\pi\rho(V_\infty + v_u)v_u ydy \tag{2.68}$$

Or in dimensionless form

$$\begin{aligned} dC_{T_u} &= \frac{dT_u}{\rho(\pi R^2)(\Omega R)^2} = \frac{2\rho(V_\infty + v_u)v_u dA}{\rho\pi R^2(\Omega R)^2} \\ &= \frac{2\rho(V_\infty + v_u)v_u(2\pi ydy)}{\rho\pi R^2(\Omega R)^2} = 4\lambda\lambda_u rdr \end{aligned} \tag{2.69}$$

Thus, on the annulus the incremental thrust coefficient is

$$dC_{T_u} = 4\lambda\lambda_u rdr = 4\lambda(\lambda - \lambda_\infty)rdr \tag{2.70}$$

since $\lambda_u = \lambda - \lambda_\infty$. The incremental induced power required is

$$dC_{P_u} = \lambda dC_{T_u} = 4\lambda^2\lambda_u rdr = 4\lambda^2(\lambda - \lambda_\infty)rdr \tag{2.71}$$

These results ignore swirl losses in the wake, which is acceptable for rotors that are lightly loaded. The blade tip induced losses due to the formation of the tip vortex can be accounted for in the BEMT by using the Prandtl tip-loss function, which is defined in terms of a correction factor, F, where

$$F = \left(\frac{2}{\pi}\right)\cos^{-1}(\exp(-f)), \tag{2.72}$$

and f is defined by the number of blades N_b and the radial location of the blade element, r and ϕ, the induced inflow angle, $\phi = \lambda(r)/r$ for small angles.

$$f = \frac{N_b}{2}\left(\frac{1-r}{r\phi}\right) \tag{2.73}$$

The function F can be seen as a reduction factor added to the variation in the fluid velocity passing through the control volume. From the momentum theory it follows that

$$dC_T = 4\mathrm{F}\lambda^2\mathrm{rdr} \tag{2.74}$$

and from blade element theory, the incremental thrust of the same annulus is

$$dC_{T_u} = \frac{1}{2}\sigma C_l r^2 dr = \frac{\sigma C_{l_\alpha}}{2}(\theta_u r^2 - \lambda_r)dr \tag{2.75}$$

with θ_u, the blade pitch distribution of the upper rotor. Equating these two equations and using, $\lambda_u = \lambda - \lambda_\infty$ from Equation 2.70, gives

$$\frac{\sigma C_{l_\alpha}}{2}(\theta_u r^2 - \lambda_r) = 4F\lambda(\lambda - \lambda_\infty)r \tag{2.76}$$

or

$$\lambda^2 + \left(\frac{\sigma C_{l_\alpha}}{8F} - \lambda_\infty\right)\lambda - \frac{\sigma C_{l_\alpha}}{8F}\theta_u r = 0 \tag{2.77}$$

Solving this equation for λ results in

$$\lambda(r, \lambda_\infty) = \sqrt{\left(\frac{\sigma C_{l_\alpha}}{16F} - \frac{\lambda_\infty}{2}\right)^2 + \frac{\sigma C_{l_\alpha}}{8F}\theta_u r} - \left(\frac{\sigma C_{l_\alpha}}{16F} - \frac{\lambda_\infty}{2}\right) \tag{2.78}$$

Thus the upper rotor's inflow equation, found by using the BEMT principles for a single rotor with an axial climb velocity where $V_c = V_\infty$, as discussed by Leishman (2006) can be written as

$$\lambda_u(r, \lambda_\infty) = \sqrt{\left(\frac{\sigma_u(r) C_{l_\alpha}}{16F} - \frac{\lambda_\infty}{2}\right)^2 + \frac{\sigma_u(r) C_{l_\alpha}}{8F}\theta_u(r) r} - \left(\frac{\sigma_u(r) C_{l_\alpha}}{16F} - \frac{\lambda_\infty}{2}\right) \tag{2.79}$$

where $\sigma_u(r)$ and $\theta_u(r)$ are respectively the blade solidity distribution and pitch distribution at radial positions on the upper rotor.

Take note that F in Equation 2.72 is a function of the rotor inflow, λ, and that λ is initially unknown. Therefore Equations 2.78, 2.72 and 2.73 are solved iteratively starting from $F = 1$ (equivalent to $N_b \to \infty$) to calculate λ and then calculating f and F using, $\phi = \lambda(r)/r$ to recalculate and update λ until convergence is achieved.

The same method can be used to analyse the lower rotor. Note that depending on the vertical separation of the rotors, only a certain part of the lower rotor will be affected by the slipstream of the upper rotor. The velocity of the slipstream of the upper rotor can be defined in terms of the radial contraction of the wake, r_c, that is, the contracted wake area is $A_c = \pi(r_c R)^2$. In the ideal case for a fully developed slipstream, the area is $A_c = A/2 \; or \; r_c = 1/\sqrt{2} = 0.707$. For this ideal case the inner area of the lower rotor encounters incoming differential stream tubes with velocity $V_\infty + 2v_u$, or $V_\infty + (A/A_c)v_u$ in the general case.

Using the same steps for the lower rotor, the equation for the inflow distribution can be written as

$$\lambda_l(r, \lambda_\infty) = \sqrt{\left(\frac{\sigma_l(r) C_{l_\alpha}}{16F} - \frac{\lambda_u}{2}\right)^2 + \frac{\sigma_l(r) C_{l_\alpha}}{8F}\theta_l(r) r} - \left(\frac{\sigma_l(r) C_{l_\alpha}}{16F} - \frac{\lambda_\infty + (A/A_c)\lambda_u}{2}\right) \qquad for\ r \le r_c \tag{2.80}$$

where θ_l is the blade pitch distribution on the lower rotor. The inflow distribution for points outside the area A_c, where $r > r_c$, is found by solving

$$\lambda_l(r, \lambda_\infty) = \sqrt{\left(\frac{\sigma_l(r) C_{l_\alpha}}{16F} - \frac{\lambda_u}{2}\right)^2 + \frac{\sigma_l(r) C_{l_\alpha}}{8F}\theta_l(r) r} - \left(\frac{\sigma_l(r) C_{l_\alpha}}{16F} - \frac{\lambda_\infty}{2}\right) \qquad for\ r > r_c \tag{2.81}$$

Equations 2.79 to 2.81 give an estimate of the inflow distribution at separate radial points over both the upper and lower rotors for any prescribed blade pitch,

blade twist distribution and planform shape (in terms of the chord or solidity distribution). The airfoil section is implicitly specified through the effect of lift-curve slope and zero-lift angle of attack (Leishman & Syal, 2008).

With the inflow distributions of both the rotors known, the corresponding thrust and power (induced plus profile) distributions for each can be solved numerically, element by element, using the discretised inflow solution. The total thrust and power are simply found by numerically integrating the equations across each rotor disc. The coefficient of thrust and power for the upper rotor is

$$C_{T_u} = \int_{r=0}^{r=1} dC_{T_u} = 4\int_0^1 {\lambda_u}^2 r dr = \frac{1}{2}\int_0^1 \sigma_u C_l r^2 dr \tag{2.82}$$

and

$$C_{P_u} = \int_{r=0}^{r=1} \lambda_u dC_{T_u} = 4\int_0^1 {\lambda_u}^3 r dr = \int_{r=0}^{r=1} \lambda_u dC_{T_u} + \int_0^1 \frac{1}{2}\sigma_u C_d r^3 dr \tag{2.83}$$

Where C_d is the sectional profile drag coefficient and $C_d \approx C_{d_0}$ for moderate blade loading coefficients. The coefficient of thrust and power for the lower rotor is

$$C_{T_l} = \int_{r=0}^{r=1} dC_{T_l} = \frac{1}{2}\int_0^1 \sigma_l C_l r^2 dr \tag{2.84}$$

and

$$C_{P_l} = \int_{r=0}^{r=1} \lambda_l dC_{T_l} + \int_0^1 \frac{1}{2}\sigma_l C_d r^3 dr \tag{2.85}$$

The two rotors operate at a torque (or power) balance condition where $C_{P_u} = C_{P_l}$ for a prescribed system thrust, $C_T = C_W = C_{T_u} + C_{T_l}$. These two conditions (i.e. thrust balance and torque balance) can be satisfied by a numerically trimming procedure whereby the pitch angles on both the rotors are adjusted iteratively until the required balance conditions are met.

The BEMT applied to a coaxial rotor system is an efficient tool to aerodynamically analyse the coaxial rotors with different twist distributions and planform shapes. In the article by Leishman (2006) a detailed analysis on the use of the BEMT is done in order to find an optimum design for the blade shapes.

2.6 LIFTING LINE MODELS

The lifting line model can be used to represent a high aspect ratio wing by a vortex string, positioned along the ¼ chord line of the wing (the bound vortex). This bound vortex string is also called the lifting line. Since the circulation along the blade is not constant, trailing vortices are shed off the blade forming a helical shape and these vortex lines combine to form helical vortex sheets in the wake. Betz (1919) extended the classic lifting line model for rotating wings as illustrated in Figure 2.8 and defined the conditions for a propeller with maximum efficiency. Betz indicated that the vortex sheets of a most efficient propeller move axially backwards as rigid twisted surfaces. The bound circulation is a function of the radial position $\Gamma_B(r)$ and the circulation of the trailing vortex lines per unit span Γ_T is determined by the conservation of circulation:

$$\Gamma_T(r) = \frac{\Gamma_B(r)}{dl_B} \tag{2.86}$$

where dl_B is the coordinate along the ¼ chord line of the blade. The shape of the helical trailing vortices affects the induced velocities at any point in the flow field. In the free wake model it is assumed that the direction of the trailing vortices coincides with the direction of the local resultant velocity and is thus not acted on by forces. This method is important for hover conditions, but requires that the actual wake geometry needs to be calculated and entails intensive computations (Gur & Rosen, 2008).

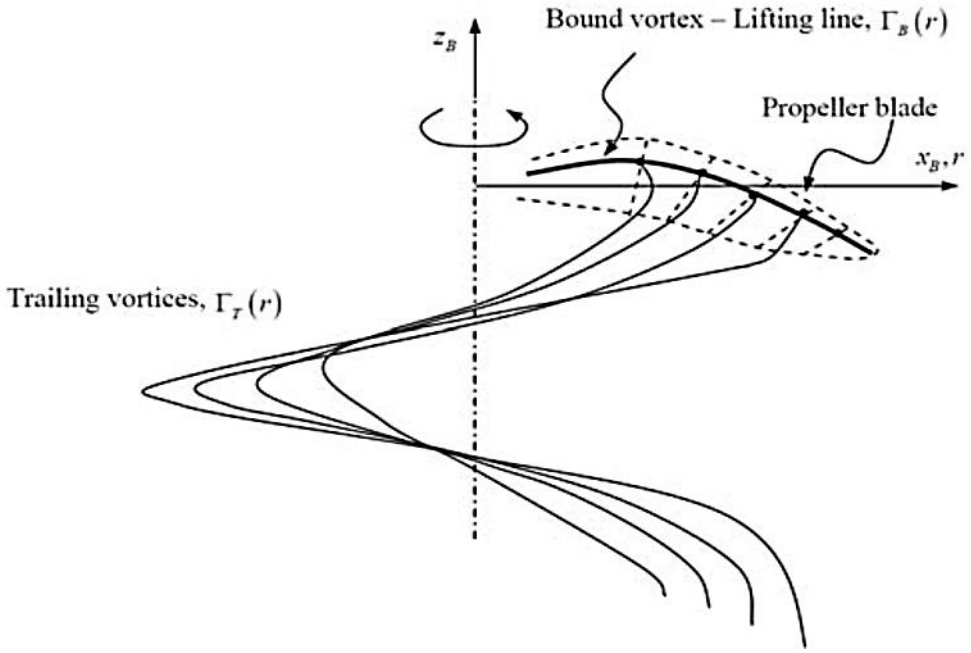

Figure 2.8: The lifting line model (Gur & Rosen, 2008).

In the prescribed wake models it is assumed that each vortex string in the wake has a helical shape with a constant pitch and radius, where the radius is the same as the radius where the trailing vortex string started at the bound vortex. For the fully prescribed wake model, the induced velocity, compared to the tangential velocity, Ω·r and the flight velocity V_F is ignored when defining the wake's pitch:

$$\mathrm{P}_Z(r) = 2\pi \frac{V_F}{\Omega} \tag{2.87}$$

The wake geometry thus stays constant during the whole iterative process. For the semi prescribed wake model, the axial component of the induced velocity is incorporated when defining the wake's pitch:

$$\mathrm{P}_Z(r) = 2\pi \frac{V_F + w_a(r)}{\Omega} \tag{2.88}$$

where $w_a(r)$ is the axial induced velocity in the wake. This velocity is dependent on the wake geometry and thus requires an iterative solution process. Experiments have shown that the difference in accuracy between these models are negligible and suggested that the fully prescribed wake model should be the preferred one except for hovering flight where the free wake model needs to be used, since the free stream velocity in this condition is zero (Gur & Rosen, 2008).

With the wake geometry known, the lifting line model is combined with the blade element model to calculate the induced velocity along the bound vortex by using Biot-Sarvart's law. These velocities are then projected onto the blade element cross section.

2.7 VORTEX MODELS

The vortex models of Theodorsen and McCormick will be discussed here as two methods of calculating the induced velocities along the blades. The assumption of Betz (1919) that the vortex sheets of a most efficient propeller move axially backwards as rigid twisted surfaces, implies that the resultant velocity of the vortex sheets must be normal to the vortex surfaces. Therefore the resultant induced velocities in the far wake will be normal to the resultant velocities there. It was further assumed by McCormick (1967) and Theodorsen (1948) that the cross sectional resultant induced velocity at the rotor disc plane is perpendicular to the resultant velocity as indicated in Figure 2.9. Applying the Momentum theory to rotors with certain assumptions, it was shown that the induced velocity in the far wake is two times the magnitude of the induced velocity at the rotor disc. Therefore the displacement velocity, *w*, in the far wake of the vortex model is also assumed to be twice the value of the displacement velocity at the disc plane. If the displacement velocity and its inflow angle ∅ are known, the circumferential and axial components of the induced velocity can easily be calculated.

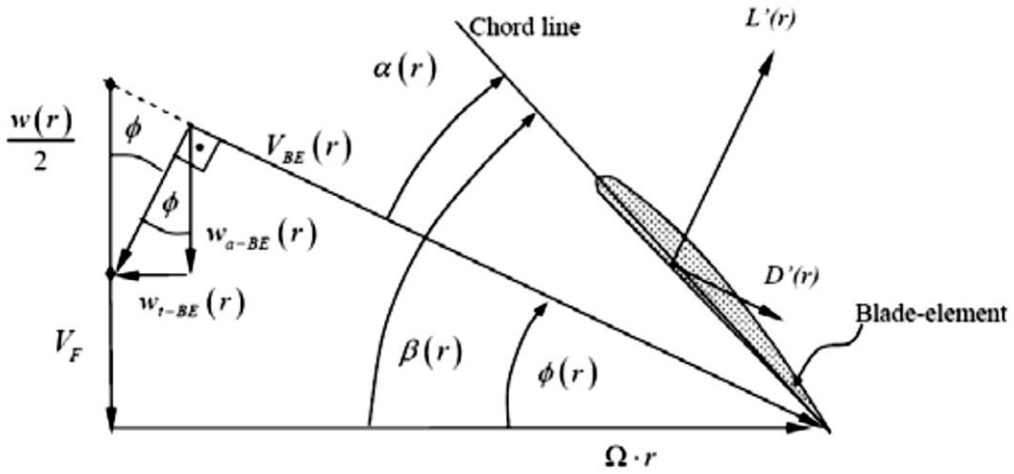

Figure 2.9: The cross sectional velocities of the vortex model (Gur & Rosen, 2008).

2.7.1 Theodorsen's model

In Theodorsen's vortex model the displacement velocity, *w*, *is* expressed as

$$[\mathrm{V}_F + w(r)] \cdot w(r) = \frac{1}{2} \cdot \frac{V_{BE}(r) \cdot \sigma(r) \cdot \Omega \cdot r \cdot \tilde{C}_l(r)}{\mathrm{K}(\mathrm{N_b}, \lambda, \mathrm{r/R})} \tag{2.89}$$

where $\tilde{C}_l(r)$ is the corrected 2D lift coefficient of the blade element and includes effects of the angle of attack ∝, Mach number M, and Reynolds number Re and σ(r) is the local solidity

$$\sigma(r) = \frac{N_b \cdot c(r)}{2\pi r} \tag{2.90}$$

Equation 2.89 is a relation between the displacement velocity and the blade element aerodynamic loading in terms of the coefficient of lift distribution, which is

found from the blade-element model (Theodorsen, 1948). The basis of this equation is the Kutta-Joukowski theory that dictates a relation between the local lift coefficient and the amount of the local circulation. Theodorsen's circulation function, $K(N_b, \lambda, r/R)$ is a function of the number of blades, N_b the radial position of the element r/R and the advance ratio in the far wake, λ which is calculated as

$$\lambda = \frac{V_F}{\Omega \cdot r} \cdot \left(1 + \frac{w}{V_F}\right) \cdot \left(1 + 2 \cdot \frac{w}{V_F} \cdot Y\right) \tag{2.91}$$

where the values of the wake contraction coefficient, Y, are found in the article of Crigler (1948). It is common practice to assume that the pitch angle is constant along the wake when dealing with lightly loaded propellers. In this case the advance ratio in the far wake, λ can be approximated to the tangent to the disc inflow angle, ϕ

$$\lambda \cong \tan \emptyset \tag{2.92}$$

A simplified form of Theodorsen's model as illustrated in Figure 2.9 expresses the displacement velocity as

$$\tan \emptyset = \frac{V_F}{\Omega \cdot r} \cdot \left(1 + \frac{w}{2 \cdot V_F}\right) \tag{2.93}$$

With the axial and circumferential induced velocity components at the blade element cross-section expressed as

$$w_{a-BE} = \frac{w}{2} \cdot \cos^2 \phi \tag{2.94}$$

$$w_{t-BE} = \frac{w}{2} \cdot \cos \phi \cdot \sin \phi \tag{2.95}$$

Equations 2.94 and 2.95 in conjunction with the blade element model can be used to calculate the aerodynamic loads along the blade.

2.7.2 McCormick's model

McCormick's model differs only slightly from Theodorsen's model. He expressed the circumferential induced velocity at the blade element as

$$w_{t-BE}(r) = \frac{V_{BE}(r) \cdot \sigma(r) \cdot \tilde{C}_l(r)}{2 \cdot \kappa(r)} \tag{2.96}$$

where the relation between Theodorsen's circulation function, K and Goldstein's interference velocity coefficient κ is given as (Gur & Rosen, 2008)

$$\kappa = K \cdot \left[1 + \left(\frac{\lambda}{R/r}\right)^2\right] \tag{2.97}$$

The axial induced velocity at the blade element can be found from Figure 2.9

$$w_{a-BE}(r) = -\frac{V_F}{2} + \sqrt{\left(\frac{V_F}{2}\right)^2 + w_{t-BE}(r) \cdot [\Omega \cdot r - w_{t-BE}(r)]} \tag{2.98}$$

Equations 2.97 and 2.98 in conjunction with the blade element model can be used to calculate the aerodynamic loads along the blade.

CHAPTER 3: DESIGN OF THE COAXIAL ROTOR SYSTEM

3.1 INTRODUCTION

The objective of this study was to design a more efficient coaxial rotor for the Aero Flight Dynamics Directorate (AFDD) ducted coaxial rotor system as published by Lee (2010). It was decided to use simple fixed-pitch coaxial rotors attached to a direct drive electric motor to ensure mechanical robustness with reliable and safe operation and minimum skilled maintenance. In this configuration the thrust is varied by changing the rotor rotational speed rather than changing the pitch of the rotor blades as is required when using the traditional helicopter rotor. The traditional rotor requires a mechanically complex swash plate mechanism and tail rotor system. In this study the rotor radius was dictated by the inner geometry of the shroud used by Lee (2010), which was set at 0.1778 m. This resulted in a tip Mach number of 0.278 and 0.322 for a rotor speed of 5 000 and 6 000 rpm respectively, which would ensure incompressible flow conditions. From experimental data published by Lee (2010) it was decided to base the design on two conditions:

- To design the rotors to deliver the maximum thrust in hover with an input power of 370 W at a design rotor speed of 5 000 rpm.
- To achieve a torque balance for the coaxial rotors with each rotor operating at the same rotational speed, ranging from 3 000 to 7 500 rpm.

3.2 THE DUCTED FAN DESIGN CODE (DFDC)

DFDC was specifically developed for the design and analysis of a ducted propulsor with single or multiple blade rows. It is a simple two-dimension code where the rotor blade representation is based on a lifting-line formulation as described in paragraph 2.6. The duct and hub is modelled with the panel method scheme that is also used in the XFOIL code.

The code combines the blade element theory presented in paragraphs 2.4 and 2.5 for the blade row sections and the vortex theory together with the two-dimensional lift, moment and profile drag characteristics to determine the rotor blade performance. The induced velocities associated with the blade-row loading are represented by vortex sheets shed into the flow field as described in paragraph 2.7. The vortex theory with the Betz and the Glauert laws are used to optimize the blade geometry for a specified thrust, power or torque.

DFDC is designed for rapid shrouded rotor design and analysis. The code works with a single input file in text format which contains the shroud case data, the shroud geometry data, actuator disk or rotor blade data and drag source data. Its aerodynamic outputs are the shroud forces and moments and the rotor and stator forces. Amongst others, DFDC's analysis capabilities include a shroud with an actuator disk or rotor blade, a stator modelled as actuator disk or as a bladed disk. The user can specify the rotor or stator axial position, the free-stream velocity and the rotor RPM, and with these DFDC will then drive the solution to a specified thrust output. The effects of duct drag sources can also be investigated. DFDC has the capability to design the rotor or stator blade chord to a specified circulation and the blade twist for a specified chord and circulation. The rotor blade design in DFDC is exported into CAD for subsequent 3D modelling and meshing with the ESLOFT tool that is fully integrated with DFDC for generating accurate lofts.

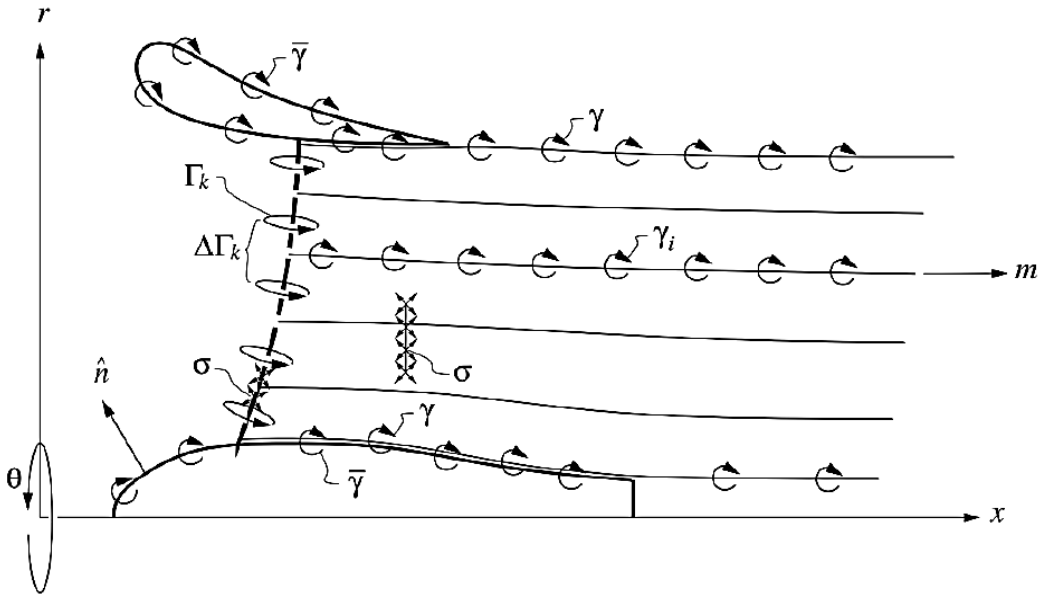

Figure 3.1: The vortex presentation of the shroud, hub and rotor in DFDC (Drela & Youngren, 2005).

The DFDC code and user manual is available online at http://www.esotec.org/sw/DFDC.html.

3.3 SHROUD DESIGN

For the shrouded rotor to be viable, the increase in total thrust must be more than the additional weight of the shroud.

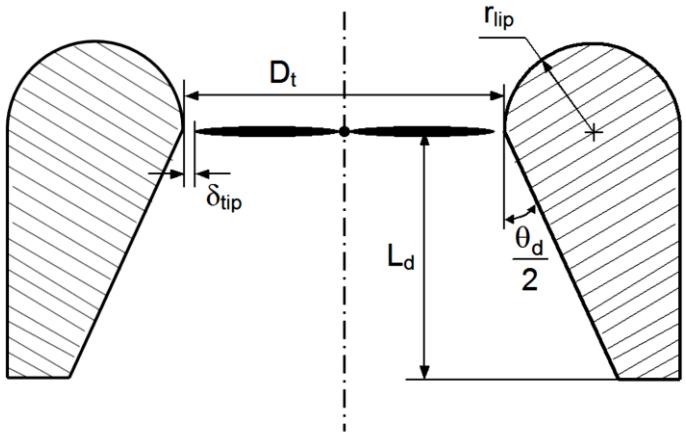

Figure 3.2: Shroud design parameters (Pereira 2008).

Pereira (2008) identified an optimum combination of design parameters for a shrouded rotor on a MAV scale to minimize the losses due to the increased weight of the shroud as indicated in Figure 3.1. His main conclusions were:

- A blade tip clearance $\delta_{tip} < 0.012R$ will generally result in good performance.
- The diffuser length (L_d) is less important than the diffuser angle(θ_d), a value of $\theta_d \approx 10°$ gave the best results.
- Moderate increases in thrust (or decreases in power required) were experienced when the diffuser length was increased from 31% to 50% of

the throat diameter (D_t). The improvement was less significant with a further increase to 72% D_t. It was found that a diffuser expansion ratio between 1.22 and 1.31 generally resulted in better performance, where the expansion ratio is expressed as

$$\sigma_d = \frac{A_e}{A} = \left[1 + 2\frac{L_d}{D_t}\tan\left(\frac{\theta_d}{2}\right)\right]^2 \tag{3.1}$$

- The external part of the shroud leading edge plays a less important role in thrust production. Thus, to save weight, reducing the lip radius in this region might be considered.

Hrishikeshavan (2011) applied simple momentum theory to determine the upper limit for the shroud weight as described below:

If W_{IR} is the weight of the isolated rotor MAV, W_{Shroud} the weight of the shroud and W_{SR} the weight of the shrouded MAV, then

$$W_{SR} = W_{Shroud} + W_{IR} \tag{3.2}$$

The total power required by a rotor can be expressed as

$$P = P_0 + P_i \tag{3.3}$$

The profile power (P_0) is primarily a function of the airfoil drag coefficient and rotor solidity, while the induced power (P_i) is largely determined by the structure of the wake. For the same rotor configurations, it follows that the induced power will be the main reason for differences in power consumption between an isolated rotor and shrouded rotor. Thus, for a favourable shroud design:

$$P_{i_{SR}} < P_{i_{IR}} \tag{3.4}$$

In coefficient form:

$$C_{P_{i_{SR}}} < C_{P_{i_{IR}}} \tag{3.5}$$

From simple momentum theory, for a given expansion ratio σ_d, the induced power coefficient is given by:

$$C_{P_i} = \kappa \frac{W^{3/2}}{\sqrt{4\sigma_d \rho A}} \tag{3.6}$$

Where, κ is the induced power factor accounting for non uniform inflow, tip losses and swirl effects, W is the weight of the MAV, A is the rotor disk area which is constant. Thus, for

$$C_{P_{i_{SR}}} < C_{P_{i_{IR}}} \tag{3.7}$$

It is necessary that

$$\kappa_{SR} \frac{W_S^{3/2}}{\sqrt{4\sigma_d \rho A}} < \kappa_{IR} \frac{W_{US}^{3/2}}{2\rho A} \tag{3.8}$$

Thus,

$$\frac{W_{SR}}{W_{IR}} < \left(\frac{\kappa_{IR}}{\kappa_{SR}}\right)^{2/3}(2\sigma_d)^{1/3} \tag{3.9}$$

Since the tip vortices and therefore the induced losses from a shrouded rotor are anticipated to be lower than for an isolated rotor, $\kappa_{IR} > \kappa_{SR}$. By assuming $\kappa_{IR} \sim \kappa_{SR}$, a conservative calculation for the weight of the shroud can be made from Equations 3.10 and 3.11

$$\frac{W_{Shroud}}{W_{IR}} < ((2\sigma_d)^{1/3} - 1) \tag{3.10}$$

Hence, for $\sigma_d = 1$, $\frac{W_{Shroud}}{W_{IR}} < 0.26$ to ensure an improved power loading for the shrouded MAV.

3.3.1 Shroud specifications

The shroud used for the present work consists of the same cambered leading edge shroud and the symmetrical NACA derivative trailing edge as used by Lee (2010) in his research. Apart from the leading edge, the inner surface of the shroud is flat to ensure the same inner diameter and tip clearance for any rotor station within the shroud. The shroud airfoil is defined in terms of a leading edge and a trailing edge segment and each segment consists of an inner and an outer surface. The shroud throat (or minimum inner) diameter D_t is 0.3592 m to ensure a nominal tip clearance of 0.01R (0.001778 m) and the shroud chord c_d is set at 0.2052 m.

3.3.2 Cambered leading edge

The cambered leading edge is a variant of the Küchemann airfoil and consists of a pair of elliptical shapes that form the interior and exterior surfaces of the shroud inlet. The shape is described by four constants K_1, K_2, K_3, K_4 and the ratio between the inner and outer cross-sectional areas of the shroud, A_i/A_m. By changing these parameters the shroud geometry, like the leading edge nose roundness or the size of the interior or exterior lengths can be altered. The shroud inner radius is R_i = 1.01R (0.1798 m) and the maximum shroud thickness is t_d = 0.0254 m to leave enough space for the internal shroud structures. It follows that the shroud outer radius R_m is described as

$$R_m = R_i + t_d \quad \text{and} \tag{3.12}$$

$$A_i/A_m = R_i^2/R_m^2 = 0.76752 \tag{3.12}$$

The cambered airfoil leading edge was generated by the equations:

$$y_{K_m} = R_0 + (R_m - R_0)\sqrt{1 - \left(1 - {}^{x}/_{L_m}\right)^2} \qquad 0 \le x \le L_m \tag{3.13}$$

$$y_{K_i} = R_0 - (R_0 - R_i)\sqrt{1 - \left(1 - {}^{x}/_{L_i}\right)^2} \qquad 0 \le x \le L_i \tag{3.14}$$

$$y_{K_i} = R_i \qquad L_i \le x \le L_m \tag{3.15}$$

where R_0 is the leading edge centre radius, L_m the outer length and L_i the inner length which are all defined in terms of the Küchemann constants (Küchemann, 1953).

$$R_0 = K_1 R_i \tag{3.16}$$

$$L_m = \frac{R_m}{K_2 + K_3 \left(\frac{A_i}{A_m}\right)^3} \tag{3.17}$$

$$L_i = K_4 (K_1 - 1) R_i \tag{3.18}$$

For the current design K_1 = 1.05, K_2 = 0.20, K_3 = 8.58 and K_4 = 1.50. The outer length L_m specifies the overall length of the leading edge segment, therefore the NACA trailing edge begins at x = L_m = 0.245c_d (0.050247 m).

3.3.3 NACA trailing edge

The equations for the shroud exterior and interior surfaces of the trailing edge originate from a NACA symmetrical airfoil and are defined by Lee (2010, 34) as

$$y_{TE_m} = 10 t_d \left(A \sqrt{\frac{x}{c_s} + T\left(\frac{x}{c_s}\right)} + B\left(\frac{x}{c_s} + T\left(\frac{x}{c_s}\right)\right) + C\left(\frac{x}{c_s} + T\left(\frac{x}{c_s}\right)\right)^2 + D\left(\frac{x}{c_s} + T\left(\frac{x}{c_s}\right)\right)^3 + E\left(\frac{x}{c_s} + T\left(\frac{x}{c_s}\right)\right)^4\right) \tag{3.19}$$

$$y_{TEi} = 0 \qquad L_m \leq x \leq c_d \tag{3.20}$$

where the values of the constants are: $A = 0.2969$, $B = -0.1260$, $C = -0.3516$, $D = 0.2843$ and $E = -0.1015$.

The combination of the Küchemann leading edge surfaces and the NACA trailing edge surfaces forms the cambered shroud airfoil as shown in the Figure 3.2.

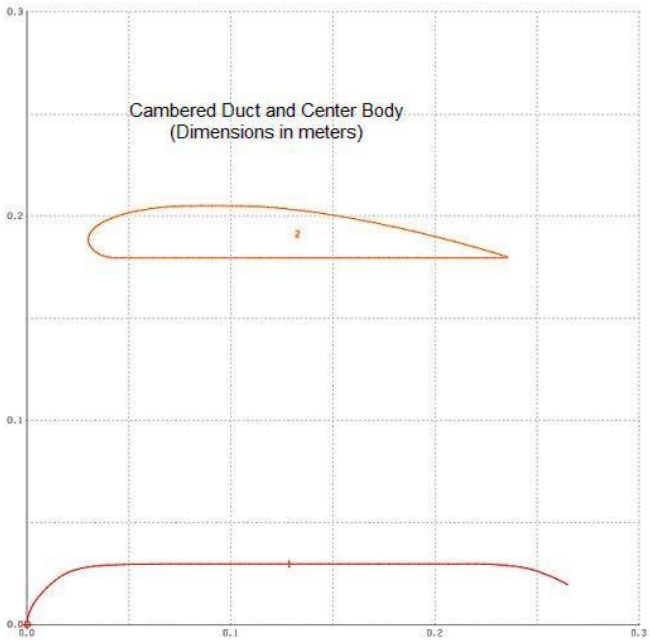

Figure 3.3: The cambered shroud airfoil and symmetrical centre body.

3.3.4 Centre body specifications

The cylindrical centre body of the current design has a radius equal to the rotor hub radius of 0.167R (0.02969 m) as used by Lee (2010) in his research. A close variant of a semi-circle leading edge is used to ensure convergence in DFDC, whilst the trailing edge protrudes from the shroud and is slightly tapered towards the centreline. Apart from housing the electrical motors, batteries and flight avionics, the vehicle's centre of gravity can be controlled by carefully shifting these items in the centre body.

3.4 UAV ROTOR BLADE DESIGN

The design of high performance simple fixed-pitch rotors with optimum low Re number airfoils for small scale UAVs is a trade-off between optimal aerodynamic performance and ease of manufacturing. According to Hrishikeshavan (2011), the ideal profile will be very thin (in the order of 2%), highly cambered (in the order of 10%) with a sharpened leading edge, but in reality these airfoils are difficult to manufacture.

Furthermore, these thin airfoils deform easily due to aerodynamic torque on the blades under load conditions. The design of small-scale fixed-pitch rotor blades is thus also a trade-off between best aerodynamic design and best structural design.

The blades must be rigid enough to ensure that the aerodynamic moment due to lift is being balanced by the elastic torque due to twisting (Pounds & Mahony, 2004). Unbalanced aerodynamic blade pitching moments will increase the angle of attack of the airfoil, resulting in an even higher blade pitching moment. Insufficient elastic restoring torque will cause the blades to twist until they stall. At the equilibrium angle, the torsional strain along the blades will be balanced by the continuous deformation due to the aerodynamic bending moments of the blades.

The three major aspects of rotor design are the rotor tip velocity (determined by the rotor speed and diameter), the profile section and the planform, which is determined by the chord and twist distribution. The blade planform should be designed in such a way to ensure that the equilibrium angle of each blade section along the radius is also the ideal AoA. Tapering the blade towards the blade tip generally helps to enhance the efficiency of the rotor (Hrishikeshavan, 2011).

The goal of the blade design is to ensure maximum thrust at steady state for a given power supplied to the rotor shaft. This means that the blade AoA and Re number should be optimal for the airfoil to ensure a high lift to drag (L/D) ratio.

The Re range for most small scale UAV rotor blades is in the order of 50 000 to 150 000 and as such it can be expected that the flow in this regime will be laminar and that the aerodynamics will be mainly influenced by viscous effects (Pounds & Mahony, 2004). High aerodynamic rotor efficiency is guaranteed by maximum rotor radius, but the rotor radius is always constrained by the geometry of the UAV and manufacturing limitations. For small blades to generate maximum thrust it is required that the rotor speed must be as high as possible (Leishman, 2000). In contrast, the rotor speed is restricted by the available drive torque and the rotor tip Mach number. It is generally accepted that tip Mach numbers below 0.3 will ensure negligible compressibility effects.

The ideal airfoil shape for these small scale UAV rotors is a high aspect ratio blade section. Minimum profile drag will be ensured by a profile with a limited

camber and a thin cross section, while a sharp trailing edge will keep the separation drag to a minimum (Pounds & Mahony, 2004).

3.4.1 Rotor blade profile selection

The profile selection for the rotor blades was done by dividing the blade into three Re number regions namely: 60 000 < Re > 80 000 for the first third inner section of the blade, 80 000 < Re > 110 000 for the middle section and 110 000 < Re > 150 000 for the outer section of the blade. To ensure structural integrity and ease of manufacturing, a thickness to chord ratio (t/c) in the order of 18%, 14% and 10% respectively were chosen for the three sections. Comparative searches within the online airfoil databases, Airfoil Tools (Airfoil Tools, n.d.) and The Incomplete Guide to Airfoil Usage by Lednicer (2010), were made for rotorcraft/propeller airfoils with regards to their lift and drag polar diagrams within the relevant Re number ranges. Airfoils that would deliver high L/D ratios over an adequate range of AoAs where their lift curve slopes stay constant were selected.

The airfoil comparative search resulted in five sets of profiles being selected, namely the ARA-D13-D10, DAE 11-21-31-51, EPPLER 855-854-852, NACA 2418-2414-2410 and MH 112-114-115-117-121 series (Airfoil Tools, n.d.). All these sections were designed for propellers or rotors for ultra-light aircraft operating in low Reynolds number flows. Analyses of these profiles were done by producing airfoil polars with the analytical tool XFOIL (Drela, 2004). A short description of XFOIL can be found in (Drela, 1989) and the code and user manual is available online at http://web.mit.edu/drela/Public/web/xfoil.

The aerodynamic data of these five sets of profiles were then used in Drela's Ducted Fan Design Code (DFDC) to do a preliminary rotor design. The same geometric data of the cambered duct used in Lee's experiments and a cylindrical hub with a circular nose section were used to host the rotor blades in the DFDC code.

Figure 3.3 shows the total loads for the hover performance of the cambered duct with a coaxial rotor for the different profile sets as predicted with the DFDC code. For the comparison between the different airfoil sets, the tip gap was set to 0 mm and no provision was made for the blade blockage effect. The results indicated that the ARA-D13-D10 and the NACA 2418-2414-2410 profile sets performed the best, with the first only marginally better than the latter. This result is in agreement with previous research that indicated that thinner airfoils will give better performance (Hrishikeshavan, 2011). In almost all of the designs an increase in thrust of more than 20% for the same power input as in Lee's experiments was achieved. After comparing the different rotors at design point and away from the design point it was decided to use the NACA 2418-14-08 sections. Not only are they aerodynamically better than the other airfoils, but their much simpler geometry should result in easier manufacturing.

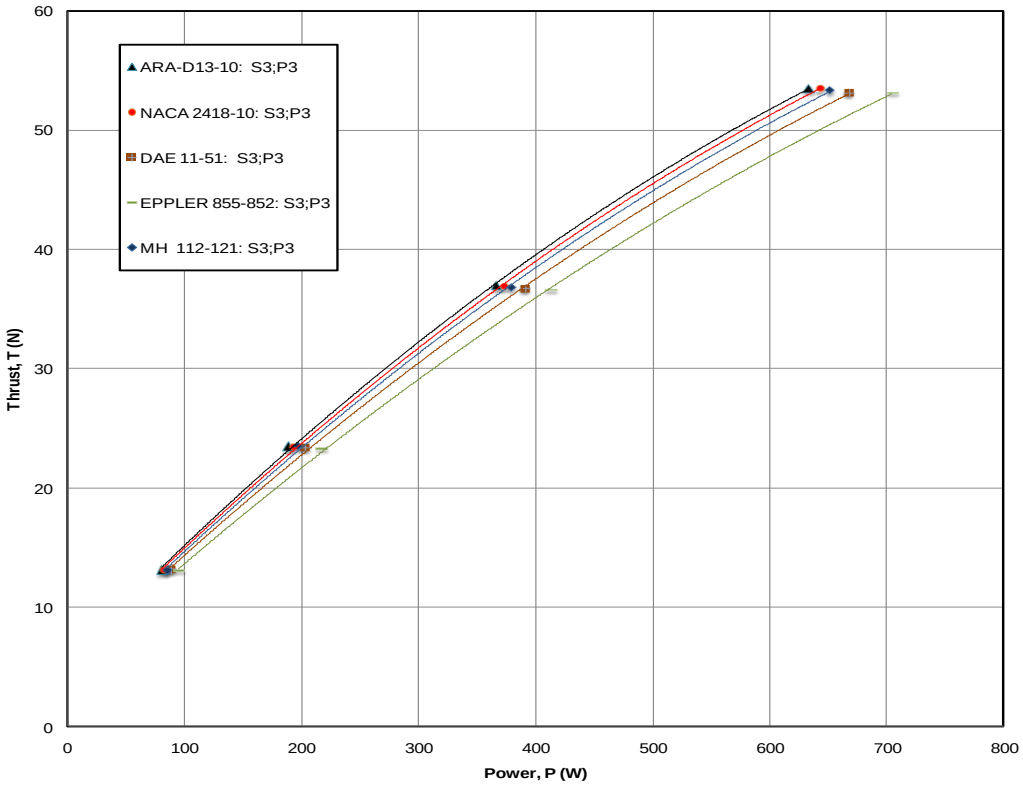

Figure 3.4: The total loads for hover performance of the cambered duct with a coaxial rotor for different profiles sets.

The aerodynamic polar diagrams for the NACA 2418-14-10 profiles can be found in Appendix A.

3.4.2 Final rotor blade design

With the blade profile set having been selected, the final rotor blade design was done with the DFDC code. In the initial design each rotor consisted of three rotor blades to closely resemble the rotors that were used in Lee's experiments. It was later decided to decrease the number of blades to two, which allowed an increase in blade chord length and Reynolds number. The rotors were designed at sea level conditions with the density (ρ) set at 1.226 kg/m^3, the viscosity (v) equal to 0.178E-04 kg/m/s and the speed of sound (a) equal to 340 m/s. An example of an input file used in the DFDC code is presented in Appendix B.

3.4.3 Rotor blade geometry

The rotor blade geometry for the upper and lower rotor is summarised in Tables 3.1 and Table 3.2 respectively. Further rotor details are shown in Appendix C and Appendix D.

Table 3.1 Upper rotor geometric data.

Lofted Blade	CRR-S3P3-NACA 2418-14-10		Disk 1	Upper Rotor		Rotor Rotation:	Positive	
Parents Airfoils	**NACA 24 series**	**t/c**	**@ x/c**	**Camber**	**@ x/c**	**Radius_le**	**Thickness_te**	**A0 (deg)**
1	NACA_2418	0.18	0.2998	0.0200	0.4021	0.0354	0.0038	-0.90
2	NACA_2414	0.14	0.2998	0.0200	0.4018	0.0213	0.0029	-1.46
3	NACA_2410	0.10	0.2997	0.0200	0.4023	0.0110	0.0021	-1.20

Points per side	60	Density -le/te	8.00		
Stations Spec	16	Distribution	Linear t/c	Density-hub/tip	1.50
Rotor Tip Gap (mm)	1.78	PitchAxisHub-x/c	0.35	PitchAxisTip	0.35

Station	Radius (cm)	Chord (cm)	Beta (deg)	Alpa 0 (deg)	Thickness (mm)	t/c
1H	2.97	5.38	58.47	-0.900	9.69	0.18
2	3.76	4.78	50.71	-0.960	8.40	0.18
3	4.59	4.24	44.09	-1.022	7.27	0.17
4	5.44	3.78	38.77	-1.087	6.30	0.17
5	6.32	3.39	34.66	-1.153	5.50	0.16
6	7.22	3.08	31.37	-1.221	4.83	0.16
7	8.15	2.81	28.62	-1.292	4.28	0.15
8	9.11	2.59	26.32	-1.365	3.80	0.15
9	10.10	2.40	24.37	-1.439	3.40	0.14
10	11.12	2.24	22.75	-1.434	3.05	0.14
11	12.16	2.10	21.35	-1.397	2.74	0.13
12	13.23	1.99	20.13	-1.360	2.48	0.12
13	14.32	1.89	19.02	-1.321	2.24	0.12
14	15.45	1.80	17.99	-1.282	2.03	0.11
15	16.60	1.73	17.03	-1.241	1.84	0.11
16T	17.78	1.68	16.11	-1.200	1.68	0.10

Table 3.2 Lower rotor geometric data.

Lofted Blade	CRR-S3P3-NACA 2418-14-10		Disk 2	Lower Rotor		Rotor Rotation:	Negative	
Parents Airfoils	**NACA 24 series**	**t/c**	**@ x/c**	**Camber**	**@ x/c**	**Radius_le**	**Thickness_te**	**A0 (deg)**
1	NACA_2418	0.18	0.2998	0.0200	0.4021	0.0354	0.0038	-0.90
2	NACA_2414	0.14	0.2998	0.0200	0.4018	0.0213	0.0029	-1.46
3	NACA_2410	0.10	0.2997	0.0200	0.4023	0.0110	0.0021	-1.20

Points per side	60	Density -le/te	8.00	Beta Coords	Global
Stations Spec	16	Distribution	Linear t/c	Density-hub/tip	1.50
Rotor Tip Gap (mm)	1.78	PitchAxisHub-x/c	0.35	PitchAxisTip	0.35

Station	Radius (cm)	Chord (cm)	Beta (deg)	Alpa 0 (deg)	Thickness (mm)	t/c
1H	2.97	4.56	126.57	-0.900	8.20	0.18
2	3.76	4.16	131.76	-0.960	7.31	0.18
3	4.59	3.79	136.39	-1.022	6.50	0.17
4	5.44	3.46	140.40	-1.087	5.77	0.17
5	6.32	3.17	143.77	-1.153	5.13	0.16
6	7.22	2.91	146.63	-1.221	4.58	0.16
7	8.15	2.69	149.07	-1.292	4.09	0.15
8	9.11	2.50	151.17	-1.365	3.67	0.15
9	10.10	2.33	152.98	-1.439	3.30	0.14
10	11.12	2.19	154.56	-1.434	2.98	0.14
11	12.16	2.07	156.07	-1.397	2.69	0.13
12	13.23	1.96	157.46	-1.360	2.44	0.12
13	14.32	1.86	158.70	-1.321	2.21	0.12
14	15.45	1.78	159.85	-1.282	2.01	0.11
15	16.60	1.71	160.91	-1.241	1.82	0.11
16T	17.78	1.65	161.88	-1.200	1.65	0.10

CHAPTER 4: CAMBERED SHROUDED COAXIAL ROTOR SYSTEM (CSCRS) PERFORMANCE

4.1 INTRODUCTION

This chapter presents the results of the design and performance predictions obtained from DFDC. The hover performance and the axial flight performance of the newly designed NACA 2418-14-10 Cambered Shroud Coaxial Rotor System (CSCRS) are compared to the experimental results published by Lee (2010).

4.2 CSCRS HOVER PERFORMANCE

Figure 4.1 compares the hover performance of the Lee rotors to the DFDC designed rotors, both using the same cambered shroud of Lee. Two combinations of rotor-to-rotor spacings (S3 and S4) and three rotor-to-shroud positions (P1, P3 and P4) were used in this comparison. These simulations were all done with a nominal rotor tip gap set at 0.01R. Note that due to the larger root chord of the DFDC rotors it was not possible to reduce the rotor-to-rotor spacing below a value of 0.30R. It is clear that the DFDC rotors outperform the rotors used by Lee over the entire power range. In the operating region of the design point, where the required power is 363 W, the DFDC S3;P3 rotor system delivers 67.45% more thrust than the equivalent Lee rotors.

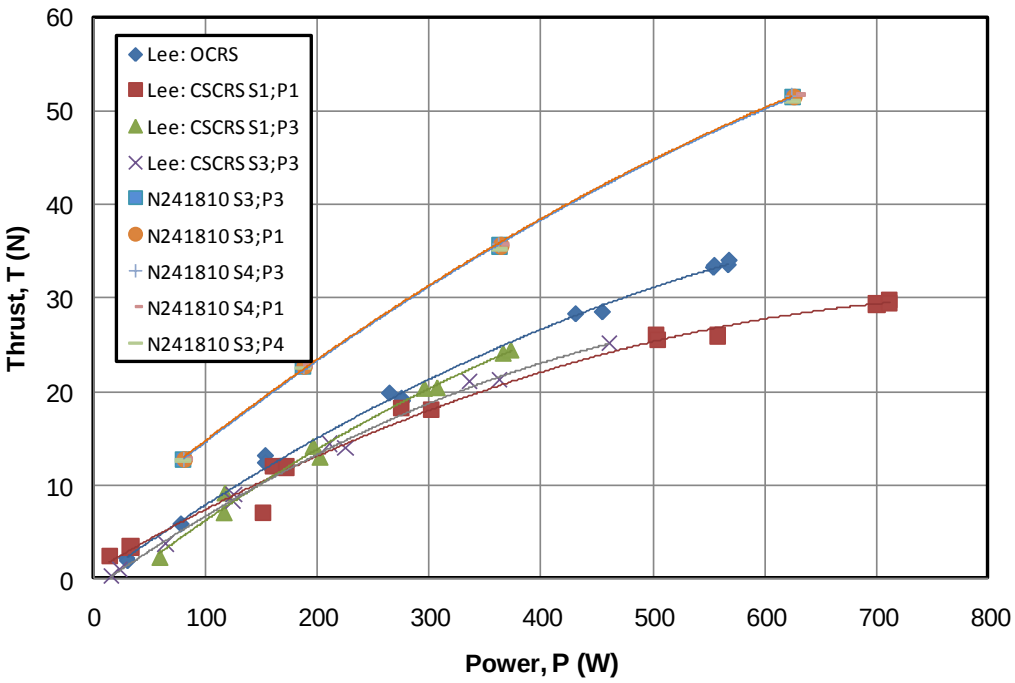

Figure 4.1: A comparison between the Lee CSCRS and the N241810 CSCRS in terms of hover performance at various rotor-to-rotor spacings and rotor-to-shroud positions.

Unlike the experimental data of Lee that indicated that the best hover performance was obtained with the rotors closely spaced and positioned further back in the shroud, DFDC predicts very little difference in hover performance for the various rotor-to-rotor spacings and rotor-to-shroud positions. This insensitivity to rotor spacing and position of the DFDC simulation may be due to the

cylindrical centre body and straight inner flow section of the shroud, resulting in a constant inner area duct.

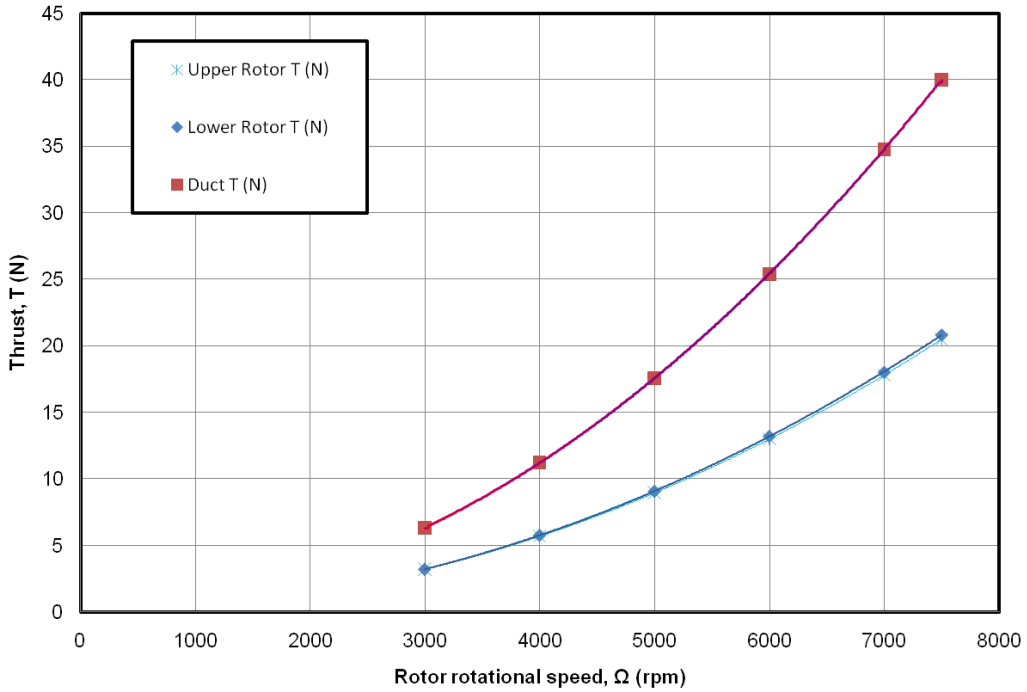

Figure 4.2: Load distribution for the hover performance of the N241810 CSCRS with a 0.01R tip gap and S3;P3 spacing.

The load distribution between the shroud and the rotors is presented in Figure 4.2. The DFDC results indicate that approximately the same amount of thrust is being generated by the upper rotor and the lower rotor and that the rotors and the shroud share about 50% of the total trust.

Figure 4.3 represents the torque distribution in hover between the upper and the lower rotors of the DFDC shrouded coaxial rotor system. It is clear that the torque is almost equally shared between these rotors over the entire rotor speed range. A total torque in the order of 0.001 Nm at 3 000 rpm, increasing slightly to 0.006 Nm at 7 500 rpm is predicted by DFDC.

The power loading (PL) is the direct ratio of thrust developed to the power required by the system and is an indication of the efficiency of the system. Figure 4.4 compares the power loadings of the rotors used by Lee and the DFDC rotors at the same disc loadings (DL). Note that these rotors have the same area and will thus have the same DL at the same thrust. It can be seen that to produce 25 N thrust, the PL of the DFDC rotors is in the order of 75% higher than that of the Lee rotors, which means that considerably less power is required by the DFDC rotors to produce the same amount of thrust.

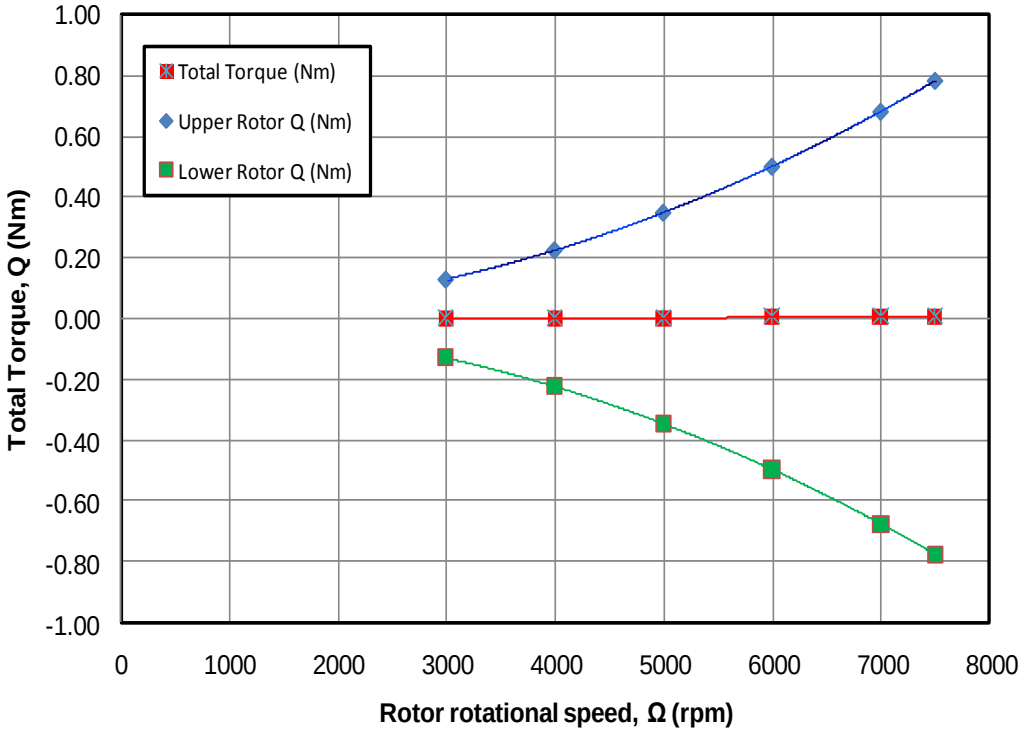

Figure 4.3: Net torque for hover performance of the N241810 CSCRS with a 0.01R tip gap and S3;P3 spacing.

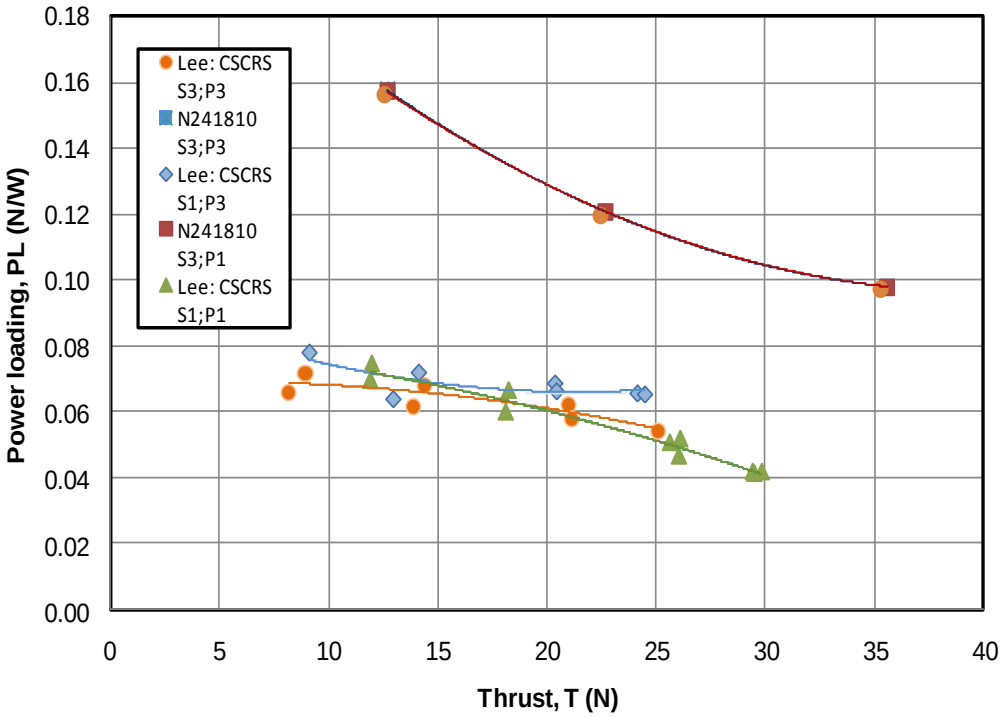

Figure 4.4: A comparison between the Lee CSCRS and the N241810 CSCRS in terms of the power loading for hover performance at various rotor-to-rotor spacings and rotor-to-shroud positions.

The Lee rotors recorded the best PL for the S1 rotor-to-rotor spacing and the P3 rotor to shroud position, while rotor spacing and position have a negligible effect on the PL for the DFDC rotors.

The figure of merit (FM) is used as an indication of the static thrust efficiency of a rotor and is the ratio of the ideal (or the least possible) amount of power required to produce a specified thrust, to the actual amount required by the rotor. From Figure 4.5 it can be seen that DFDC predicts an FM in the order of 83% when delivering 35.4 N thrust for the S3;P3 configuration. At this condition, the shrouded coaxial rotor system with nominal tip gap requires power of 363 W. DFDC predicts a marginally higher FM when the rotor-to-rotor spacing is the largest and the rotors are positioned further back in the shroud.

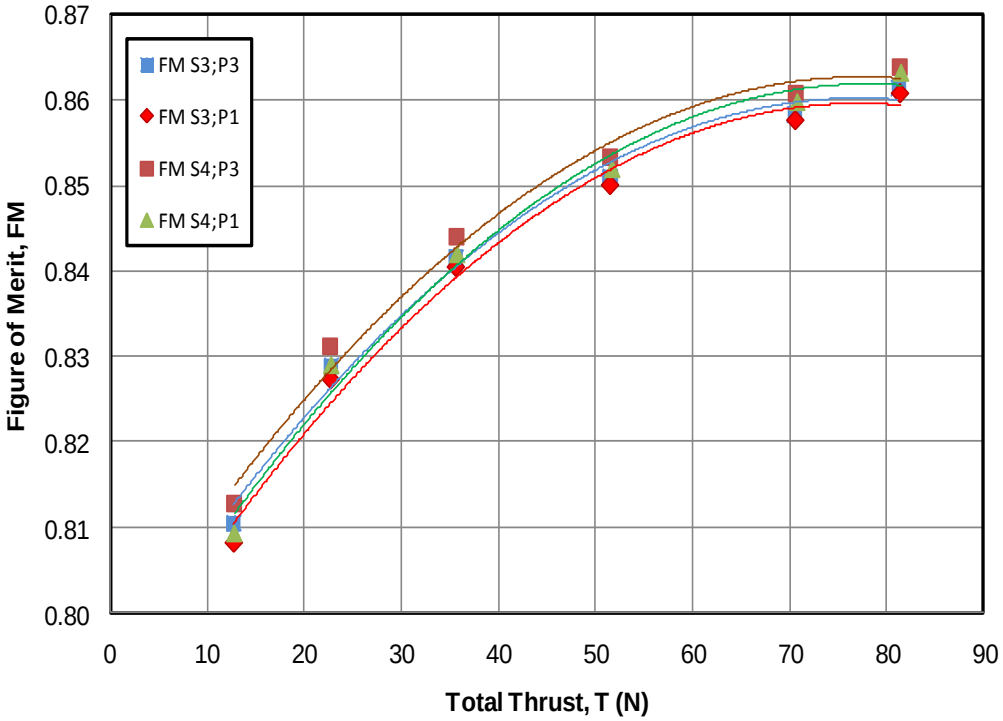

Figure 4.5: Figure of Merit (FM) for hover performance of the N241810 CSCRS with a 0.01R rotor tip gap.

The effect of tip-gap clearance on the performance of the shrouded coaxial rotor system for the S3;P3 spacing is shown in Figure 4.6. An increase in the tip gap reduces the total thrust of the system. From the figure it can be seen that an increased tip gap mainly reduces the shroud thrust while the rotor thrust is less affected by the increased tip clearance.

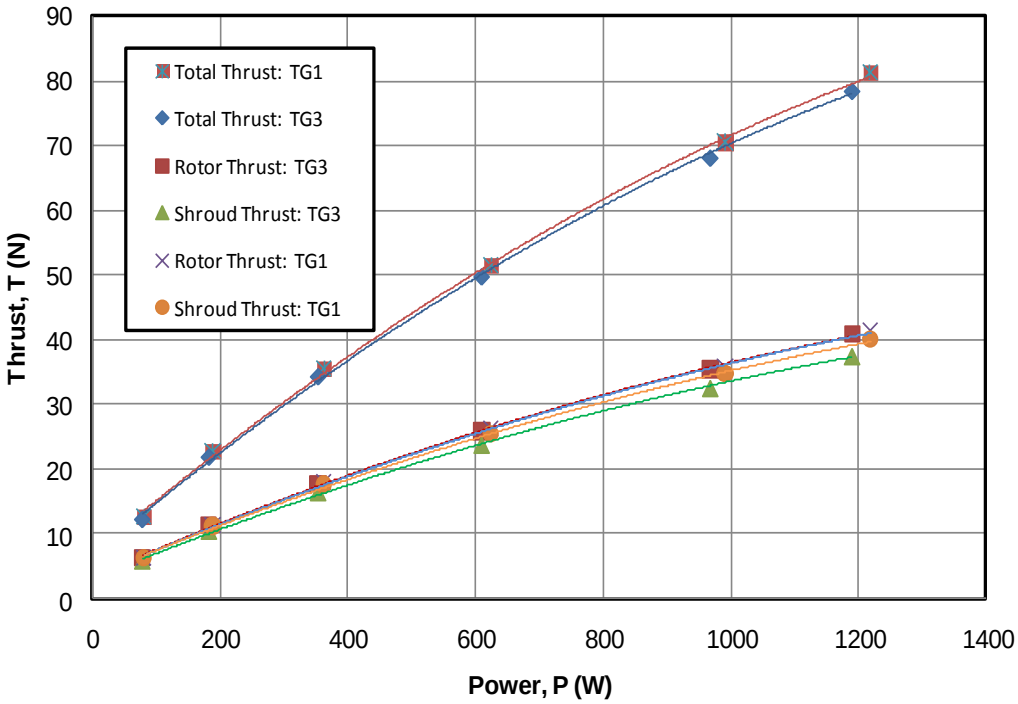

Figure 4.6: Hover performance in terms of total loads and load distribution for the N241810 CSCRS in the S3;P3 rotor position at various rotor tip gaps.

4.3 CSCRS PERFORMANCE IN AXIAL FLIGHT

The axial flight performance of the shrouded rotor system was investigated to assess the effect of rotor-to-rotor spacing, the rotor-to-shroud position, the shroud performance and the rotor tip gap at various inflow velocities. For a fixed pitch rotor configuration axial flow through the rotor increases the inflow angle which in turn will decrease the angle of attack of the blade section, resulting in a decrease of thrust by approximately the square of the inflow velocity. A lower thrust will decrease the rotor torque and the power required to turn the rotor.

If the inflow velocity is increased to a value where the inflow angle increased to the point where the effective angle of attack is zero, the rotor will produce zero thrust. This point is the beginning of the rotor brake state, where after any increase in inflow velocity will result in negative rotor thrust. It was found that the rotors designed in this study reached the brake state at an axial velocity of approximately 28 m/s for the design rotational speed of 5 000 rpm with the lower rotor reaching this state only fractionally before the upper rotor.

Figure 4.7 represents the total loads (shroud and rotors) for the axial flight performance of the shrouded coaxial rotor system at various inflow velocities and rotor positions. The figure clearly illustrates that for a given power input the total thrust delivered by the system decreases with increasing axial velocity. Generally the axial flight performance of the shrouded coaxial rotor system used in this study seems not to be affected by the rotor-shroud position, as was the case with the hover performance. It was thus decided to use only the S3;P3 rotor-to-rotor spacing and rotor-to-shroud position for the remainder of the axial flight performance investigation.

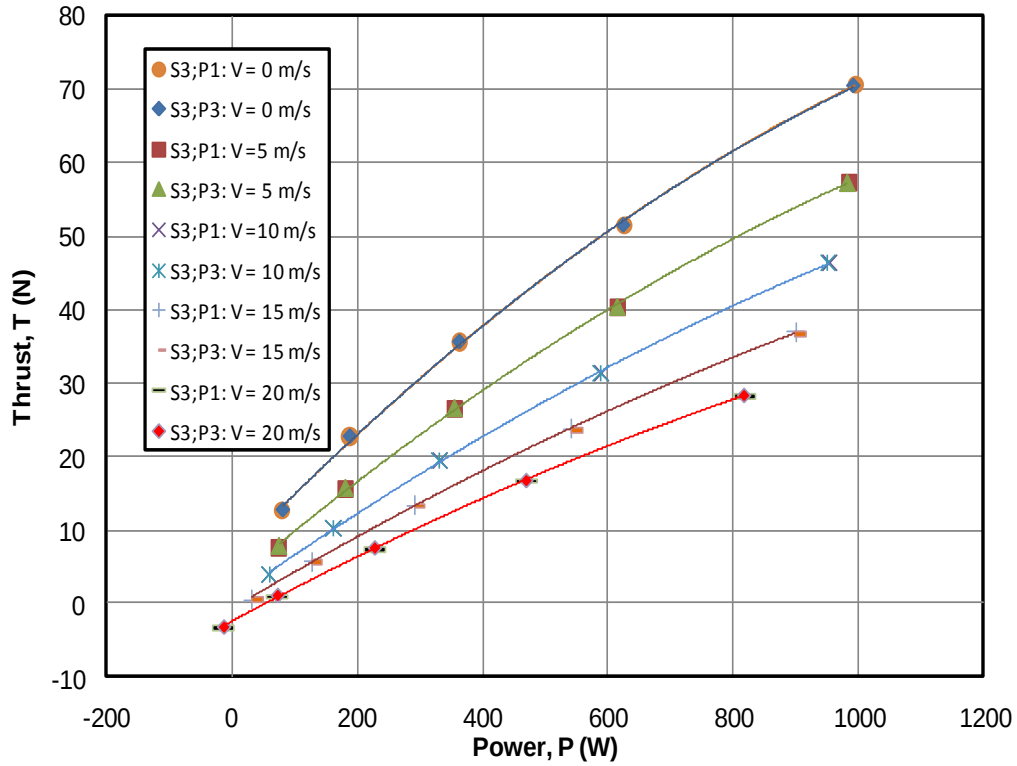

Figure 4.7: Total loads for axial flight performance of the N241810 CSCRS at various rotor-to-rotor spacings and rotor-to-shroud positions. Tip gap is 0.01R.

The composition of the total loads generated in axial flight conditions at increasing speeds is given in Figure 4.8.

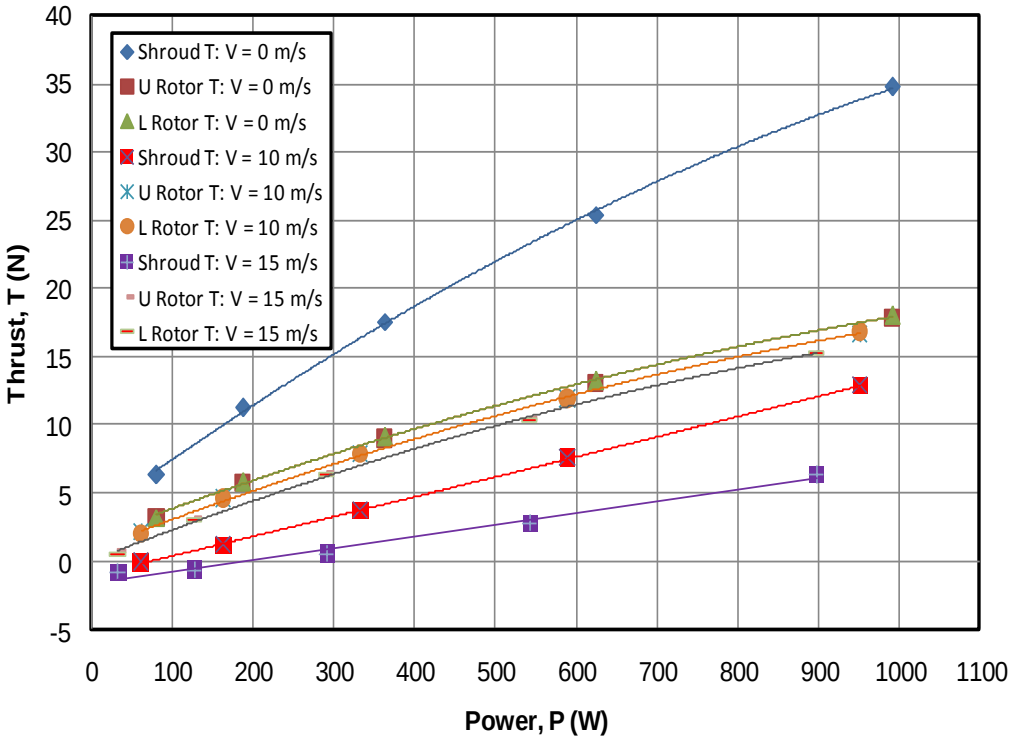

Figure 4.8: Axial flight performance of the shroud, upper rotor and lower rotor of the N241810 CSCRS at S3;P3 and TG1.

As in the case for the hover performance, it can be seen that for the same axial velocity, the thrust produced by the upper and lower rotors is almost identical and decreases with an increase in inflow velocity. The largest reduction in thrust with increased axial velocities can be attributed to the shroud. This reduction of shroud thrust may be due to the fact that the increased axial flow decreased the low pressure region at the inner section of the shroud leading edge due to the forward movement of the stagnation point towards the leading edge of the shroud, which causes less thrust to be developed in this region. A further increase in axial velocity will ultimately result in negative shroud thrust. For the coaxial rotor system used in this study the condition of zero shroud thrust at design rpm is reached when the axial velocity is approximately 28 m/s.

The major impact on the efficiency, in terms of power loading, of the shrouded coaxial rotor system in axial flight conditions is shown in Figure 4.9. The power loading is significantly reduced for an increase in axial velocity.

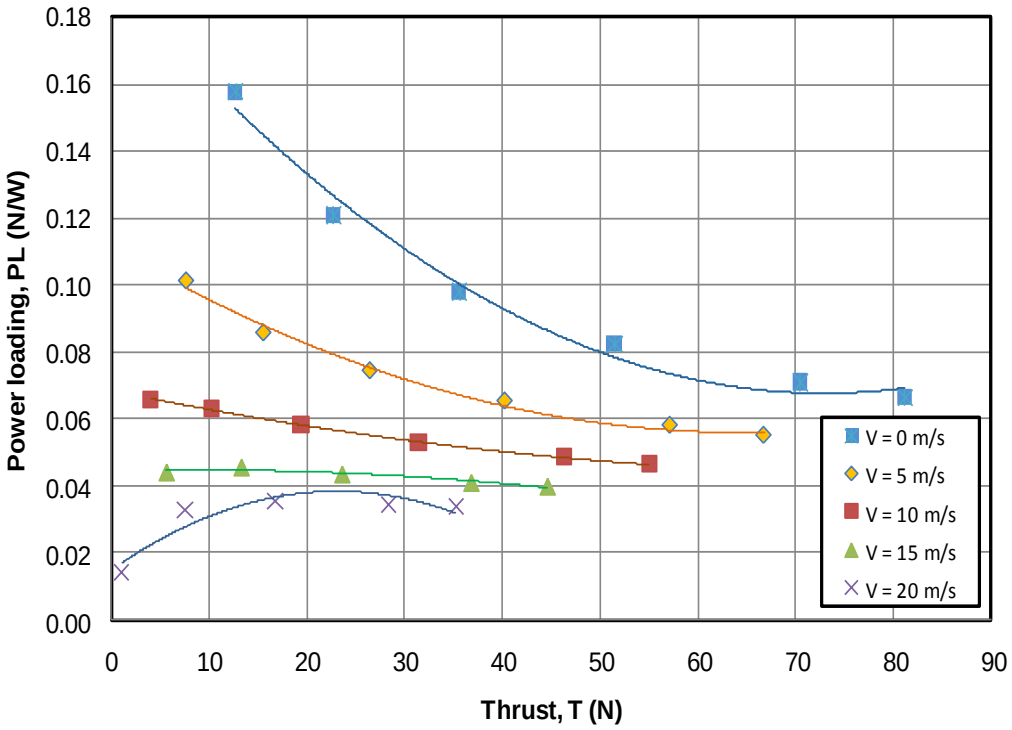

Figure 4.9: Axial flight performance of the N241810 CSCRS in terms of power loading (PL) at various inflow velocities for a S3;P3 spacing and tip gap of 0.01R.

The effect of the rotor tip clearance on the performance of the shrouded coaxial rotor system for the S3;P3 spacing is illustrated in Figure 4.10. An increase in the tip gap reduced the total thrust of the system. From the figure it can be seen that at higher axial velocity the total thrust of the system is less affected by an increased tip clearance.

The total thrust decrease caused by an increase in rotor tip gap and axial velocity is further investigated in Figure 4.11. The load distributions on the shroud and rotors are displayed to examine the influence of various rotor tip gaps and inflow velocities on the shroud and rotors. From Figure 4.11 it follows that the rotor thrust at an axial velocity of 0 m/s or 15 m/s is almost unaffected by the rotor tip gap, but the rotor thrust decreases with an increase in axial velocity.

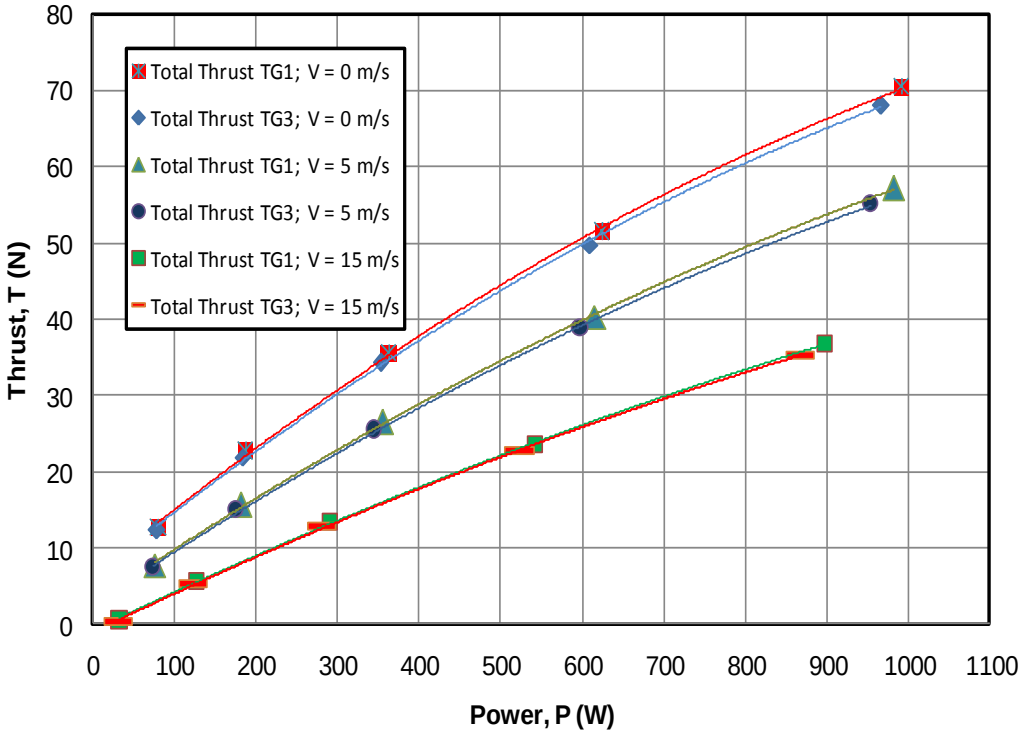

Figure 4.10: Total loads for axial flight performance of the N241810 CSCRS for a S3;P3 rotor spacing at various rotor tip gaps and inflow velocities.

The shroud thrust in hover conditions deteriorates with an increase in rotor tip gap, but at an axial velocity of 15 m/s the shroud thrust is practically unchanged by rotor tip gap changes. The shroud thrust decreases drastically with an increase in axial velocity and is by far the largest contributor to the total thrust reduction caused by an increase in axial velocity and rotor tip gap.

The total efficiency of the shrouded coaxial rotor system is defined as the product of the inflow velocity and the total thrust divided by the total power required by the system. Figure 4.5 indicates that for hover conditions the FM is between 0.81 and 0.86 with the upper value corresponding to the higher thrust conditions. From Figure 4.12 the maximum total efficiency for axial flight conditions is in the order of 0.70 for axial velocities between 15 m/s and 20 m/s in the low thrust region. For the design thrust in the order of 36 N and an axial velocity of 20 m/s, the total efficiency will be approximately 0.68.

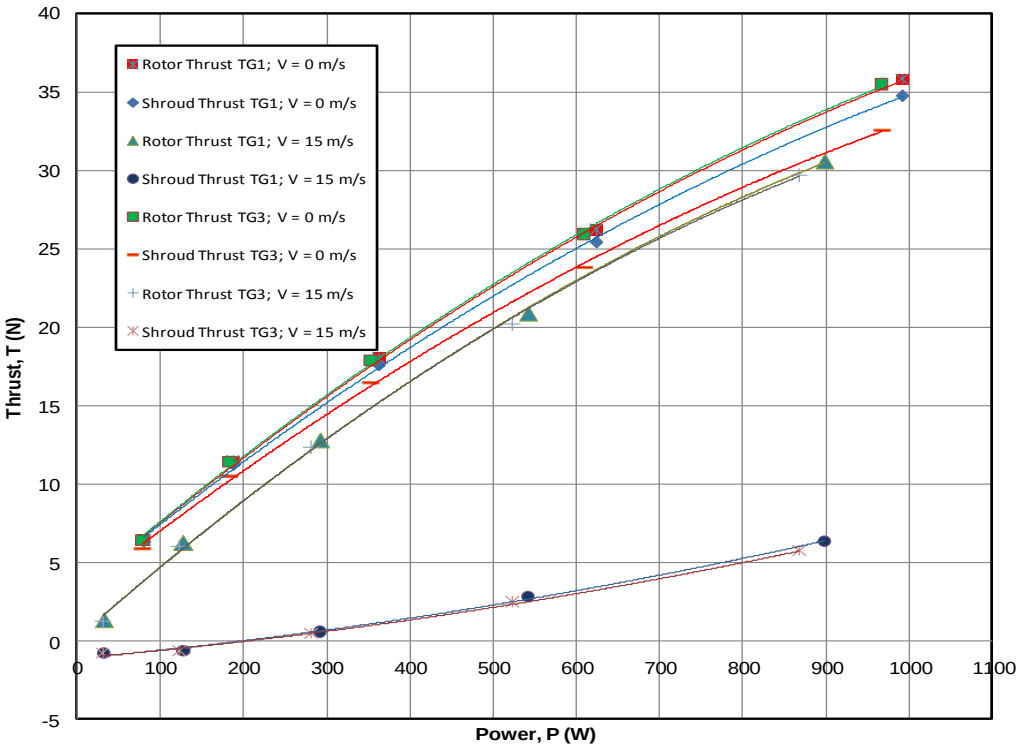

Figure 4.11: Load distributions for axial flight performance of the N241810 CSCRS with a S3;P3 rotor spacing at various rotor tip gaps and inflow velocities.

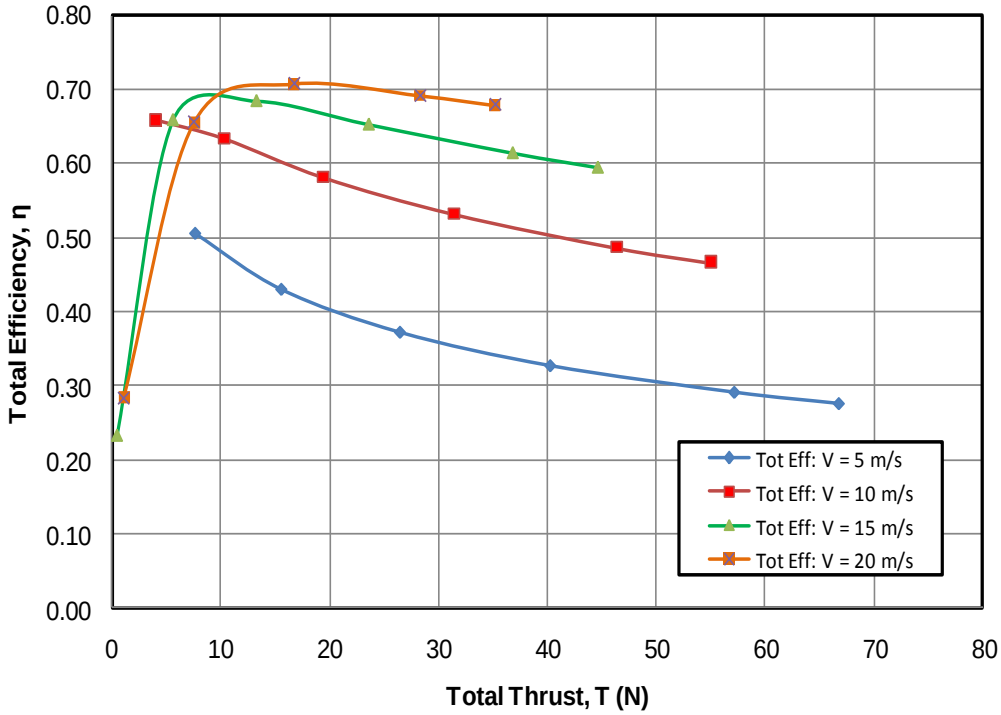

Figure 4.12: Total efficiency of the N241810 CSCRS with a 0.01R tip gap and S3;P3 spacing at various inflow velocities.

CHAPTER 5: CFD FORMULATION

5.1 INTRODUCTION

This chapter gives a brief overview of the CFD formulation for the validation of the performance of the newly designed NACA 2418-14-10 Cambered Shroud Coaxial Rotor System (CSCRS) as predicted in the DFDC code.

The geometry of the shrouded coaxial rotor system (SCRS) was created with the DFDC code after which AutoDesk Inventor 3D CAD was used to import the geometric data into ANSYS TurboGrid and ANSYS Mesher. The performance predictions of the DFDC code were simulated with the general purpose ANSYS-CFX 15.07 code, which is based on the finite volume method (FVM). CFX is capable of simulating the incompressible mean flow field flow past the contra-rotating shrouded rotor system for UAVs.

Predictions for the 35.5 mm diameter shrouded rotors with tip Mach numbers between 0.276 and 0.332 at varying rotor speeds of 5 000 and 6 000 rpm respectively, for which incompressible and isothermal flow conditions can be assumed, were made. A description of the computational method followed is given in the next sections.

5.2 COMPUTATIONAL MODEL

A three dimensional CFD method was used to conduct a steady state analysis on the turbulent and viscous flow field around and inside the shrouded rotors in hover and axial flight conditions. The incompressible mean flow field around the shrouded rotors was simulated using the ANSYS-CFX 15.07 code, which solves the unsteady Reynolds-Averaged Navier Stokes equations by means of an element based FVM (Ansys, 2009). The conservation of mass, momentum and energy equations are solved simultaneously over a predominant hexahedral finite volume mesh.

5.2.1 Discretization of the governing equations

The conservation of mass, momentum and a passive scalar, used in the expression of the energy equation for the temperature distribution, given in scalar coordinates below forms the governing equations for a complete mathematical description of the fluid flow problem. The equation for the temperature distribution was not solved in this study.

$$\frac{\partial \rho}{\partial t} + \frac{\partial}{\partial x_j}\left(\rho U_j\right) = 0 \tag{5.1}$$

$$\frac{\partial}{\partial t}\left(\rho U_j\right) + \frac{\partial}{\partial x_j}\left(\rho U_j U_i\right) = -\frac{\partial P}{\partial x_i} + \frac{\partial}{\partial x_j}\left(\mu_{eff}\left(\frac{\partial U_i}{\partial x_j} + \frac{\partial U_j}{\partial x_i}\right) + S_{U_i}\right) \tag{5.2}$$

$$\frac{\partial}{\partial t}\left(\rho \emptyset\right) + \frac{\partial}{\partial x_j}\left(\rho U_j \emptyset\right) = \frac{\partial}{\partial x_j}\left(\Gamma_{eff}\left(\frac{\partial \emptyset}{\partial x_j}\right) + S_{\emptyset}\right) \tag{5.3}$$

Equations 5.1, 5.2 and 5.3 are integrated over the control volume and the Gauss' Divergence Theorem is used to convert the volume integrals involving divergence

and gradient operators to the surface integrals which results in the following set of equations:

$$\frac{\partial}{\partial t}\int_V \rho dV + \int_S \rho U_j \, dn_j = 0 \tag{5.4}$$

$$\frac{\partial}{\partial t}\int_V \rho U_j \, dV + \int_S P U_j U_i \, dn_j = \int_S P \, dn_j + \int_S \mu_{eff}\left(\frac{\partial U_i}{\partial x_j} + \frac{\partial U_j}{\partial x_i}\right) dn_j + \int_V S_{U_i} \, dV \tag{5.5}$$

$$\frac{\partial}{\partial t}\int_V \rho \emptyset dV + \int_S \rho U_j \emptyset \, dn_j = \int_S \Gamma_{eff}\left(\frac{\partial \emptyset}{\partial x_j}\right) dn_j + \int_V S_\emptyset \, dV \tag{5.6}$$

where S and V in Equations 5.4, 5.5 and 5.6 respectively indicate the surface and volume region integrals and dn_j are the Cartesian components of the outward normal surface vectors.

5.2.2 Rotational forces

To account for the effects of Coriolis and centrifugal forces when simulating flow in a rotating frame of reference which rotates at a constant rotational velocity Ω, additional sources of momentum are required (Ansys, 2009). In Equation 5.2 and 5.3 the source terms are modified as:

$$S_{M,rot} = S_{Cor} + S_{cfg} = -2\,\rho\Omega \text{ x } U - \rho\Omega \text{ x } (\Omega \text{ x } r) \tag{5.7}$$

where U is the relative frame velocity and r is the location vector.

5.2.3 Turbulence model

To model the turbulent flow in this study, the k-epsilon and k-omega turbulent models were initially used, but these models struggled to converge. The k-ω based shear-stress transport (SST) turbulence model was used in this study. This low Re turbulence model was designed to give an accurate prediction of the start and the amount of fluid flow separation due to adverse pressure gradients. This is done by the incorporation of transport effects into the expression of the eddy viscosity, resulting in a high accuracy boundary layer simulations turbulence model. Included in the SST turbulence model used in CFX are blending functions in the near wall region that are dependent on the wall distance (Ansys, 2009). The model automatically resorts to a wall function formulation called the “automatic wall treatment” in the vicinity of coarse grid resolutions close to a wall. An additional equation is solved automatically by the CFX-Solver at the beginning of the simulations to calculate the wall distance. With all turbo machinery there is a large component of primary and induced swirl in the flow-field. ANSYS CFX provides a curvature correction option when the SST turbulence model is selected to capture the additional turbulent kinetic energy produced from the swirl (Ansys, 2009). CFX has several transitional turbulence models as extensions to the standard SST Turbulence model. The writer experimented with the Gamma Theta and other models, but found similar results as with the standard SST model.

5.3 COMPUTATIONAL DOMAIN

The computational domain for the simulation of the shrouded contra-rotating rotors in hover and axial flight is divided into two stationary half cylindrical regions and two rotating regions. Due to the axisymmetric nature of the problem, only one half of the model is analysed to save on computational time. The dimensions of the computational domain selected were similar to the domain used by Akturk *et al.* (2009) in their computational study of a 5 inch ducted fan for V/STOL UAV applications. The outer half cylindrical region extends 8 D_R ahead and 12 D_R behind the model, while an extension of 5 D_R to each side was allowed.

In this study the multi reference frame (MRF) method was used to simulate the flow activities in the stationary domains and the rotating rotor domains. The outer computational domain (named Volume) hosts a smaller inner domain (named Blades) in which the shrouded contra-rotating rotors are situated as shown in Figure 5.1.

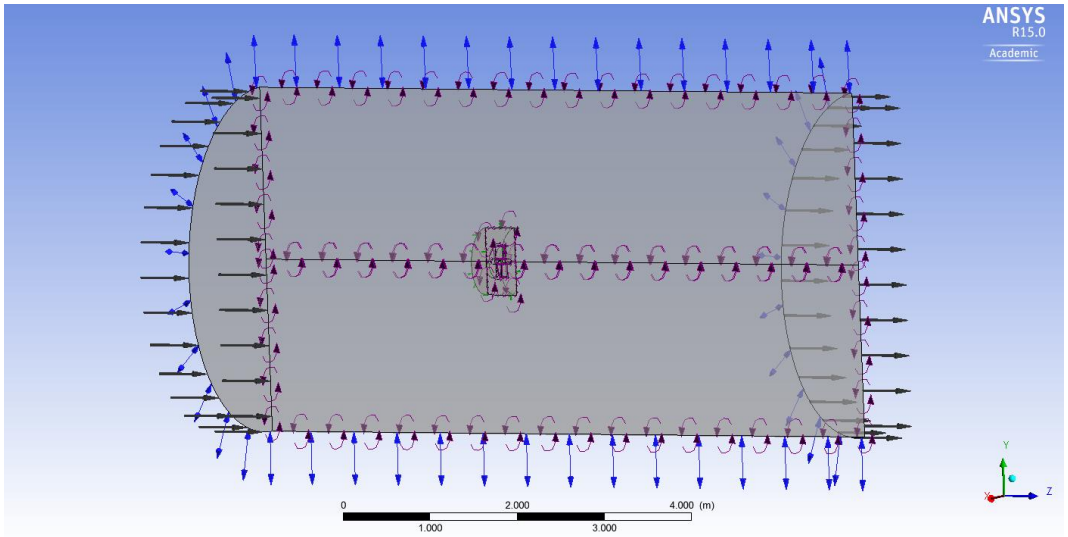

Figure 5.1: MRF Transparent with periodic interfaces and boundary conditions.

In the rotating rotor domains, named R1 and R2, the alternate rotation model was selected, resulting in the solver to solve the advection term in the stationary frame and transform it back to the rotating frame. The alternate rotation model can reduce the production of false swirl due to fluid motion that is not well aligned with the rotating frame as is the case with the flow through a rotor, which is primarily axial and not well aligned with the rotating frame (Ansys 2009). A stage type interface model was inserted between the stationary and rotating frames as well as between the two rotating rotor frames. This interface model circumferentially averages the fluxes on the interface and sends the average fluxes to the downstream section. A general grid interface (GGI) was used to connect the meshes on either side of the two joined boundary surfaces where they did not match. Periodic interfaces were created on the symmetry planes to reduce the size of the computational domain and computation time as indicated in Figure 5.1.

5.4 BOUNDARY CONDITIONS

For the computation, an undisturbed subsonic velocity in the axial direction is specified for an inlet boundary condition and atmospheric static pressure is prescribed on the outlet surface. On the outer side wall of the cylinder, a free-slip-wall boundary condition is prescribed, which ensures that the flow is not decelerated when it approaches the surface. The smaller inner flow domain hosts the rotating domains as well as all the external sections of the shroud and hub not included in the rotating domains. All sections of the rotor hub, the shroud and blades are considered as smooth solid walls with no-slip boundary conditions. The shroud walls inside the rotating domains are prescribed by a counter rotating wall boundary condition, since the counter rotating wall in the rotating system will ensure a stationary wall in the global system. The boundary conditions are shown in Table 5.1.

Table 5.1 Boundary conditions imposed.

Boundary type	Property	Value
Inlet: (hover flight)	Flow regime Mass & momentum Static pressure Turbulence intensity	Subsonic Relative press = 0 Pa Low = 1%
Inlet: (axial flight)	Flow regime Mass & momentum Cylindrical velocity Turbulence intensity	Subsonic Axial comp.= 5-10 m/s Radial comp.= 0 m/s Theta comp.= 0 m/s Low = 1%
Outlet:	Flow regime Mass & momentum Static pressure Turbulence intensity	Subsonic Relative press = 0 Pa Low = 1%
Outer side walls (hover flight) Opening boundary:	 Flow regime Mass & momentum Flow direction Turbulence intensity	 Subsonic Opening pressure & direction Normal to boundary Medium = 5%
Outer side walls (axial flight) Wall boundary:	 Flow regime Mass & momentum	 Subsonic Free slip wall

5.5 COMPUTATIONAL MESH

The outer domain is predominantly filled with hexahedral elements with a smaller number of pyramids and tetrahedral elements as indicated in Figure 5.2. The unstructured mesh in the smaller inner domain hosts the shrouded rotor system, and consists of tetrahedral and wedge elements as shown in Figure 5.3.

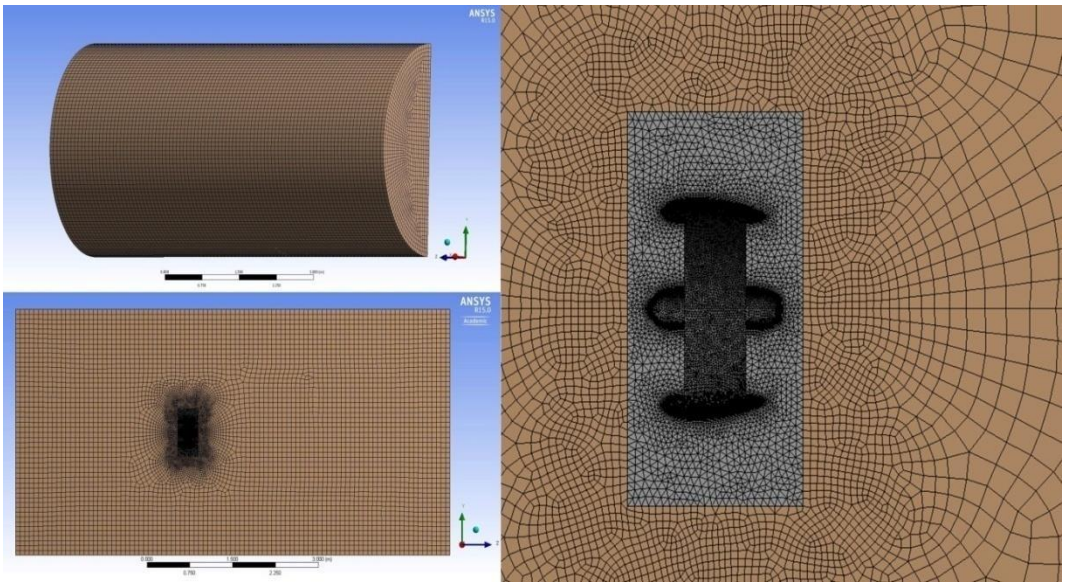

Figure 5.2: The computational mesh.

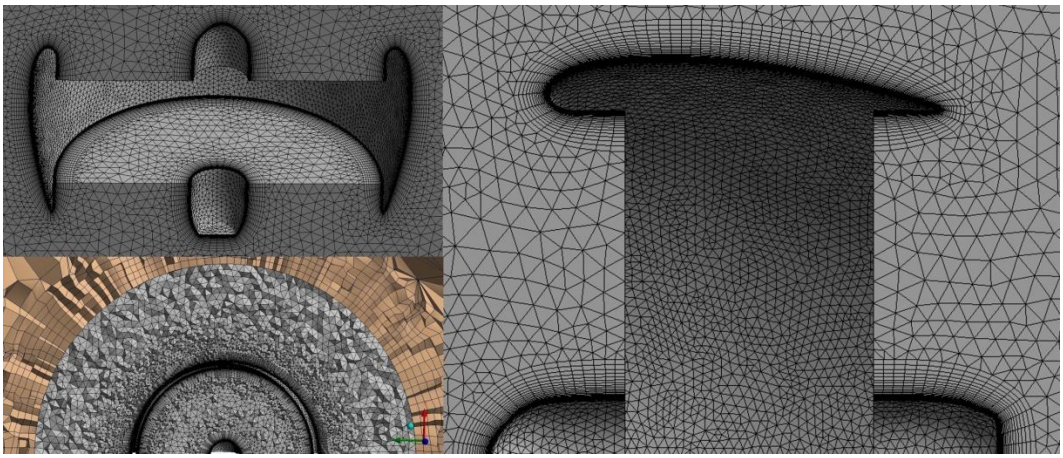

Figure 5.3: The inner computational mesh with hexahedral elements and inflation.

5.6 BOUNDARY LAYER INFLATION

A boundary layer inflation of at least 10 layers is needed, but 20 layers are desirable to fully benefit from this model. To ensure that the laminar sub-layer in low Re flows is thoroughly captured the average Y-plus value should be in the order of 1 (Ansys 2009). A boundary layer inflation of 30 layers with a first layer height set at 5.e-5 m and an expansion ratio of 1.15 was used in the smaller fluid domain and in the rotating fluid domains of this study to fully benefit from this turbulence model. Edge sizing was used on the trailing edge of the shroud with a curvature normal angle set at 5°.

5.7 GRID GENERATION IN THE ROTATING FLUID DOMAINS

The ANSYS TurboGrid package was used to create good quality structured grids for the two rotating domains. The “Tradional with Control Point” placement in conjunction with the H-Grid method and O-Grid inclusion with control points was selected. TurboGrid generates hexahedral meshes which are ideal for solving the complex blade passage problems for rotating machinery. Figure 5.4 illustrates the grid on the hub and blade. The two rotating domains consist of a total number of 4 468 236 elements.

In this study Y-plus values in the order of 1 were used on the blades. Y-plus values in the order of 5 for the hub regions were the lowest that TurboGrid would allow before negative volume elements were encountered in the mesh.

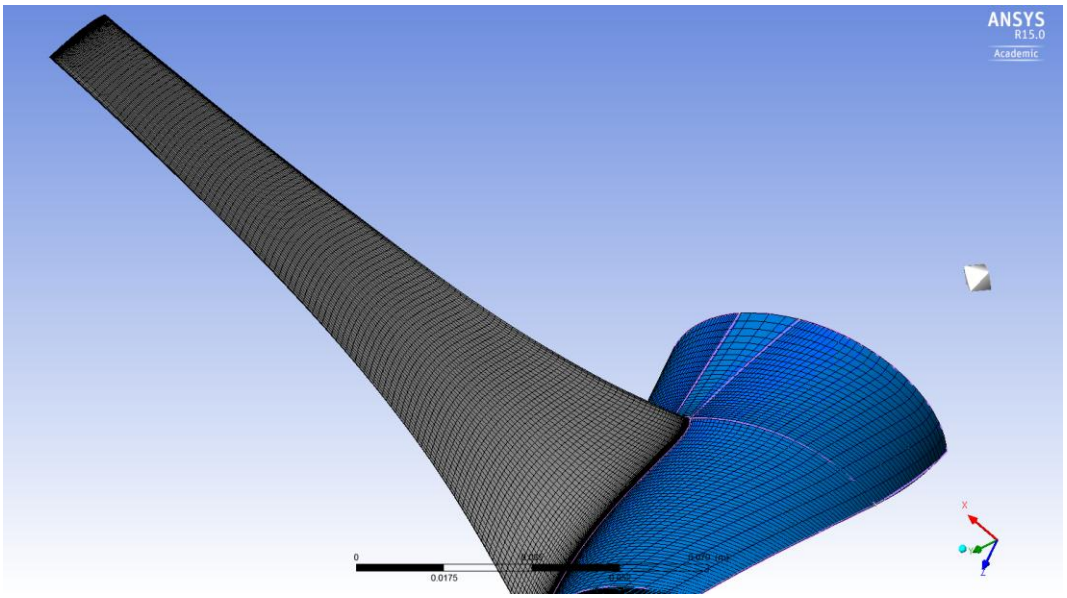

Figure 5.4: The TurboGrid-generated hexahedral meshes on the hub and blade.

5.8 CONVERGENCE

Convergence of the steady state problem was assumed after the solution satisfied at least two of the following three criteria:

- Residual RMS Error values for P-Mass, U-Mom, V-Mom and W-Mom have reduced to a value less than 10^{-4}. This criteria could not always be reached, with the V-Momentum residual mostly having the highest value.
- Monitor points set up for the thrust and torque of both rotors having reached a steady solution for at least the last 50 consecutive iterations.
- The flow domain has P-Mass, U-Mom, V-Mom and W-Mom imbalances of less than 1%.

For steady-state problems, the CFX-Solver uses a false time scale to under-relax the equations as they iterate towards a solution. Auto Time Scale uses a physical time scale, dependent on the flow conditions, boundary conditions, flow physics, and flow domain geometry. It is usually stable, but faster convergence for steady-state problems is often possible by selecting a larger time scale using the local time scale factor (Ansys 2009). A factor of 5 was used as a first guess. Large time scales normally result in fluctuating convergence or no convergence. Time scales that are too small result in very slow, steady convergence.

In this study the use of local time scale factors between 1 and 10 were utilized to improve the convergence rate although the last few iterations were done using the auto time scale setting. The value entered is a multiplier of a local element-based time scale, which is roughly the time required by an element to travel through the flow domain, $t \approx \frac{lenght\ of\ domain}{mean\ velocity}$. The default time scale factor is 5 and values less than this are considered as "small" time steps. The simulations typically required between 350 and 500 outer loop iterations to achieve convergence.

5.9 MESH INDEPENDENCE

With the convergence criteria above met, the mesh independence was confirmed using 6 different mesh refinements. A simulation, at a rotation speed of 5 000 rpm and an axial velocity of 5 m/s, was performed for each of the refined meshes until convergence was reached after which the total thrust produced by the rotor system for the respective meshes were compared as indicated in Figure 5.5. From Table 5.2 it is evident that extremely fine meshes in the rotational domains are required to ensure mesh independence. The mesh with 5 648 084 elements is considered to be independent of the mesh resolution, and was used for the remainder of the analysis.

Table 5.2 Mesh independent study.

Domain	Mesh 1	Mesh 2	Mesh 3	Mesh 4	Mesh 5	Mesh 6
Blades	273863	273863	971832	971832	972048	972048
R 1	262032	479568	1104288	1104288	2225376	2675768
R 2	227016	485516	1126140	1126140	2242860	2327868
Vol	94879	94879	207764	354153	207764	207764
Total	857790	1333826	3410024	3556413	5648048	6183448
Thrust (N)	26.24	26.15	22.82	22.76	21.5	21.2

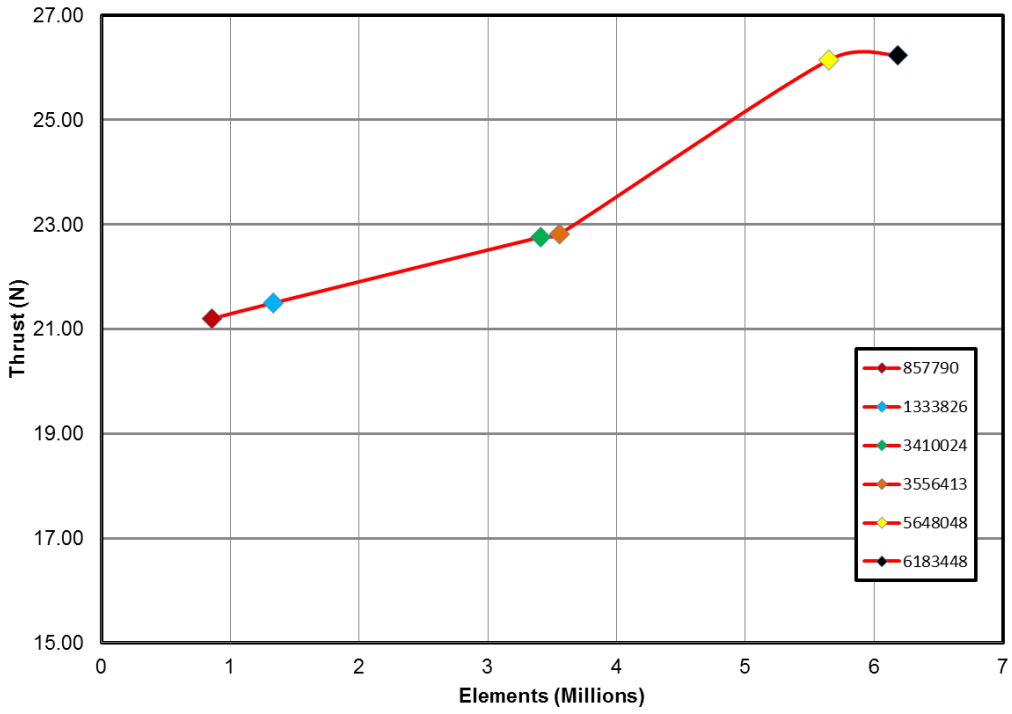

Figure 5.5: The mesh independence study.

The meshing statistics of Mesh 2 that was used for the remainder of the study are given in Table 5.3.

Table 5.3 Meshing statistics.

Domain	Nodes	Elements	Tetrahedra	Wedges	Hexahedra
Blades	336113	972048	493158	478890	0
R1	2289916	2225376	0	0	2225376
R2	2307884	2242860	0	0	2242860
Volume	183078	207764	17799	3515	158028
All Domains	5116991	5648048	510957	482405	4626264

Figure 5.6 displays a contour plot of the axial velocity on the symmetry-plane and at the outlet for hover flight at a rotational speed of 5 000 rpm. The plot is generated from the CFX simulation using Mesh 5. The symmetric distribution of the velocity in the slipstream is a clear indication of a converged solution with a sufficiently fine mesh.

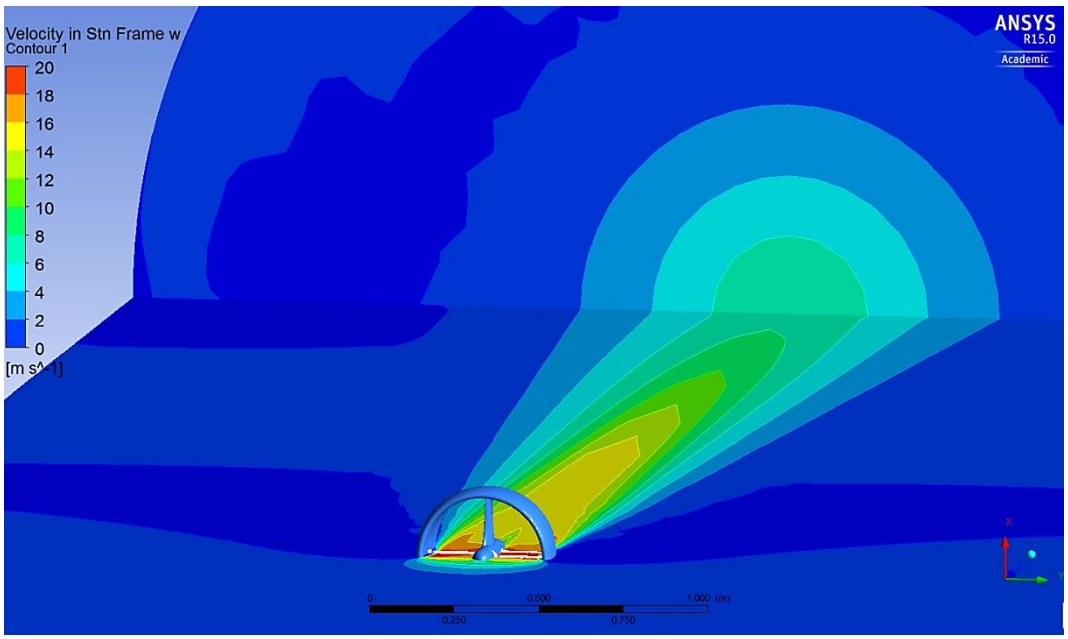

Figure 5.6: A velocity contour plot of a mesh independent CFD solution.

CHAPTER 6: CFD PERFORMANCE PREDICTIONS OF THE CSCRS

6.1 INTRODUCTION

This chapter presents the ANSYS-CFX CFD performance predictions of the design. The CFD hover and axial flight performance of the newly designed rotors are compared to the DFDC results for the NACA2418-14-10 CSCRS. Only the S3 rotor-to-rotor spacing and the P3 rotor-to-shroud position were considered in this comparison. The CFD simulations were performed at rotation speeds of 4 000 rpm, 5 000 rpm and 6 000 rpm. In all these simulations the nominal rotor tip gap was set at 0.01R.

6.2 CFD PERFORMANCE PREDICTIONS FOR THE CSCRS IN HOVER

Figure 6.1 compares the hover thrust of the Lee rotors to the DFDC and the CFD simulation at various power inputs. The fact that the thrust delivered by the DFDC rotors exceeds the performance of the rotors used by Lee over the entire power range is also confirmed by the CFD predictions. Although the CFD predictions are less optimistic than the DFDC results they still indicate a 33% increase in thrust for the design power input of 370 W at a rotational speed of 5 000 rpm.

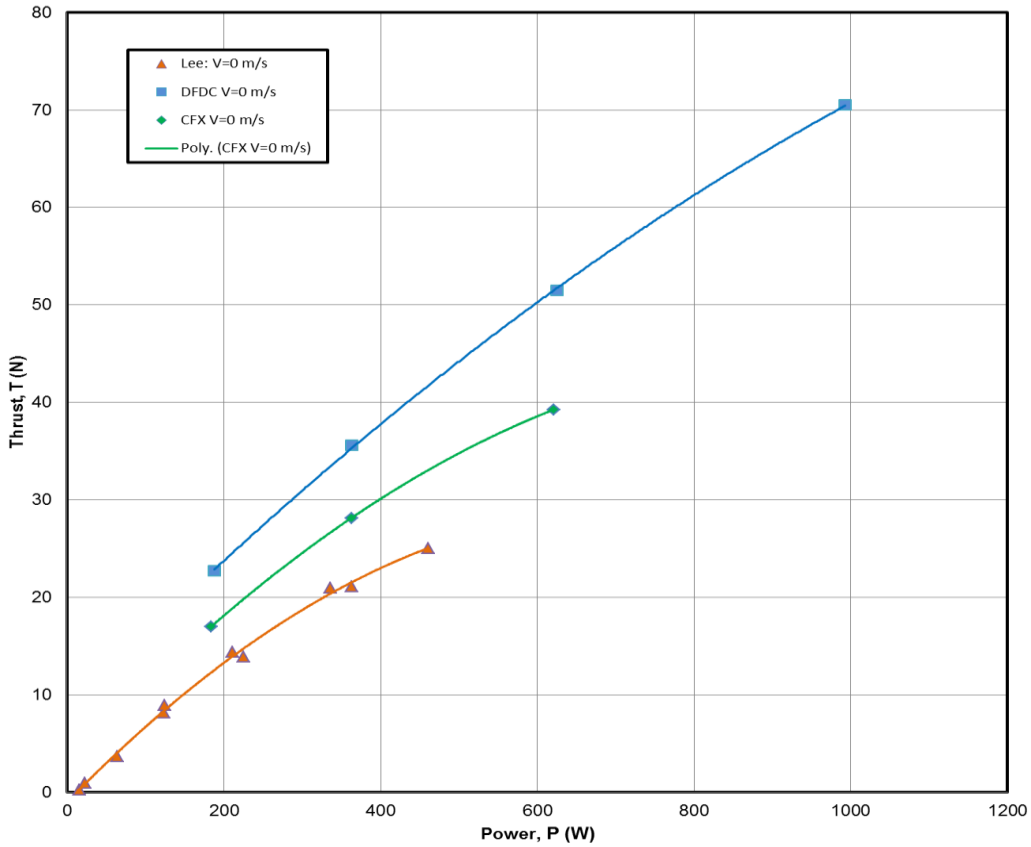

Figure 6.1: A comparison between the hover performance of the Lee CSCRS experimental data, the DFDC results and the ANSYS-CFX CFD predictions at various power inputs.

Figure 6.2 illustrates the comparison between the DFDC and CFX thrust predictions for the design in hover flight at various rotational speeds. The CFD simulation predicts a lower thrust in hover condition at a specified rotational speed, with the difference increasing at higher rotational speeds.

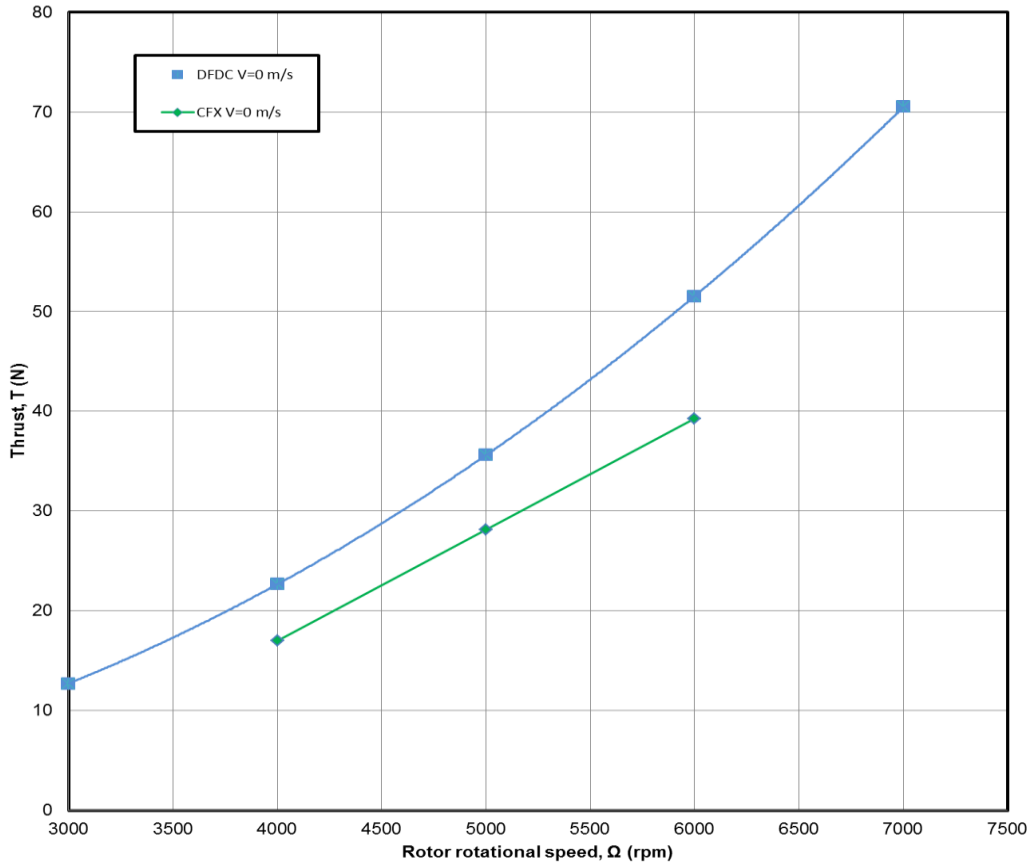

Figure 6.2: A comparison between the DFDC and CFX thrust predictions for the design in hover flight.

The load distribution between the shroud and the rotors is presented in Figure 6.3. According to the CFD thrust prediction at the same rotational speed, less thrust is generated by the upper rotor, while more thrust is generated by the lower rotor than the DFDC results indicate.

The CFD prediction that the lower rotor will perform better than the upper rotor might be due to the fact that the lower rotor is operating in the rotating flow coming from the upper rotor at a more favourable incidence and that the lower rotor is able to extract some of the rotational energy present in the slipstream of the upper rotor. The total thrust generated by the two shrouded rotors correlates well in the CFD and DFDC predictions.

The CFD predicted shroud thrust in hover flight is close to the average of the thrust predicted for the upper and lower rotors. It is in the order of half the amount of thrust predicted by DFDC. From Equation 6, derived for a single rotor, the thrust ratio between the shroud and the rotor is given as $T_{Shroud}/T_{Rotor} = (2\sigma_d - 1)$, where $\sigma_d = \frac{A_e}{A}$ is the shroud diffuser ratio. Since the current shroud has a straight diffuser meaning $\sigma_d = 1$, the rotor and shroud inlet should share about 50% of the total thrust. If it is assumed that the mass flow rate through the shrouded coaxial rotors are approximately the same as through the single shrouded rotor, the resulting external flow over the leading edge of the shroud will be the same, irrespective of one or two rotors in the shroud. This would imply that the shroud

thrust should be of the same order as the average thrust of the coaxial rotors. The more conservative shroud thrust prediction of the CFX analysis thus seems to be the realistic one.

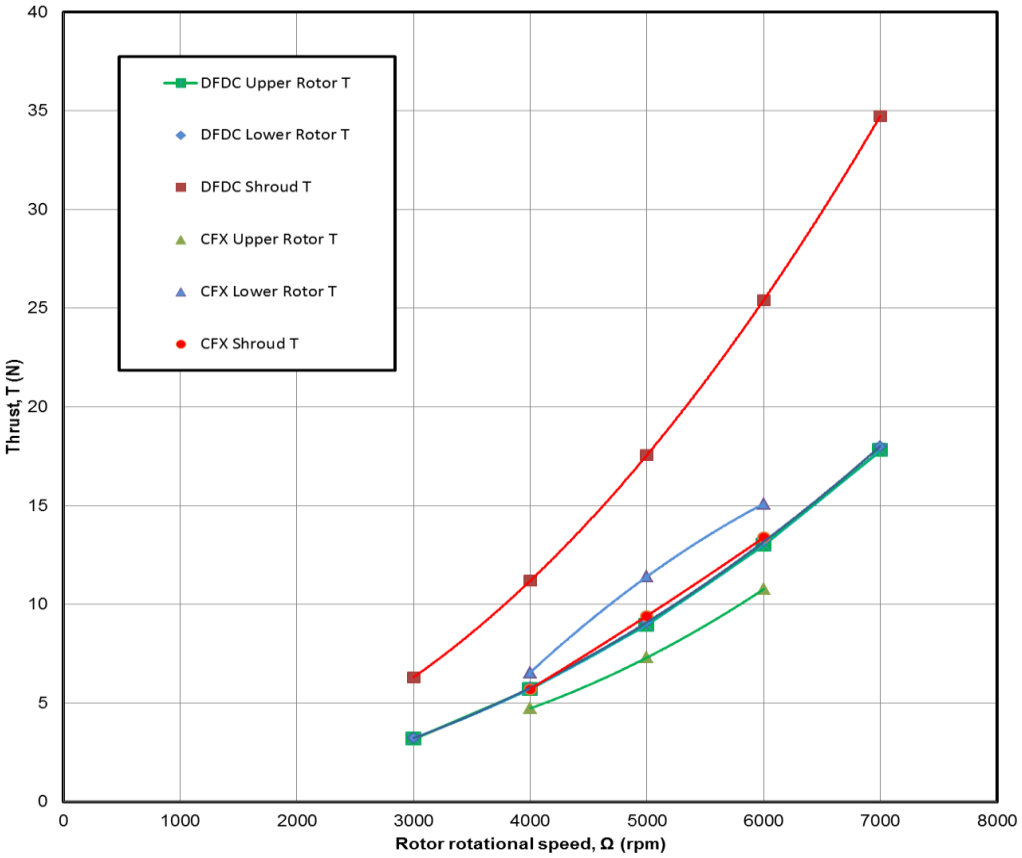

Figure 6.3: A comparison between the DFDC and CFX load distribution predictions in hover flight for various rotational speeds.

The difference in the shroud thrust predictions may be due to the very basic boundary layer analysis on the shroud and hub in DFDC. It is currently done at the end of the blade design, in one pass, based on the calculated pressures. An interactive routine where the boundary layer thickness will result in pressure changes should be incorporated into the DFDC code. This might have a significant influence on the shroud thrust predictions.

Figure 6.4 represents a comparison between the DFDC and CFX torque predictions on the upper and lower rotors in hover flight of the shrouded coaxial rotor system. The CFD predicted torque on both the rotors correlates well with the DFDC prediction. CFX predicts a slightly higher torque for the upper rotor and a slightly lower torque for the lower. The CFD simulation thus predicts a resultant positive torque. Whilst DFDC predicts a total torque of 0.00316 Nm at 5 000 rpm, the CFD prediction is of 0.0537 Nm at 5 000 rpm.

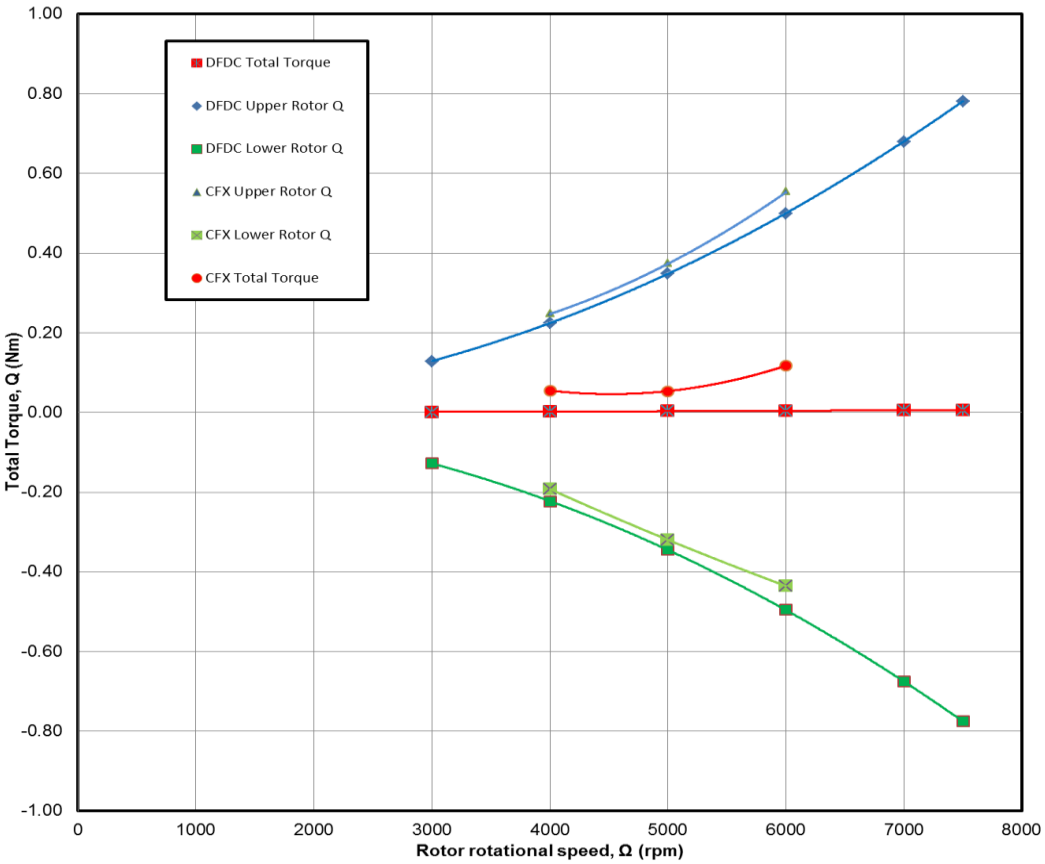

Figure 6.4: A comparison between the DFDC and CFX torque predictions on the upper and lower rotors in hover flight.

Comparing Figure 6.1 with Figures 6.2 to 6.4 leads to the conclusion that although DFDC predicts a higher thrust in hover flight than CFX at a given power input and rotational speed, these two methods correlate well, except for the shroud thrust that seems to be over predicted by DFDC.

The power loading (PL) is the direct ratio of thrust developed to the power required by the system and is an indication of the efficiency of the system. Figure 6.5 compares the power loadings of the rotors from the Lee experimental data to the DFDC and CFD predictions. It can be seen that DFDC and CFD predictions correspond with the trends discussed above and that considerably less power is required by the newly designed rotors to produce the same amount of thrust than the original design.

6.3 CFD PERFORMANCE PREDICTIONS FOR THE CSCRS IN AXIAL FLIGHT

The axial flight performance of the shrouded rotor system was evaluated to assess the effect of various inflow velocities on the performance. For a fixed pitch rotor configuration an axial flow through the rotor increases the inflow angle which in turn will decrease the angle of attack of the blade section, resulting in a decrease of thrust. A lower thrust will decrease the rotor torque and the power required to turn the rotor.

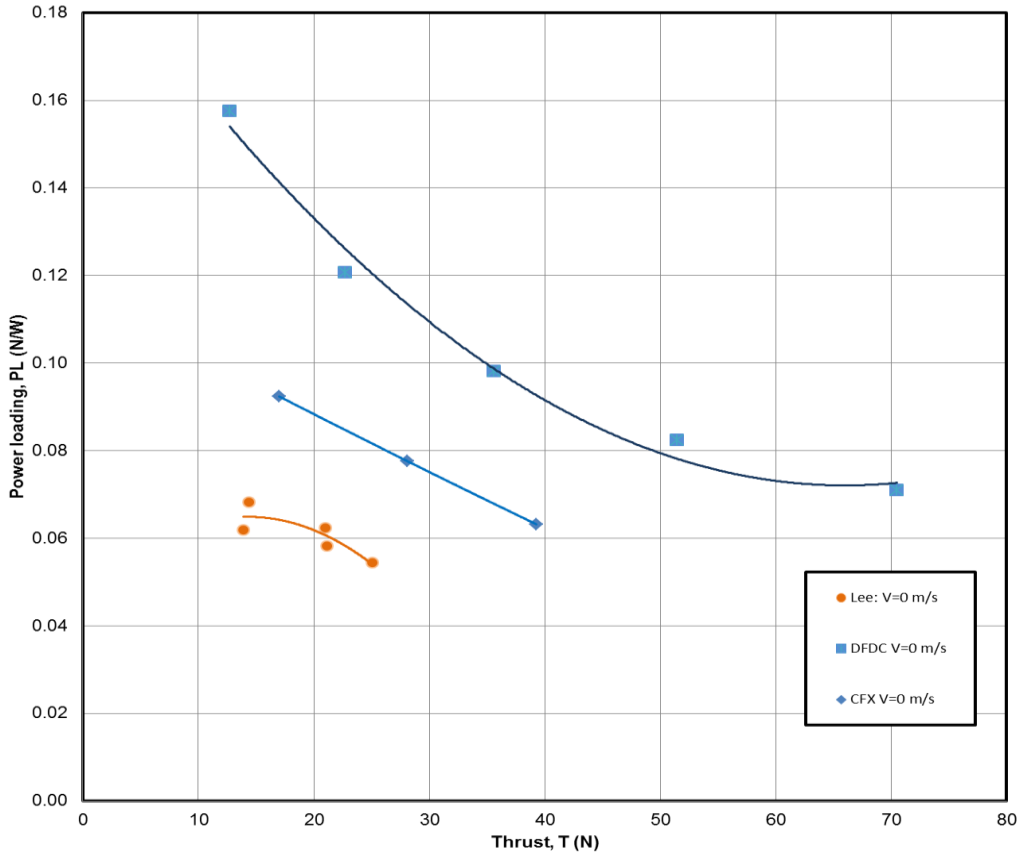

Figure 6.5: A comparison between the Lee data, DFDC and CFX power loading with thrust in hover flight.

Figure 6.6 represents the total loads (shroud and rotors) for the axial flight performance of the shrouded coaxial rotor system at various inflow velocities and rotor positions at different power inputs. For both the DFDC and the CFD predictions the figure clearly illustrates that for a given power input the total thrust delivered by the system decreases with increasing axial velocity.

The CFD and DFDC thrust predictions for axial flight agree closely for the velocities simulated in this study. The graphs for hover flight were included in this figure to highlight the decreasing effect of shroud thrust with increasing axial velocity.

Figure 6.7 illustrates the impact of an increased axial velocity on the efficiency, in terms of power loading. For both the CFD and DFDC predictions the power loading is significantly reduced by an increase in axial velocity. The decreasing effect of the shroud thrust with increasing axial velocity can be seen by comparing the power loading predictions at higher axial velocities.

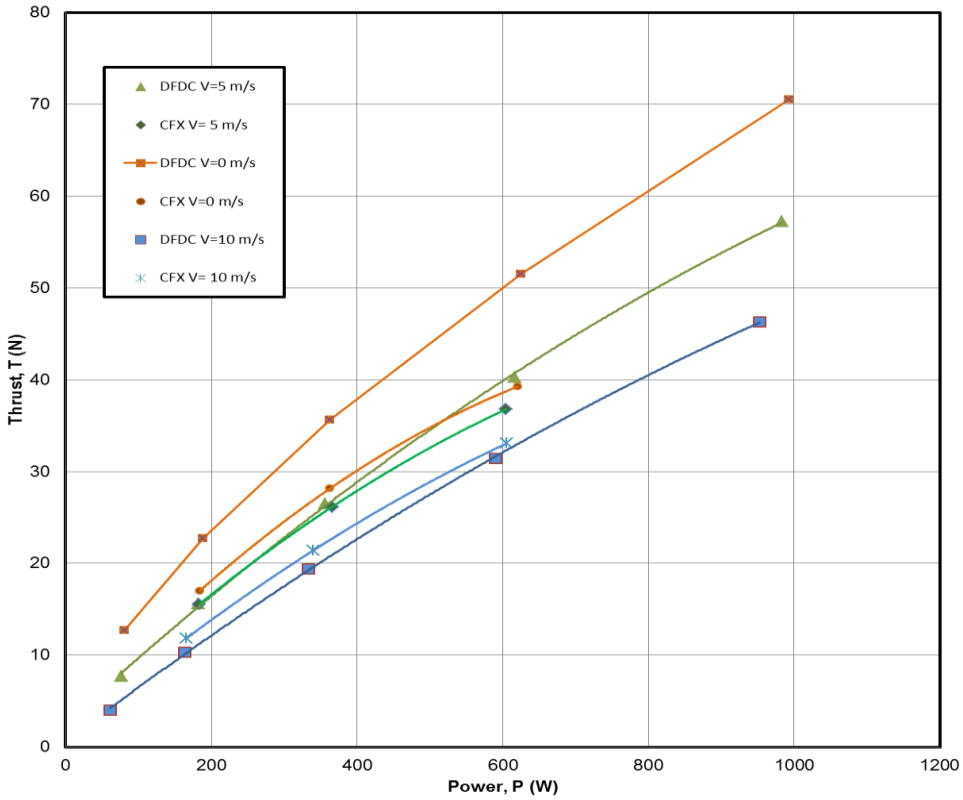

Figure 6.6: A comparison between the DFDC and CFX total load predictions at various axial velocities.

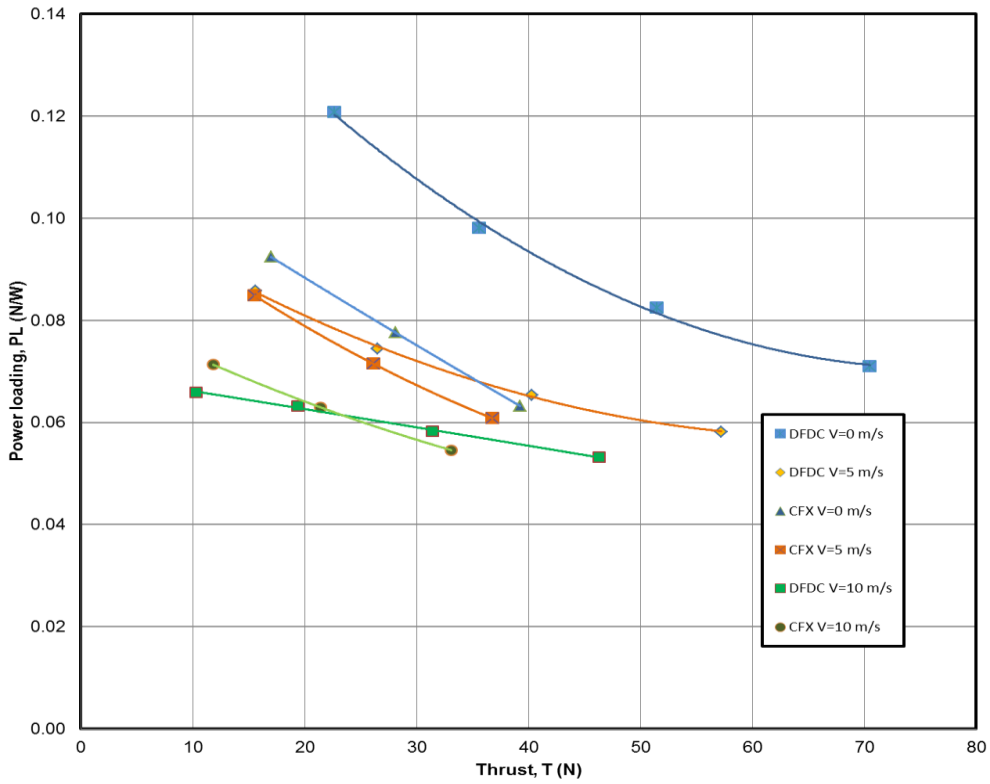

Figure 6.7: A comparison between the DFDC and CFX power loadings at various axial velocities.

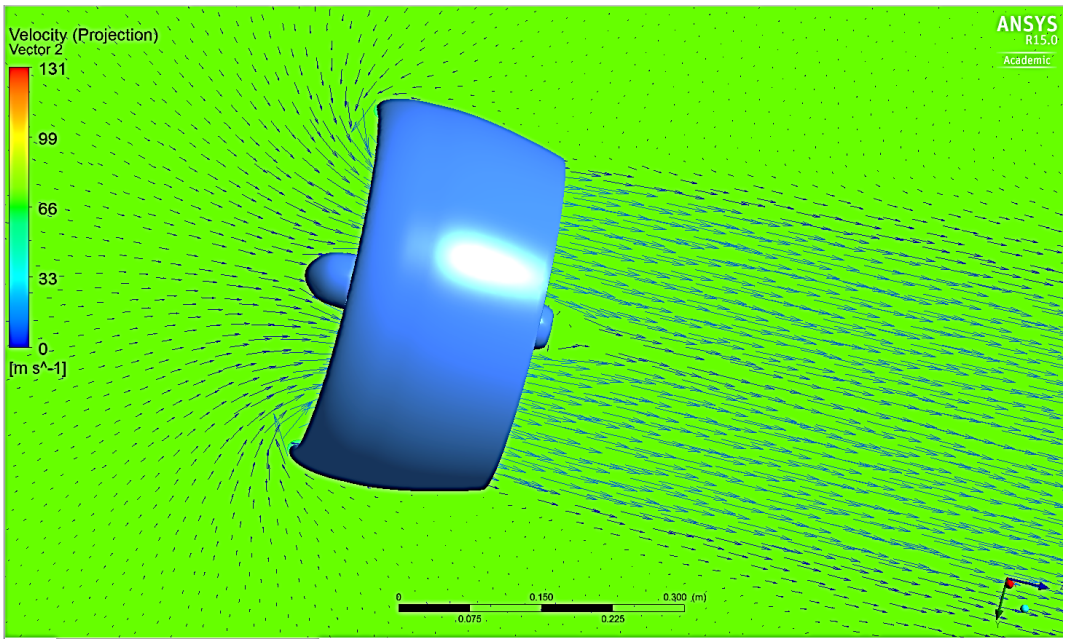

Figure 6.8: A CFX velocity vector plot for hover flight at a rotational speed of 5 000 rpm.

A CFX velocity vector plot for hover flight at a rotational speed of 5 000 rpm is illustrated in Figure 6.8. The direction, magnitude and symmetry of the flow correlates with the pressure contour plot of the same flight condition as illustrated in Figure 6.9.

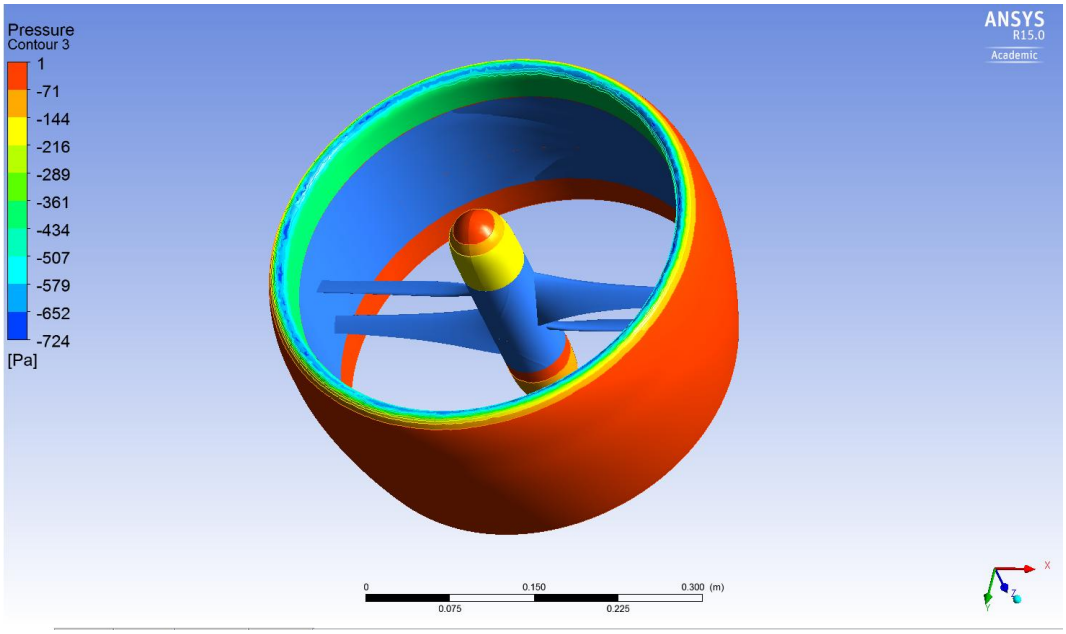

Figure 6.9: A CFX pressure contour plot for hover at a rotational speed of 5 000 rpm.

The velocity vector plot clearly indicates how the flow is being accelerated and sucked into the shroud due to the action of the rotating rotors that cause a low pressure region above the rotor plane. This explains the low pressure distribution on the inside of the shroud's leading edge which results in additional thrust or lift.

CHAPTER 7: CONCLUSION

7.1 INTRODUCTION

The aerodynamic design of a counter rotating rotor system for a UAV was completed. The challenge was to design a more efficient coaxial rotor for the ducted coaxial rotor system as published by Lee (2010). The new design was performed using the DFDC code and compared with the experimental data of the existing design. The new design was also compared to ANSYS-CFX CFD simulation results which validated the DFDC code predictions. The study only considered the aerodynamic design of the counter rotating rotor system for the existing shroud. The final counter rotating rotors are displayed in Figure 7.1.

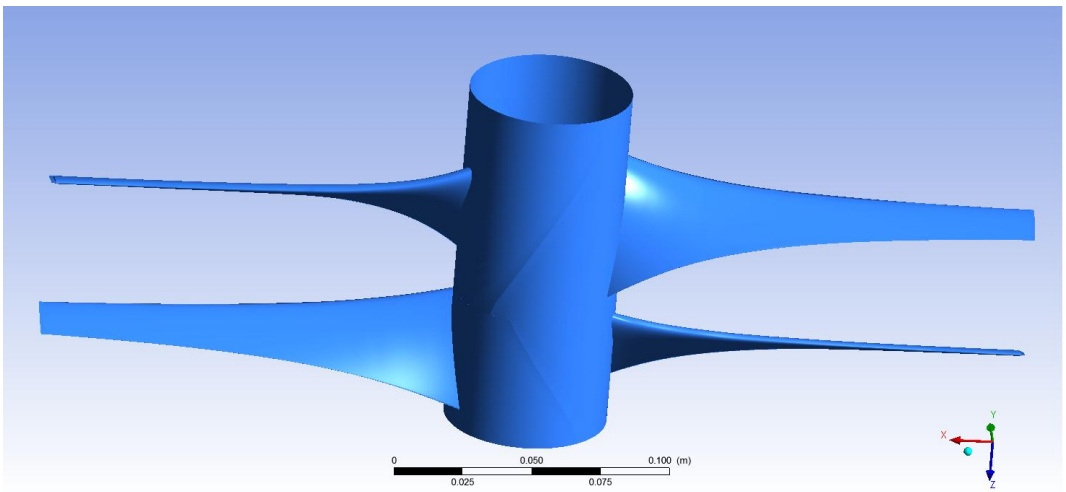

Figure 7.1: The three-dimensional model of the counter rotating rotor system.

The literature review considered the current trends of UAV design. Specific focus was placed on the design of shrouded or ducted rotor UAVs. The research revealed that a number of studies have been done on the design of the shroud, the axial position of the rotor in the shroud and the spacing between the two counter rotating rotors. The design of the leading edge lip of the shroud, the length of the shroud, as well as the tip-gap effect was also investigated.

Research indicated that the design of high-performance simple fixed-pitch rotors with optimum low Re number airfoils for small scale UAVs is a trade-off between optimal aerodynamic performance and ease of manufacturing. The ideal profile would be very thin and highly cambered with a sharpened leading edge, but in reality these airfoils are difficult to manufacture.

Although research on the design of a UAV helicopter rotor blade with variable pitch has been conducted, very little research on the aerodynamic design of a shrouded counter rotating fixed pitch rotor system could be found.

Lee (2010) published experimental data on a shrouded coaxial rotor system, but did not design the rotors and suggested that further work should be done on this aspect.

7.2 AERODYNAMIC DESIGN OF THE COAXIAL ROTOR SYSTEM

Based on the research and resources available it was decided to use Mark Drela's freeware code, named DFDC, to design a more efficient, simple fixed-pitch counter rotating rotor system for the shroud used by Lee. The design was based on two conditions:

- To design the rotors to deliver the maximum thrust with an input power of 370 W at a design rotor speed of 5 000 rpm.
- To achieve a torque balance for the coaxial rotors with each rotor operating at the same rotational speed, ranging from 3 000 to 7 500 rpm.

The design strategy was to obtain published experimental data of a shrouded contra-rotating rotor system in hover and forward flight in terms of thrust, torque and power to be used as a benchmark for the new design. The present work is based on the Aero Flight Dynamics Directorate (AFDD) ducted coaxial rotor system and experimental data as published by Lee (2010). The next phase was to select the radial airfoil profiles and numerically analyse them using XFOIL and XFLR 5 to ensure that they would deliver a high L/D ratio over a wide range of angles of attack within the expected Re number range. The selected airfoil characteristics were then used in the DFDC-070ES2a code for the blade design and optimization, after which the design was benchmarked against published experimental data and finally verified in ANSYS-CFX 15.07.

7.2.1 Selection and numerical analysis of the best suited airfoils

The goal of the blade design is to ensure maximum thrust at steady state for a given power supplied to the rotor shaft. This means that the blade AoA and Re should be optimal for the airfoil to ensure a high lift to drag (L/D) ratio.

The Re range for most small scale UAV rotor blades is in the order of 50 000 to 150 000 and as such it can be expected that the flow in this regime will be laminar and that the aerodynamics will be mainly influenced by viscous effects.

The profile selection for the rotor blades was done by dividing the blade into three Re regions namely: 60 000 < Re > 80 000 for the first third inner section of the blade, 80 000 < Re > 110 000 for the middle section and 110 000 < Re > 150 000 for the outer section of the blade. To ensure structural integrity and ease of manufacturing, a thickness to chord ratio (t/c) in the order of 18%, 14% and 10% respectively were chosen for the three sections.

An airfoil database comparative search and analysis using XFOIL and XFLR 5 resulted in five sets of possible profiles. An analysis of the different rotors at design point and away from the design point indicated that the NACA 2418-14-08 sections were the better choice, since they were aerodynamically amongst the best and their much simpler geometry should result in higher structural integrity and easier manufacturing.

7.2.2 The shroud and design of the rotor system

The shroud used for the present work consists of the same cambered leading edge shroud and the symmetrical NACA derivative trailing edge as used by Lee (2010) in his research. The rotor radius was dictated by the shroud inner geometry of the existing shroud. The shroud throat (or minimum inner) diameter, D_t, is 0.3592 m to ensure a nominal tip clearance of 0.01R (0.001778 m) and the

shroud chord c_d is set at 0.2052 m. This resulted in a tip Mach number of 0.278 and 0.322 for a rotor speed of 5 000 and 6 000 rpm respectively, which would ensure incompressible flow conditions.

The goal of the blade design was to ensure maximum thrust at steady state for a given power supplied to the rotor shaft. This means that the blade AoA and Re should be optimal for the airfoil to ensure a high lift to drag (L/D) ratio. The detailed rotor blade geometry for the front and rear rotors is listed in Table 3.1 and Table 3.2.

7.2.3 CFD Simulation

Once the geometry of the SCRS was created with the DFDC code, AutoDesk Inventor 3D CAD was used to import the geometric data into ANSYS TurboGrid and ANSYS Mesher. Due to the axisymmetric nature of the problem, only one half of the model was analysed to save on computational time. The dimensions of the computational domain were selected so that the outer half cylindrical region extends 8 D_R ahead and 12 D_R downstream of the model while an extension of 5 D_R to each side was allowed.

The computational domain consists of an outer domain that hosts a smaller inner domain in which the shrouded contra rotating rotors are situated. An MFR method was used to simulate the flow activities in the stationary domains and the rotating rotor domains, while stage type interfaces were inserted between stationary and rotating frames as well as between the two rotating rotor frames. A general grid interface (GGI) was used to connect meshes where they did not match on either side of the two joined boundary surfaces and periodic interfaces were created on the symmetry planes.

The outer domain is predominantly filled with hexahedral elements with a smaller amount of pyramids and tetrahedral elements The unstructured mesh in the smaller inner domain hosts the shrouded rotor system. It consists primarily of tetrahedral and wedge elements.

The performance predictions of the DFDC code were done with the general purpose ANSYS-CFX 15.07 code, which is based on the finite volume method (FVM). CFX is capable of simulating the incompressible mean flow field flow past the contra-rotating shrouded rotor system for a UAV. The k-ω based SST turbulence model was used in this study. This low Re turbulence model was designed to give an accurate prediction of the start and the amount of fluid flow separation due to adverse pressure gradients. The model automatically resorts to a wall function formulation in the vicinity of coarse grid resolutions close to a wall. In this study boundary layer inflation was used in the smaller fluid domain and in the rotating fluid domains on all the walls, while edge inflation was used on the trailing edge of the shroud to fully benefit from the SST turbulence model.

For axial flow computation, an undisturbed velocity in the axial direction is specified for an inlet boundary condition and atmospheric static pressure is prescribed on the outlet surface. On the outer side wall of the cylinder, a free-slip-wall boundary condition is prescribed. An atmospheric static pressure at the inlet and outlet with an opening boundary condition on the sides were assumed for hover flight. Convergence of the problem was assumed after the residual RMS error values for P-Mass, U-Mom, V-Mom and W-Mom had reduced to a value less than 10^{-4}. Since the V-Momentum residual often could not satisfy this requirement it was verified that the thrust and torque values of both rotors had reached a steady solution for at least the last 50 consecutive iterations and that

the flow domain P-Mass, U-Mom, V-Mom and W-Mom imbalances were less than 1%.

The hover performance and the axial flight performance of the newly designed blades are compared to the experimental results as published by Lee (2010) and the ANSYS-CFX predictions. These comparisons indicate that the newly designed rotor system succeeded in most aspects of the design criteria.

The CFD predictions are less optimistic than the DFDC results, but they still indicate a 33% increase in total thrust for the design power input of 370 W at a rotational speed of 5 000 rpm in hover conditions.

The CFD predictions confirmed the DFDC calculations in terms of the total amount of thrust generated by the rotors for rotational speeds of 4 000 rpm, 5 000 rpm and 6 000 rpm. CFX indicates a slight difference in the torque predictions on the upper and lower rotors from the DFDC design values. There is however a significant difference in the shroud thrust predictions of DFDC and the CFD simulations.

This study further indicated that the DFDC code has the potential be used as a valuable preliminary design tool for the development of shrouded coaxial rotor systems for UAVs.

7.3 RECOMMENDATIONS FOR FUTURE WORK

Further research is required into the reasons why the shroud thrust of the DFDC code and the ANSYS-CFX predictions differ so much.

DFDC and CFX comparisons for more shrouded rotor configurations should be made to better understand the nature of the problem.

A more detailed boundary layer analysis on the shroud and hub should be investigated.

It is advisable that the computational mesh, specifically in the rotational domains, be optimised further.

Further research on the aerodynamic design of the shroud would most definitely contribute to an increase in the performance of the system.

The best scenario would be to build and test the shrouded counter rotating rotor system to verify the anticipated system performance experimentally.

REFERENCES

Ansys. 2009. Ansys-cfx solver theory guide. [Online] Available: www.ansys.com

Airfoil Tools. 2014. *Airfoil database search*. [Online]. Available: http://airfoiltools.com/search/index. [2013,June,24].

Akturk, A., Shavalikul, A., *Camci, C*. 2009. PIV Measurements and Computational Study of a 5-Inch Ducted Fan for V/STOL UAV Applications. *AIAA* 47th Aerospace Sciences Meeting and Exhibit, AIAA-2009-332. [Online]. Available at: http://arc.aiaa.org/doi/abs/10.2514/6.2009-332. [2014, Sept 10].

Betz, A. 1919. Screw propeller with minimum energy loss (Schraubenpropeller mit geringstem energieverlust). *Translation from German by DA Sinclair, Translation Section, NRC Library, Technical Translation* 736: 193-217.

Black, D., Wainauski, H. & Rohrbach, C. 1968. Shrouded propellers – a comprehensive performance study. *AIAA 5th Annual Meeting and Technology Display*, AIAA-68-99. [Online]. Available at: http://scholar.google.com/scholar?hl=en&btnG=Search&q=intitle:Shrouded+Propellers+A+Comprehensive+Performance+Study#0. [2014, July 4].

Bohorquez, F. 2007. *Rotor hover performance and system design of an efficient coaxial rotary wing micro air vehicle*. PhD Thesis, Department of Aerospace Engineering, University of Maryland. [Online]. Available: http://drum.lib.umd.edu/handle/1903/6704. [2012,July 15].

Bramwell, A.R.S., Done, G. & Balmford, D. 2001. *Bramwell's helicopter dynamics*. 2nd Ed. Oxford: Butterworth-Heinemann.

Coleman, C.P. 1997. A survey of theoretical and experimental coaxial rotor aerodynamic research*. National Aeronautics and Space Administration, Ames Research Center,* Vol. 3675, March.

Crigler, L.J. 1948. Application of Theodorsen's theory to propeller design. *National Advisory Committee for Aeronautics*, Report 924. [Online]. Available: http://naca.central.cranfield.ac.uk/reports/1949/naca-report-924.pdf. [2014, September 2].

Cycon, J.P., Rosen K.M.& Whyte A.C. 1992. Unmanned flight vehicle including counter rotating rotors positioned within a toroidal shroud and operable to provide all required vehicle flight controls. Patent US 5152478 A. [Online]. Available: http://www.google.co.za/patents/US5152478. [2014, June 24].

Denel Dynamics. 2014. Products. [Online]. Available: http://www.deneldynamics.co.za/products/uas/reconnaissance-systems/. [2014,March 9].

Drela, M. 1989. *XFOIL: An analysis and design system for low Reynolds number airfoils*. [Online]. Available: http://web.mit.edu/drela/Public/papers/xfoil_sv.pdf. [2012, January 27].

Drela, M. 2004. *XFOIL subsonic airfoil development system*. [Online]. Available: http://raphael.mit.edu/xfoil.[2011, August 8].

Drela, M. & Youngren, H. 2005. Axisymmetric analysis and design of ducted rotors. [Online]. Available: http://web.mit.edu/drela/Public/web/dfdc/DFDCtheory12-31.pdf. [2011, August 9].

Gur, O., & Rosen, A. 2008. Comparison between blade-element models of propellers. *Aeronautical Journal* 113.3277: 689-704. [Online]. Available: http://aerosociety.com/News/Publications/Aero-Journal/Online/528/Comparison-between-bladeelement-models-of-propellers. [2010, October 10].

Heise, R., Peddle, I.K., Jones, T. & Milne, G.R. 2006. SLADe: Development of a UAV Decoy. Paper presented at 32nd European Rotorcraft Forum, Maastricht, Netherlands, 12-14. Code 70024.

Hrishikeshavan, V. 2011. *Experimental investigation of shrouded rotor micro air vehicle in hover and in edgewise gusts*. University of Maryland at College Park. [Online]. Available: http://drum.lib.umd.edu/handle/1903/12351 [2014, June 15].

Johnson, W. 1980. *Helicopter Theory*. New York: Dover Publications.

Ko, A., Ohanian, O.J., Gelhausen, P. 2007. Ducted fan UAV modeling and simulation in preliminary design. Paper presented at AIAA Modeling and Simulation Technologies Conference and Exhibit, Hilton Head, South Carolina, 20-23 August. [Online]. Available: http://arc.aiaa.org/doi/abs/10.2514/6.2007-6375. [2009, June 1].

Kotwani, K. n.d. *Ducted fan or shrouded rotor aerodynamics and its applications in VTOL miniature aerial vehicles.* AE 416 Project. [Online]. Available: http://issuu.com/jeanlulu/docs/ducted-fan-or-shrouded-rotor-aerodynamics-and-its-. [2012, August 4].

Krüger, W. 1949. *On wind tunnel tests and computations concerning the problem of shrouded propellers*. NACA Technical Memorandum No. 1202. [Online]. Available: http://naca.central.cranfield.ac.uk/reports/1949/naca-tm-1202.pdf. [2012, August 6].

Küchemann, D. & Weber, J. 1953. *Aerodynamics of Propulsion*. New York: McGraw-Hill.

Lednicer, D. 2010. *The incomplete guide to airfoil usage*. [Online]. Available: http://aerospace.illinois.edu/m-selig/ads/aircraft.html. [2011, August 3].

Lee, T.E. 2010. Design and performance of a ducted coaxial rotor in hover and forward flight. MSc thesis, Faculty of the Graduate School of the University of Maryland. [Online]. Available: http://drum.lib.umd.edu/handle/1903/11300. [2012, November 15].

Leishman, J.G. 2006. *Principles of helicopter aerodynamics.* 2nd Ed. New York: Cambridge University Press.

Leishman, J., & Syal, M. 2008. Figure of merit definition for coaxial rotors. *Journal of the American Helicopter Society* 53.3: 290-300. [Online]. Available: http://www.ingentaconnect.com/content/ahs/jahs/2008/00000053/00000003/art00007. [2012, August 28].

Martin, P. & Boxwell, D. 2005. *Design, analysis and experiments on a 10-inch ducted rotor VTOL UAV*. Paper presented at AHS International Specialists'

Meeting - Unmanned Rotorcraft: Design, Control and Testing in Chandler, AZ, January. Available: https://vtol.org/store/product/design-analysis-and-experiments-on-a-10inch-ducted-rotor-vtol-uav-8174.cfm. [2014, August 6].

Martin, P. & Tung, C. 2004. *Performance and flowfield measurements on a 10-inch ducted rotor VTOL UAV*. [Online]. Available: rotorcraft.arc.nasa.gov/publications/files/Martin_2004.pdf.

McCormick, B.W. 1967. *Aerodynamics of V/STOL flight*. New York: Academic Press.

Miller, P.M., Manager, P. & Goodrich, M.K. 2006. Report by the Federal Research Division, Library of Congress, Washington, DC. [Online]. Available: http://www.researchgate.net/publication/235139475_Mini_Micro_and_Swarming_Unmanned_Aerial_Vehicles_A_Baseline_Study. [2014 July 31].

Mort, K. 1965. *Performance characteristics of a 4-foot-diameter ducted fan at zero angle of attack for several fan blade angles*. NASA Technical Note NASA TN D-3122: 20. [Online]. Available: http://ntrs.nasa.gov/archive/nasa/casi.ntrs.nasa.gov/19660002851.pdf. [2014 , June 23].

Mort, K.W. & Gamse, B. 1967. *A wind tunnel investigation of a 7-foot-diameter ducted propeller*. NASA Technical Note TN D-4142. [Online]. Available: http://ntrs.nasa.gov/archive/nasa/casi.ntrs.nasa.gov/19670025554.pdf. [2014, June 24].

Mueller, T.J. & DeLaurier, J.D. 2003. Aerodynamics of small vehicles. *Annual Review of Fluid Mechanics* 35.1: pp.89-111. [Online] Available: http://www.annualreviews.org/doi/abs/10.1146/annurev.fluid.35.101101.161102. [2014, June 12].

Pereira, J.L. 2008. *Hover and wind-tunnel testing of shrouded rotors for improved micro air vehicle design*. PhD thesis, Department of Aerospace Engineering, University of Maryland. [Online]. Available: http://drum.lib.umd.edu/handle/1903/8752. [2014, June 15].

Pereira, J.L. & Chopra, I. 2009. Hover tests of micro aerial vehicle – scale shrouded rotors, Part I performance characteristics. *Journal of the American Helicopter Society* 54.1: 012001-1 to 012001-28.

Pines, D.J. & Bohorquez, F. 2006. Challenges facing future micro-air-vehicle development. *Journal of Aircraft* 43.2: 290-305. [Online]. Available: http://arc.aiaa.org/doi/abs/10.2514/1.4922. [2014, June 30].

Platt, R.J. Jnr. 1948. *Static tests of a shrouded and an unshrouded propeller*. NACA Research Memorandum L7H26. [Online]. Available: http://www.dtic.mil/dtic/tr/fulltext/u2/a800783.pdf. [2014, Sept 10].

Pounds, P. & Mahony, R. 2004. *Small-scale aeroelastic rotor simulation, design and fabrication*. [Online]. Available: http://www.araa.asn.au/acra/acra2005/papers/pounds.pdf. [2014, April.20]

Sacks, A.H., & Burnell, J.A.1962. Ducted propellers – a critical review of the state of the art. *Progress in Aeronautical Sciences* 3: 85-135.

Taylor, M. 1950. *A balsa-dust technique for air-flow visualization and its application to flow through model helicopter rotors in static thrust*. National Advisory Committee for Aeronautics, Technical Note 2220. [Online]. Available:

http://naca.central.cranfield.ac.uk/reports/1950/naca-tn-2220.pdf. [2012, August 25].

Theodorsen, T. (1948). *Theory of Propellers*. [Online]. Available: http://ittc.sname.org/proc7/Theory%20of%20Propellers.pdf. [Year, Month day].

Van der Spuy, S. & Von Backström, T.W. 2007. Aerodynamic design of a surface launched aerial decoy.

Yaggy, P. & Goodson, K. 1960. *Aerodynamics of tilting ducted-fan configurations*. , Paper presented at NASA Conference on V/STOL Aircraft, Langley Research Center, Langley Field, Va, November 17-18. [Online]. Available: http://ntrs.nasa.gov/archive/nasa/casi.ntrs.nasa.gov/19630004807.pdf#page=63 [2014, June 15].

Yaggy, P. & Mort, K., 1961. *A wind-tunnel investigation of a 4-foot-diameter ducted fan mounted on the tip of a semispan wing*. NASA Technical Note D-776. [Online]. Available: http://babel.hathitrust.org/cgi/pt?id=uiug.30112106740704;view=1up;seq=1. [2014, June 15].

APPENDIX A: NACA 2418-14-10 POLAR DIAGRAMS

The XFOIL generated polar diagrams of the NACA 2418-14-10 parent airfoil sections at various Reynolds numbers.

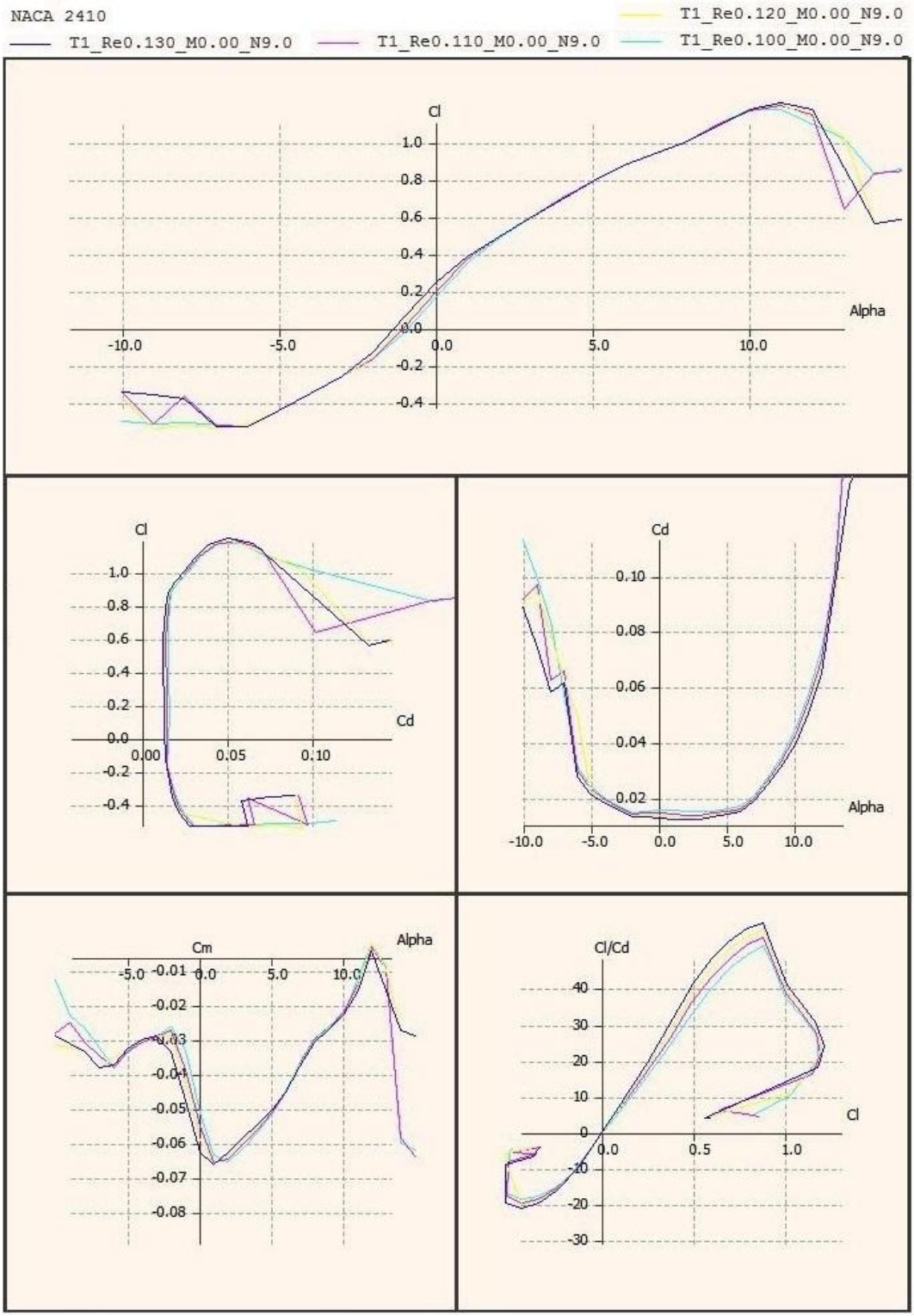

Figure A.1: NACA 2410 Polar Diagram.

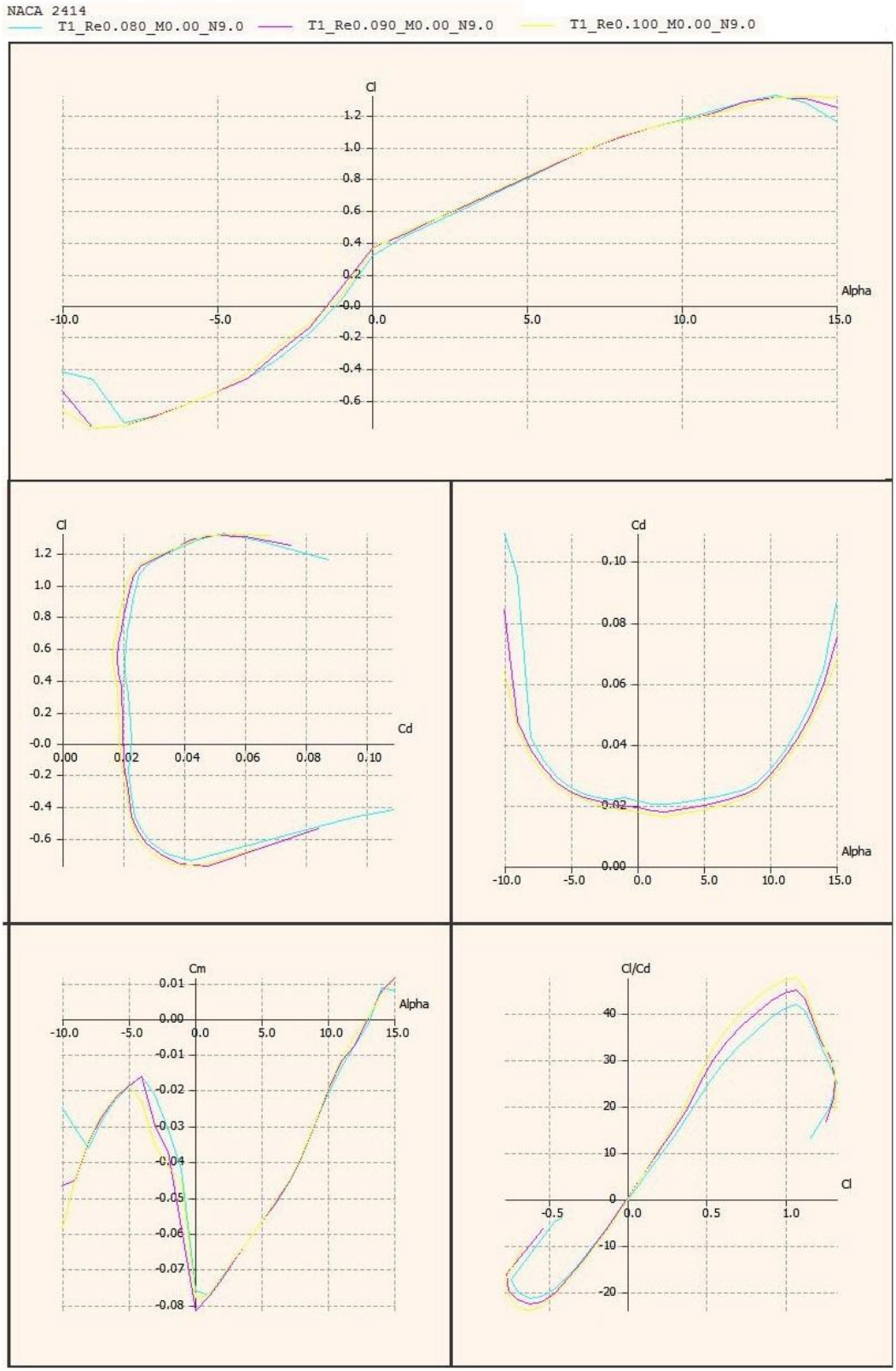

Figure A.2: NACA 2414 Polar Diagram.

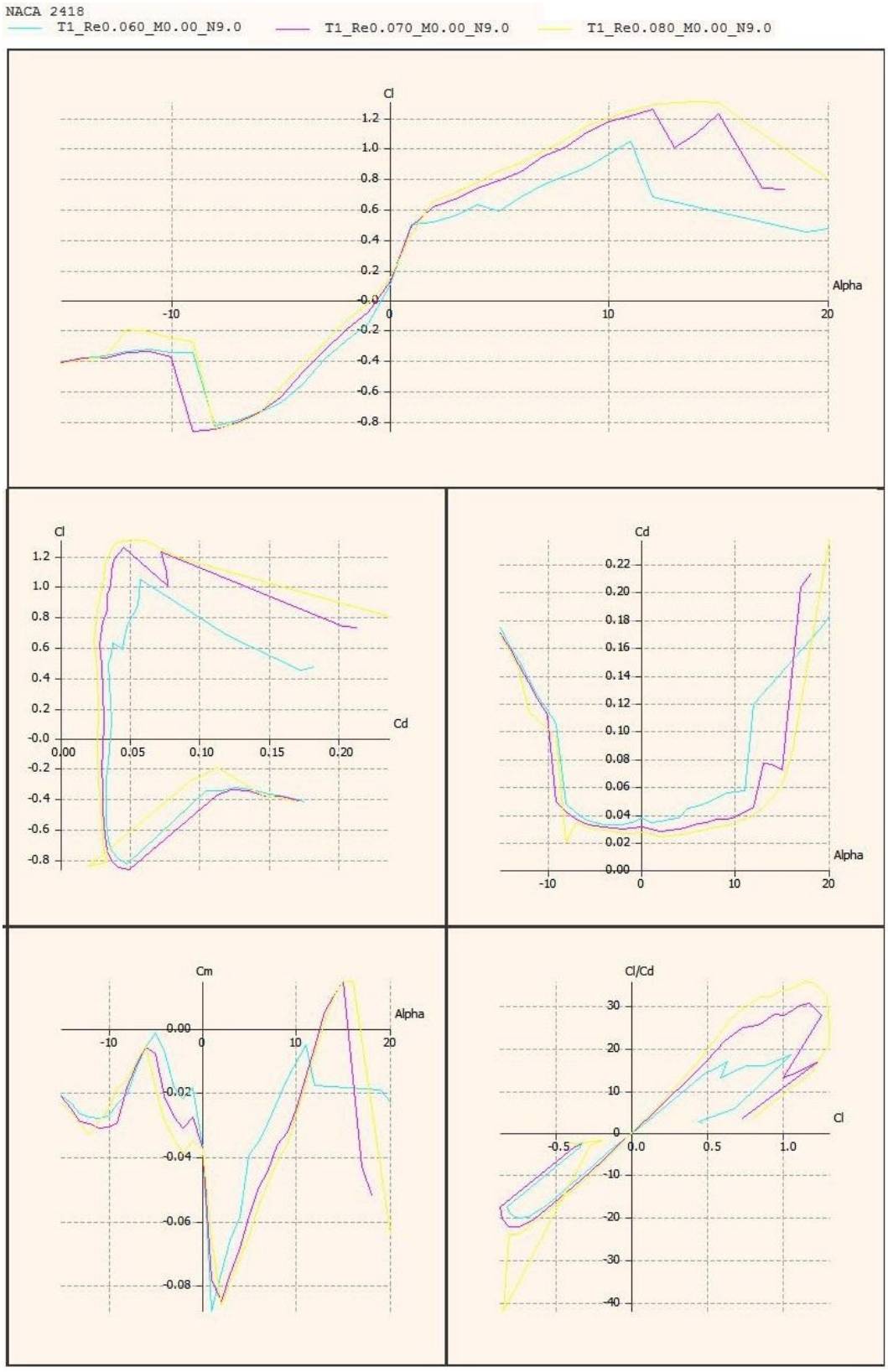

Figure A.3: NACA 2418 Polar Diagram.

APPENDIX B: DFDC INPUT FILE

An example of a DFDC input file with the NACA2418-4-10 parent airfoil sections prescribed for the rotor blade design of a CSCR. In this example the S3 rotor-to-rotor spacing and P3 rotor-to-shroud position with a 1% R tip gap is set.

```
DFDC Version 0.70E+03
TG1-S3P3-NACA2418-14-10

OPER
!    Vinf            Vref            RPM1            RPM2
     0               25              5000            -5000
!    Rho             Vso             Rmu             Alt
     1.226           340             0.0000178       0
!    XDwake          Nwake
     0.8             20
!    Lwkrlx
     F
ENDOPER

AERO
!    #sections
     3
!    Xisection
     0.167
!    A0deg           dCLdA           CLmax           CLmin
     -0.9000         5.5730          1.3000          -0.9000
!    dCLdAstall      dCLstall        Cmconst         Mcrit
     1.7190          0.0300          -0.0300         0.6000
!    CDmin           CLCDmin         dCDdCL^2
     0.0240          0.6600          0.0180
!    REref           REexp           TOC             dCDdCL^2
     80000.0000      -0.6000         0.1800          0.0180
     0.6
!    A0deg           dCLdA           CLmax           CLmin
     -1.4600         5.3930          1.3000          -0.7600
!    dCLdAstall      dCLstall        Cmconst         Mcrit
     1.1460          0.0200          -0.0400         0.7000
!    CDmin           CLCDmin         dCDdCL^2
     0.0180          0.4000          0.0480
!    REref           REexp           TOC             dCDdCL^2
     90000.0000      -0.6000         0.1400          0.0480
     1
!    A0deg           dCLdA           CLmax           CLmin
     -1.2000         5.3860          1.2000          -0.5200
!    dCLdAstall      dCLstall        Cmconst         Mcrit
     1.7190          0.0300          -0.0400         0.7000
!    CDmin           CLCDmin         dCDdCL^2
     0.0130          0.4000          0.0380
!    REref           REexp           TOC             dCDdCL^2
     120000.0000     -0.6000         0.1000          0.0380
ENDAERO

ROTOR
!    Xdisk           Nblds           NRsta
     0.11414         2               11
!    #stations
     12
!    r               Chord           Beta
     3.70E-02        4.82E-02        51.287
     5.16E-02        3.92E-02        40.324
     6.63E-02        3.28E-02        33.46
     8.09E-02        2.83E-02        28.808
     9.55E-02        2.50E-02        25.432
```

```
    0.11017     2.26E-02    22.884
    0.12481     2.07E-02    20.953
    0.13944     1.92E-02    19.375
    0.15407     1.80E-02    18.019
    0.16871     1.72E-02    16.805
    0.17691     1.69E-02    16.172
    0.17869     1.68E-02    16.04
ENDROTOR

AERO
!   #sections
    3
!   Xisection
    0.167
!   A0deg       dCLdA       CLmax       CLmin
    -0.9        5.573       0.9         -1.3
!   dCLdAstall  dCLstall    Cmconst     Mcrit
    0.172       3.00E-02    -3.00E-02   0.6
!   CDmin       CLCDmin     dCDdCL^2
    2.40E-02    -0.66       1.80E-02
!   REref       REexp       TOC         dCDdCL^2
    80000       -0.6        0.18        1.80E-02
    0.6
!   A0deg       dCLdA       CLmax       CLmin
    -1.46       5.393       0.76        -1.3
!   dCLdAstall  dCLstall    Cmconst     Mcrit
    1.146       2.00E-02    -4.00E-02   0.7
!   CDmin       CLCDmin     dCDdCL^2
    1.80E-02    -0.4        4.80E-02
!   REref       REexp       TOC         dCDdCL^2
    90000       -0.6        0.14        4.80E-02
    1
!   A0deg       dCLdA       CLmax       CLmin
    -1.2        5.386       0.52        -1.2
!   dCLdAstall  dCLstall    Cmconst     Mcrit
    1.719       3.00E-02    -4.00E-02   0.7
!   CDmin       CLCDmin     dCDdCL^2
    1.30E-02    -0.4        3.80E-02
!   REref       REexp       TOC         dCDdCL^2
    1.20E+05    -0.6        0.1         3.80E-02
ENDAERO

ROTOR
!   Xdisk       Nblds       NRsta
    0.16748     2           11
!   #stations
    12
!   r           Chord       Beta
    3.70E-02    4.19E-02    131.34
    5.15E-02    3.57E-02    139.14
    6.61E-02    3.08E-02    144.76
    8.08E-02    2.71E-02    148.87
    9.54E-02    2.42E-02    151.96
    0.11005     2.21E-02    154.4
    0.1247      2.03E-02    156.51
    0.13936     1.90E-02    158.29
    0.15402     1.79E-02    159.81
    0.16869     1.70E-02    161.15
    0.17691     1.66E-02    161.82
    0.17869     1.65E-02    161.96
ENDROTOR
```

GEOM
Sym.centerbody

0.264626	0.019691		0.015673	0.022983	0.033594	0.194657
0.262078	0.021024		0.013671	0.021512	0.032317	0.193486
0.259245	0.022416		0.011638	0.01983	0.0313	0.192268
0.256384	0.02367		0.009668	0.01801	0.030558	0.190991
0.253231	0.024885		0.007784	0.016052	0.03012	0.189657
0.250108	0.026071		0.006029	0.014041	0.030005	0.188285
0.247411	0.02694		0.004489	0.012041	0.030228	0.186909
0.244746	0.027567		0.003167	0.010063	0.030757	0.185591
0.241802	0.028087		0.002076	0.00811	0.031559	0.184362
0.238536	0.028543		0.00121	0.006166	0.03261	0.183245
0.235035	0.028923		0.000564	0.004211	0.033887	0.182248
0.231351	0.029233		0.000143	0.002214	0.035372	0.181383
0.227556	0.02948	999.00	999.00		0.037055	0.180664
0.223842	0.029642		0.2352	0.180111	0.038929	0.180101
0.22008	0.029705		0.232265	0.181018	0.041018	0.179733
0.215895	0.029703		0.228352	0.182203	0.043437	0.179577
0.211284	0.029689		0.223821	0.183538	0.046506	0.179568
0.206574	0.029693		0.21904	0.184907	0.050642	0.179584
0.201769	0.029695		0.214189	0.186254	0.055705	0.179577
0.19692	0.029692		0.209292	0.187574	0.061256	0.179578
0.192053	0.029693		0.204358	0.188864	0.067027	0.179579
0.187158	0.029693		0.199403	0.190123	0.072881	0.179578
0.182245	0.029693		0.194465	0.191341	0.078759	0.179578
0.177325	0.029693		0.189524	0.192518	0.08465	0.179578
0.172403	0.029693		0.184558	0.193662	0.090546	0.179578
0.16748	0.029693		0.179603	0.194767	0.096444	0.179578
0.162631	0.029693		0.174648	0.195831	0.102343	0.179578
0.157782	0.029693		0.169733	0.196848	0.108241	0.179578
0.152933	0.029693		0.164826	0.197817	0.11414	0.179578
0.148084	0.029693		0.159931	0.198743	0.118989	0.179578
0.143235	0.029693		0.155072	0.199615	0.123838	0.179578
0.138386	0.029693		0.150242	0.200436	0.128687	0.179578
0.133536	0.029693		0.145465	0.201197	0.133536	0.179578
0.128687	0.029693		0.140746	0.201897	0.138385	0.179578
0.123838	0.029693		0.136067	0.202531	0.143235	0.179578
0.118989	0.029693		0.131426	0.203103	0.148084	0.179578
0.11414	0.029693		0.12685	0.203605	0.152933	0.179578
0.109228	0.029693		0.122339	0.204035	0.157782	0.179578
0.104317	0.029693		0.117884	0.204388	0.162631	0.179578
0.099405	0.029693		0.113505	0.204664	0.16748	0.179578
0.094494	0.029693		0.109171	0.204856	0.172275	0.179578
0.089586	0.029693		0.104887	0.204965	0.177069	0.179578
0.084684	0.029693		0.100359	0.204978	0.181864	0.179578
0.07979	0.029692		0.095517	0.205014	0.186659	0.179578
0.074927	0.029692		0.090447	0.205013	0.191454	0.179578
0.070105	0.029696		0.085265	0.20501	0.196248	0.179578
0.065467	0.029692		0.080274	0.204977	0.201043	0.179578
0.060959	0.029659		0.075848	0.204913	0.205837	0.179578
0.056417	0.029597		0.071837	0.204746	0.21063	0.179578
0.051913	0.029513		0.067947	0.204479	0.215416	0.179578
0.047585	0.029401		0.064152	0.204114	0.220177	0.179578
0.043461	0.029248		0.060435	0.203647	0.224833	0.179578
0.039546	0.029044		0.056829	0.203087	0.229139	0.179578
0.035894	0.028783		0.053365	0.202431	0.23264	0.179578
0.032552	0.028454		0.050059	0.201684	0.2352	0.179578
0.029507	0.028043		0.046946	0.200855	ENDGEOM	
0.026755	0.027545		0.044056	0.199949		
0.024271	0.026941		0.041415	0.198978		
0.021974	0.026195		0.039041	0.197954		
0.019785	0.025285		0.036949	0.19689		
0.017684	0.024221		0.035137	0.195789		

```
PANELING
!    #elements      #refinement zones
     2              4
!    #panel nodes
     74
!    curv_expon     curv_smooth dsL/dsAvg dsR/dsAvg
     1              1           0.6       0.6
!    s1/smax        s2/smax     ds/dsAvg
     0              0           1
     0              0           1
     0              0           1
     0              0           1
!    #panel nodes
     99
!    curv_expon     curv_smooth dsL/dsAvg dsR/dsAvg
     1              1           0.6       0.6
!    s1/smax        s2/smax     ds/dsAvg
     0              0           1
     0              0           1
     0              0           1
     0              0           1
ENDPANELING
```

APPENDIX C: DFDC OUTPUT FILE

An example of a DFDC output file with the NACA2418-4-10 parent airfoil sections prescribed for the rotor blade design of a CSCR. In this example the S3 rotor-to-rotor spacing and P3 rotor-to-shroud position with a 1% R tip gap is set.

DFDC Case: TG1-S3P3-NACA2418-14-10

Flow Condition and total Forces Corrected for blade blockage

Vinf(m/s) :	0.000	Alt.(km) :	0.000	DeltaT(dgC):	0.0000
rho(kg/m3) :	1.2260	Vsound(m/s):	340.000	mu(kg/m-s) :	0.1780E-04
Thrust(N) :	35.4	Power(W) :	363	Efficiency :	0.0000
Tvisc (N) :	-0.2014	Pvisc(W) :	38.5	Induced Eff:	0.0000
Tduct(N) :	17.3179	torQue(N-m):	0.312E-02	Ideal Eff :	0.0000

Area:	0.09854	Radius:	0.17958	Omega:	523.59882	Reference data
Ct:	0.24956	Cp:	0.08563	J:	0	by(Rho,N,Dia)
Tc:	0	Pc:	0	adv:	0	by(Rho,Vinf,Area)
CT0:	0.0331	CP0:	0.00362	FOM:	0.83289	by(Rho,R*Omg,Area)

Disk # 1 Bladed Rotor

# blades :	2	RPM :	5000.000	adv. ratio :	0.0000
Thrust(N) :	8.95	Power(W) :	182	Efficiency :	0.0000
Tvisc (N) :	-0.1018	Pvisc(W) :	19.3	Induced Eff:	0.0000
torQue(N-m)	0.3483	Qvisc(N-m) :	0.311	Ideal Eff :	0.0000
radius(m) :	0.1796	hub rad.(m):	0.0297	VAavg (m/s):	17.6793

Area:	0.09854	Radius:	0.17958	Omega:	523.59882	Reference data
Ct:	0.06320	Cp:	0.04301	J:	0.00000	by(Rho,N,Dia)
Tc:	0.00000	Pc:	0.00000	adv:	0.00000	by(Rho,Vinf,Area)
CT0:	0.00838	CP0:	0.00182			by(Rho,R*Omg,Area)
Sigma:	0.06966	CT0/Sig:	0.12033			

---

i	r/R	c/R	beta deg	alfa	CL	CD	REx10^3	Mach	B*Gam
1	0.206	0.2686	51.29	6.16	0.692	0.0241	82.81	0.073	0.832
2	0.288	0.2181	40.32	6.37	0.719	0.0254	83.58	0.091	0.872
3	0.369	0.1824	33.46	6.37	0.726	0.0265	85.2	0.111	0.898
4	0.451	0.1575	28.81	6.25	0.722	0.0269	87.45	0.132	0.916
5	0.532	0.1392	25.43	6.05	0.71	0.0267	89.89	0.154	0.927
6	0.614	0.1256	22.88	5.83	0.696	0.0258	92.64	0.175	0.936
7	0.695	0.1151	20.95	5.67	0.678	0.0239	95.54	0.197	0.941
8	0.776	0.107	19.38	5.5	0.66	0.022	98.78	0.22	0.947
9	0.858	0.1004	18.02	5.32	0.641	0.0202	102.07	0.242	0.95
10	0.939	0.0956	16.8	5.12	0.62	0.0184	106.13	0.264	0.956
11	0.985	0.0939	16.17	5.01	0.609	0.0174	109.1	0.276	0.964
12	0.995	0.0936	16.04	0	0	0	0	0	0

Disk # 2 Bladed Rotor

# blades :	2	RPM :	-5000.000	adv. ratio :	0.0000
Thrust(N) :	9.08	Power(W) :	181.	Efficiency :	0.0000
Tvisc (N) :	-0.0996	Pvisc(W) :	19.1	Induced Eff:	0.0000
torQue(N-m):	-0.3451	Qvisc(N-m) :	-0.309	Ideal Eff :	0.0000
radius(m) :	0.1796	hub rad.(m):	0.0297	VAavg (m/s):	17.6402

Area:	0.09854	Radius:	0.17958	Omega:	-523.598 Reference data
Ct:	0.06411	Cp:	0.04262	J:	0.00000 by(Rho,N,Dia)
Tc:	0.00000	Pc:	0.00000	adv:	0.00000 by(Rho,Vinf,Area)
CT0:	0.00850	CP0:	0.00180		by(Rho,R*Omg,Area)
Sigma:	0.06867	CT0/Sig:	0.12383		

-global coords-

i	r/R	c/R	beta deg	alfa	CL	CD	REx10^3	Mach	B*Gam
1	0.206	0.2335	131.34	-8.26	-0.712	0.0242	80.21	0.082	-0.829
2	0.287	0.1987	139.14	-8.62	-0.733	0.0247	82.31	0.099	-0.876
3	0.368	0.1715	144.76	-8.74	-0.732	0.0252	84.64	0.117	-0.899
4	0.45	0.1508	148.87	-8.75	-0.72	0.0255	87.14	0.137	-0.911
5	0.531	0.135	151.96	-8.72	-0.705	0.0257	89.78	0.158	-0.919
6	0.613	0.1228	154.4	-8.62	-0.686	0.0253	92.6	0.179	-0.922
7	0.694	0.1132	156.51	-8.35	-0.668	0.0233	95.6	0.201	-0.927
8	0.776	0.1056	158.29	-8.05	-0.647	0.0213	98.8	0.223	-0.928
9	0.858	0.0994	159.81	-7.75	-0.626	0.0195	102.21	0.244	-0.929
10	0.939	0.0945	161.15	-7.42	-0.603	0.0178	105.9	0.266	-0.927
11	0.985	0.0922	161.82	-7.04	-0.571	0.0163	108.24	0.279	-0.897
12	0.995	0.0918	161.96	0	0	0	0	0	0

Force Summary

TG1-S3P3-NACA2418-14-10

Qinf =	0.0000	Rho =	1.2260
Qref =	25.000	Mach =	0.0000
unitRN =	68876.	q_ref =	383.13

Total Forces

Fx =	-17.545	Cx =	-4.58E-02
Fxinv =	-17.297	Cxinv =	-4.51E-02
Fxvis =	-0.24807	Cxvis =	-6.47E-04

Element 1

Fx =	-0.23597	Cx =	-6.16E-04
Fxinv =	-0.26071	Cxinv =	-6.80E-04
Fxvis =	2.47E-02	Cxvis =	6.46E-05
QnDOF=	4.85E-04		

Element 2

Fx =	-17.33	Cx =	-4.52E-02
Fxinv =	-17.057	Cxinv =	-4.45E-02
Fxvis =	-0.27281	Cxvis =	-7.12E-04
QnDOF=	-1.89E-03		

Element 3

Fx =	0.10545E-01	Cx =	0.27524E-04
Fxinv =	0.10545E-01	Cxinv =	0.27524E-04
Fxvis =	0.0000	Cxvis =	0.0000
QnDOF=	-0.0000		

Element 4

Fx =	0.10177E-01	Cx =	0.26562E-04
Fxinv =	0.10177E-01	Cxinv =	0.26562E-04
Fxvis =	0.0000	Cxvis =	0.0000
QnDOF=	-0.0000		

Rotor velocities

QINF = 0.0000

QREF = 25.0000

OMEGA = 523.5988

RPM = 5000.0005

Induced vel, flow angles in absolute frame (downstream of disk)

r	Vxi	Vri	Vmi	Vti	Vi	Swirl(deg)
3.70E-02	16.19	-8.20E-02	16.19	3.577	16.58	12.46
5.16E-02	16.34	-0.2494	16.34	2.688	16.56	9.344
6.63E-02	16.5	-0.4277	16.5	2.156	16.64	7.447
8.09E-02	16.69	-0.5891	16.7	1.802	16.79	6.166
9.55E-02	16.9	-0.7151	16.91	1.544	16.98	5.222
0.1102	17.14	-0.7893	17.16	1.352	17.21	4.51
0.1248	17.39	-0.7967	17.41	1.2	17.45	3.947
0.1394	17.64	-0.7273	17.66	1.081	17.69	3.505
0.1541	17.85	-0.5888	17.86	0.9811	17.89	3.146
0.1687	17.98	-0.4945	17.99	0.9016	18.01	2.871
0.1769	18.01	-1.406	18.07	0.8672	18.09	2.756
0.1787	15.58	-1.093	15.62	0	15.62	0

Velocities, flow angles in absolute frame (downstream of disk)

r	Vx	Vr	Vm	Vt	V	Swirl(deg)
3.70E-02	17.66	-8.20E-02	17.66	3.577	18.02	11.45
5.16E-02	17.3	-0.2494	17.3	2.688	17.51	8.832
6.63E-02	17.2	-0.4277	17.2	2.156	17.34	7.148
8.09E-02	17.22	-0.5891	17.23	1.802	17.33	5.974
9.55E-02	17.33	-0.7151	17.34	1.544	17.41	5.092
0.1102	17.49	-0.7893	17.51	1.352	17.56	4.418
0.1248	17.69	-0.7967	17.71	1.2	17.75	3.881
0.1394	17.9	-0.7273	17.91	1.081	17.95	3.456
0.1541	18.07	-0.5888	18.08	0.9811	18.1	3.108
0.1687	18.17	-0.4945	18.18	0.9016	18.2	2.841
0.1769	18.19	-1.406	18.24	0.8672	18.26	2.73
0.1787	15.73	-1.093	15.77	0	15.77	0

Velocities, flow angles relative to blade frame (downstream of disk)

r	Wx	Wr	Wm	Wt	W	Phi(deg)
3.70E-02	17.66	-8.20E-02	17.66	-15.8	23.7	48.19
5.16E-02	17.3	-0.2494	17.3	-24.35	29.87	35.39
6.63E-02	17.2	-0.4277	17.2	-32.55	36.81	27.85
8.09E-02	17.22	-0.5891	17.23	-40.56	44.07	23.01
9.55E-02	17.33	-0.7151	17.34	-48.48	51.49	19.67
0.1102	17.49	-0.7893	17.51	-56.34	58.99	17.25
0.1248	17.69	-0.7967	17.71	-64.15	66.55	15.42
0.1394	17.9	-0.7273	17.91	-71.93	74.13	13.97
0.1541	18.07	-0.5888	18.08	-79.69	81.72	12.77
0.1687	18.17	-0.4945	18.18	-87.43	89.3	11.74
0.1769	18.19	-1.406	18.24	-91.76	93.56	11.21
0.1787	15.73	-1.093	15.77	-93.56	94.88	9.543

Velocities in blade frame, on blade lifting line
flow angle from plane of rotation

r	Wx	Wr	Wm	Wt	W	Phi(deg)
3.70E-02	17.66	-8.20E-02	17.66	-17.59	24.93	45.12
5.16E-02	17.3	-0.2494	17.3	-25.7	30.98	33.95
6.63E-02	17.2	-0.4277	17.2	-33.62	37.77	27.09
8.09E-02	17.22	-0.5891	17.23	-41.46	44.9	22.56
9.55E-02	17.33	-0.7151	17.34	-49.25	52.22	19.38
0.1102	17.49	-0.7893	17.51	-57.01	59.64	17.06
0.1248	17.69	-0.7967	17.71	-64.75	67.13	15.28
0.1394	17.9	-0.7273	17.91	-72.47	74.65	13.87
0.1541	18.07	-0.5888	18.08	-80.18	82.19	12.7
0.1687	18.17	-0.4945	18.18	-87.88	89.74	11.68
0.1769	18.19	-1.406	18.24	-92.2	93.98	11.16
0.1787	15.73	-1.093	15.77	-93.56	94.88	9.543

APPENDIX D: DFDC OUTPUT PLOTS

DFDC output plot files with the NACA2418-4-10 parent airfoil sections prescribed for the upper rotor blade design of a CSCR. In this example the S3 rotor-to-rotor spacing and P3 rotor-to-shroud position with a 1% R tip gap is set.

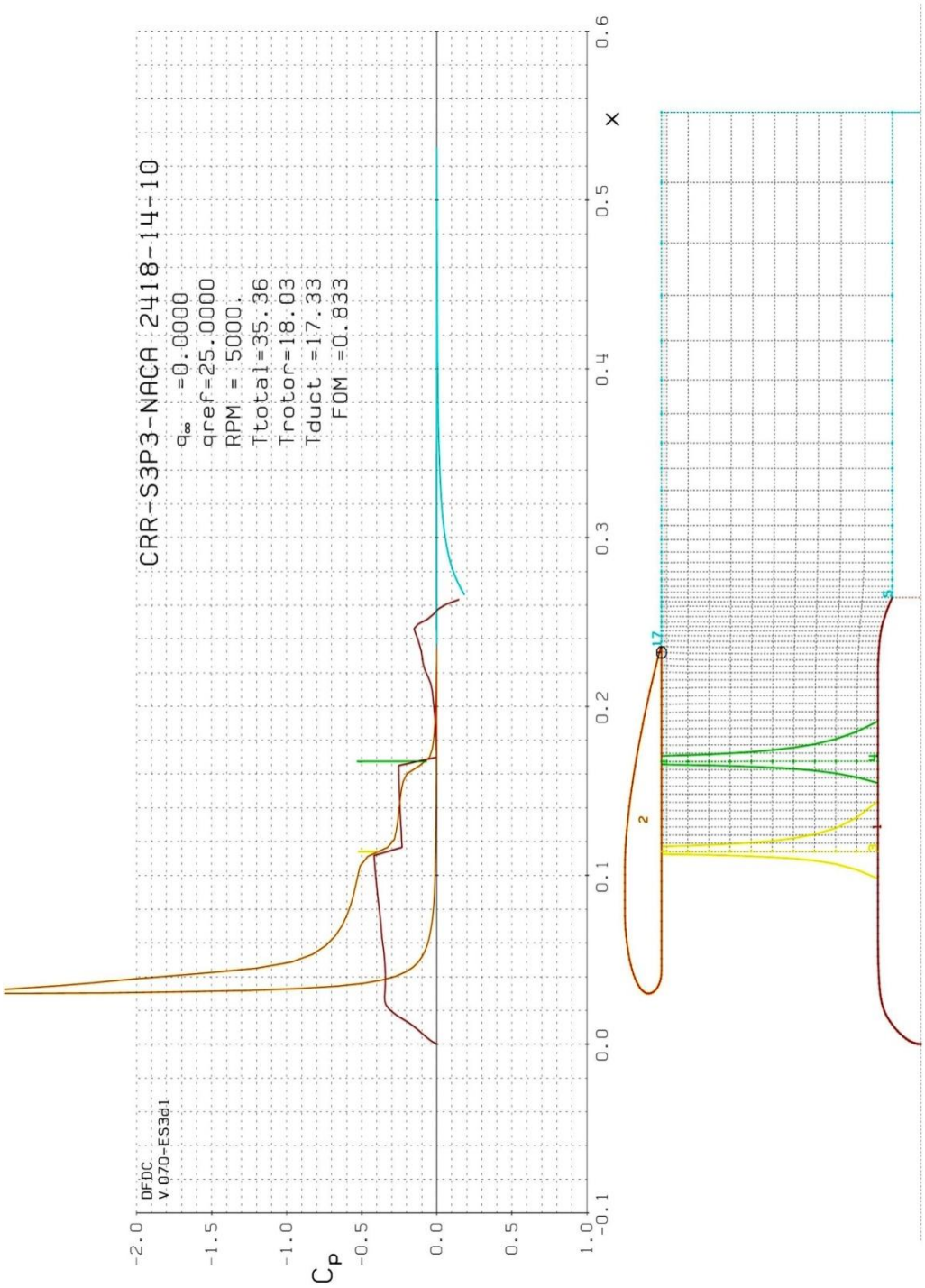

Figure D.1: C_p plot.

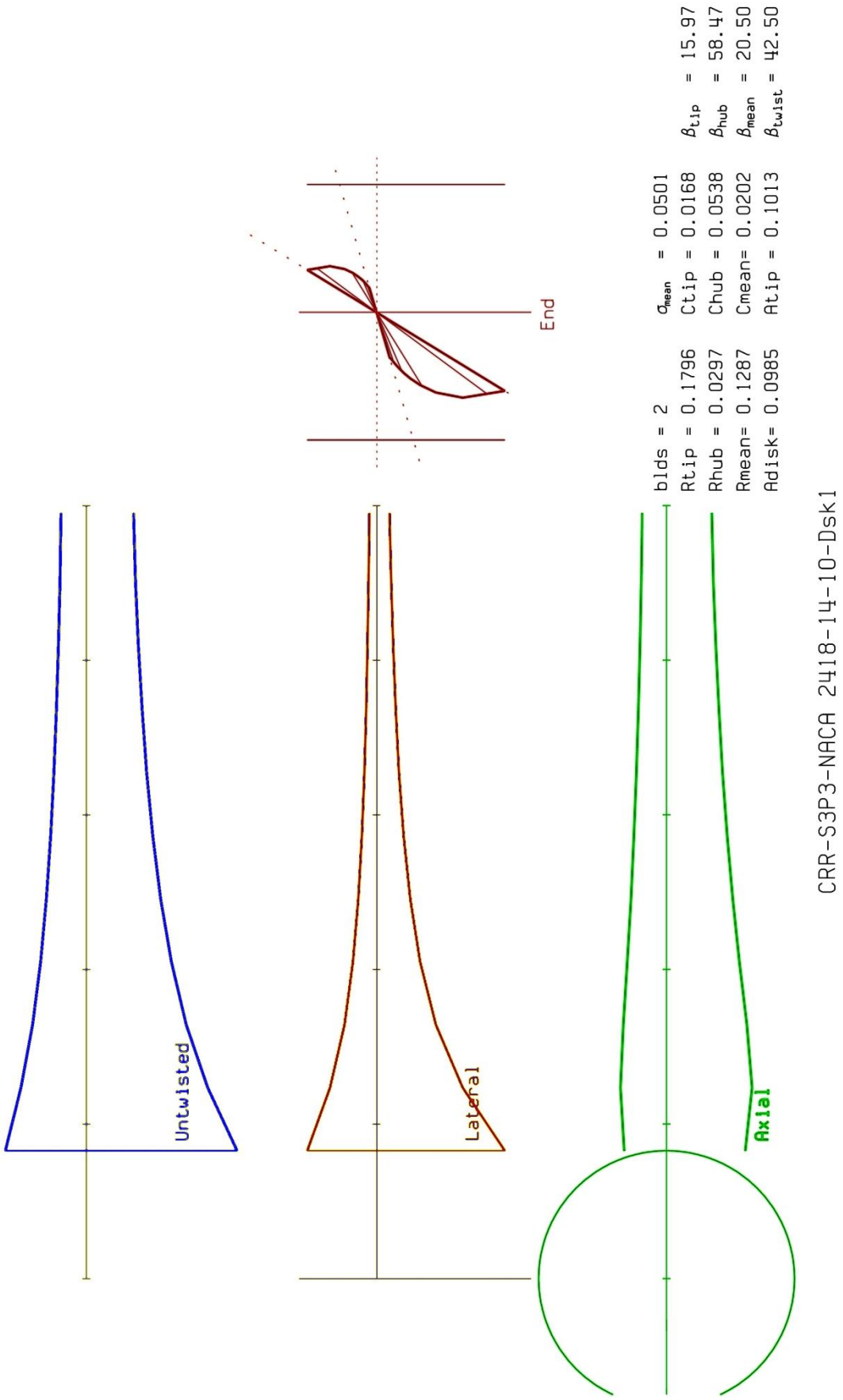

Figure D.2: Blade geometry and twist.

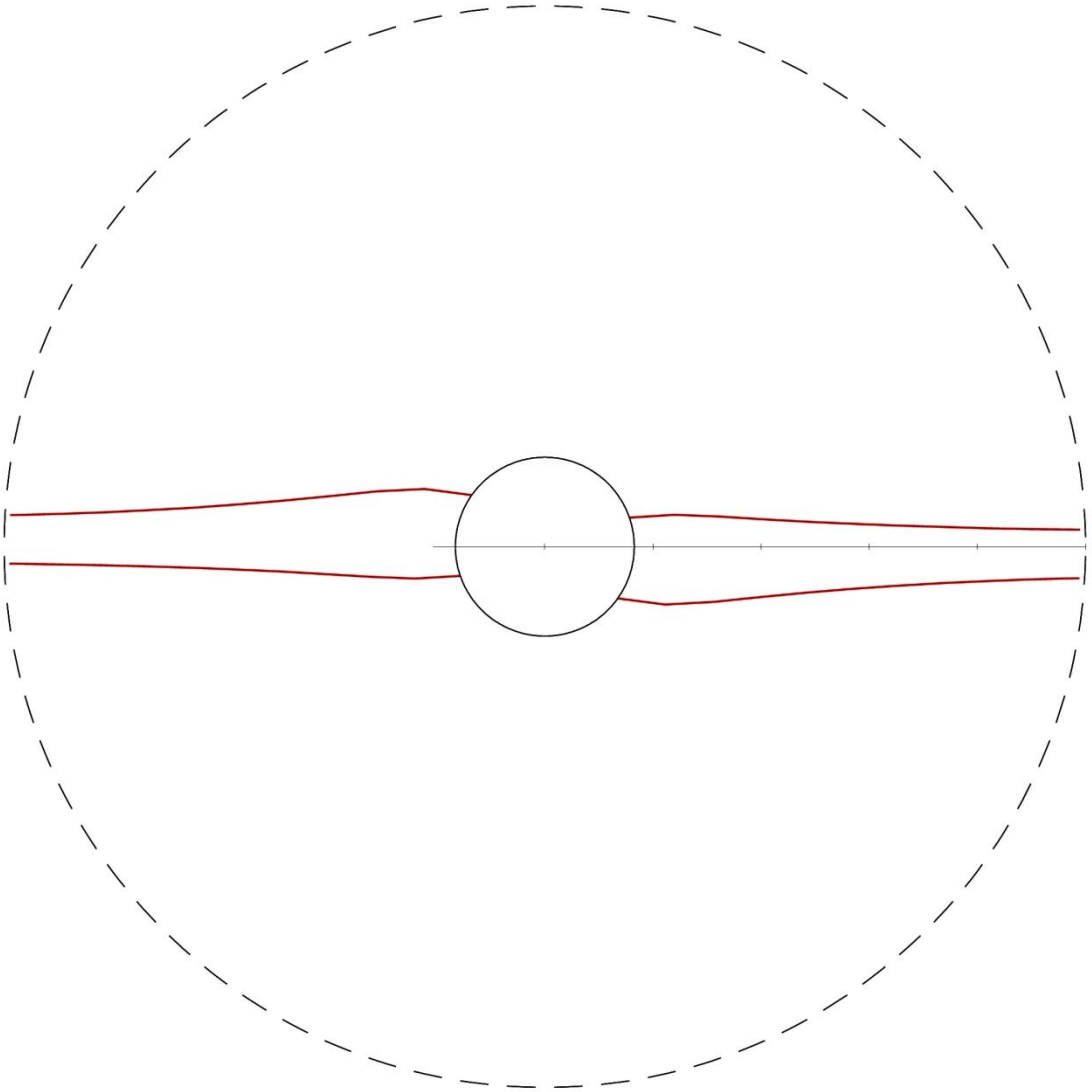

CRR-S3P3-NACA 2418-14-10-Dsk1

blds = 2	σ_{mean} = 0.0501	
Rtip = 0.1796	Ctip = 0.0168	β_{tip} = 15.97
Rhub = 0.0297	Chub = 0.0538	β_{hub} = 58.47
Rmean= 0.1287	Cmean= 0.0202	β_{mean} = 20.50
Adisk= 0.0985	Atip = 0.1013	β_{twist} = 42.50

Figure D.3: Frontal view and geometric data.

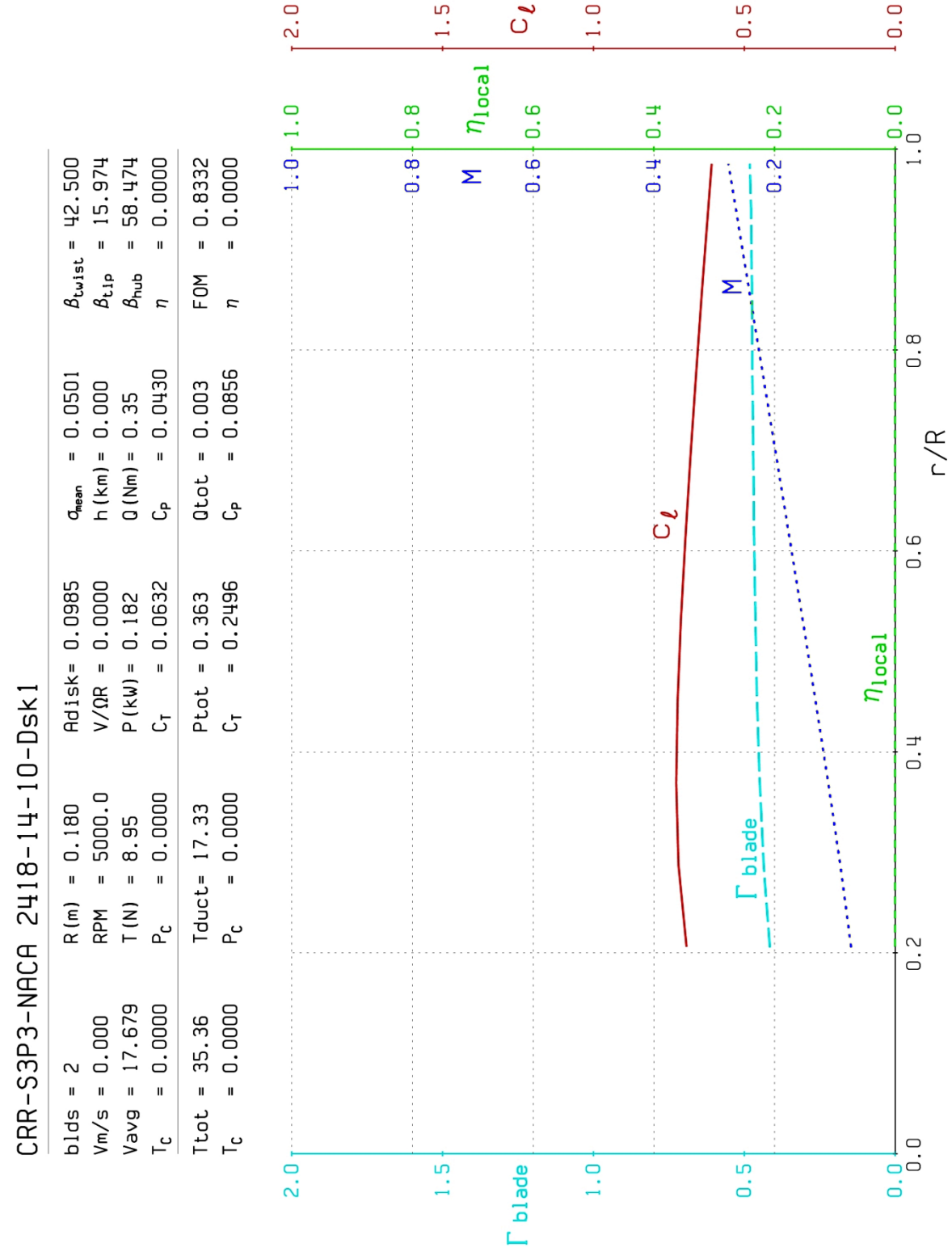

Figure D.4: Aerodynamic characteristics.

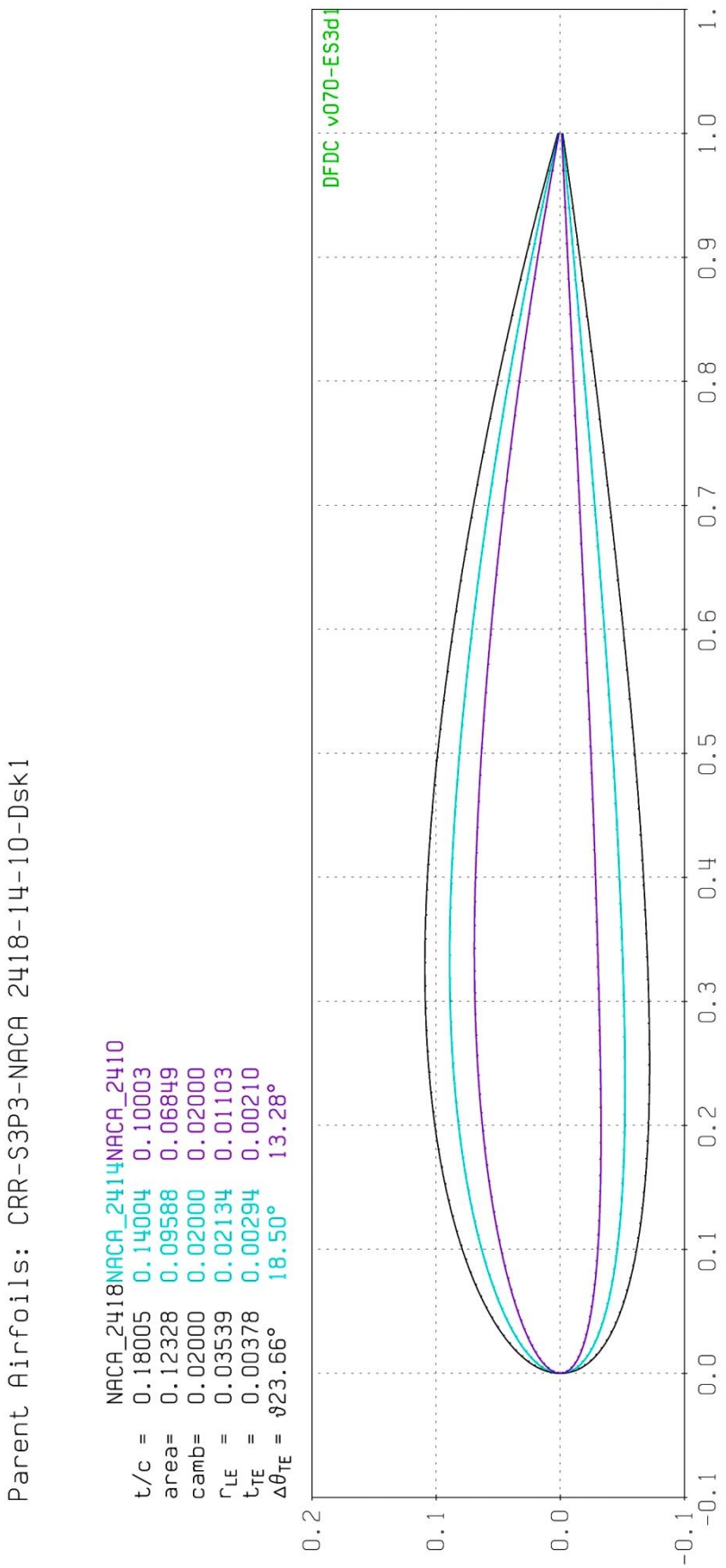

Figure D.5: Parent airfoils.

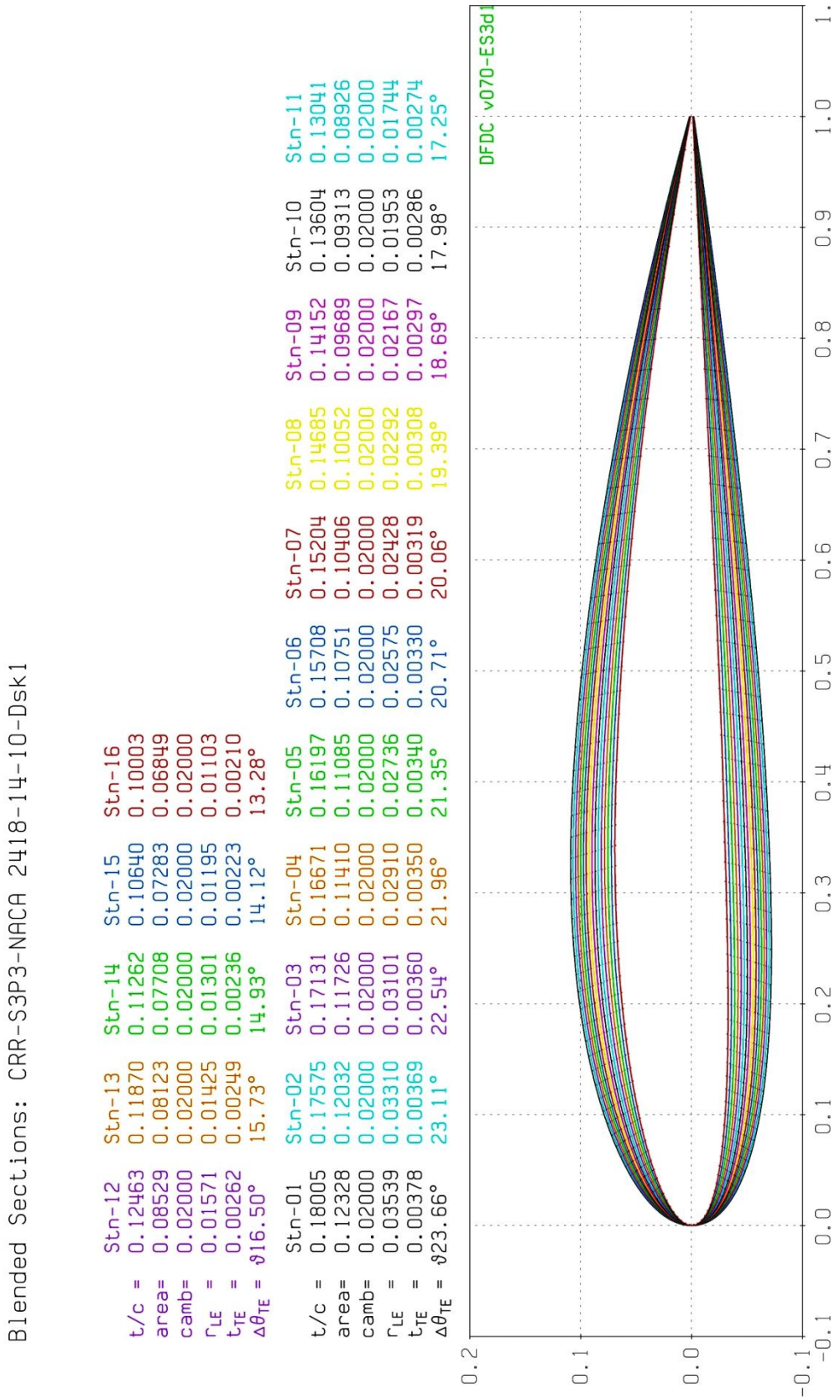

Figure D.6: Blended sections.

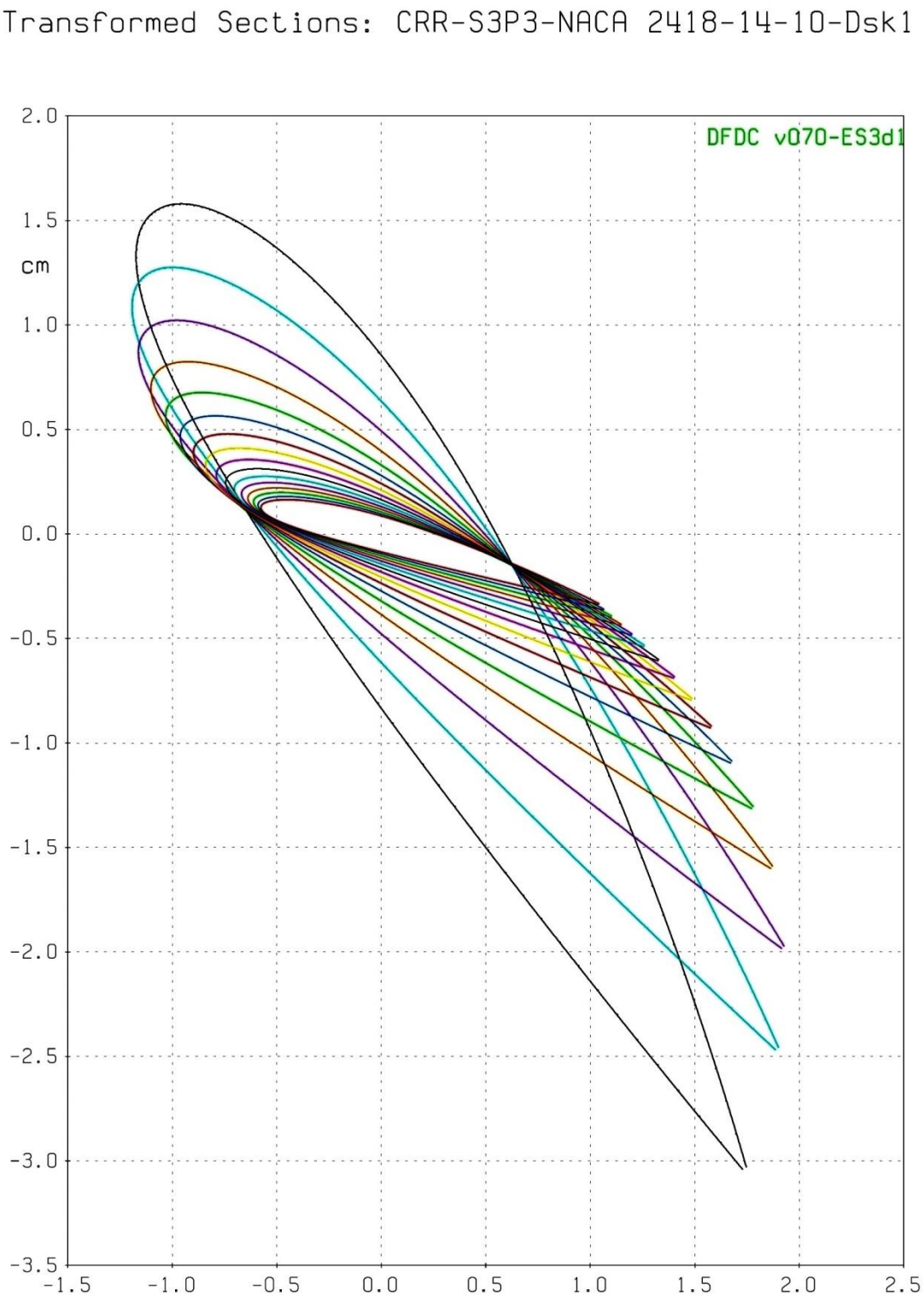

Figure D.7: Transformed sections.

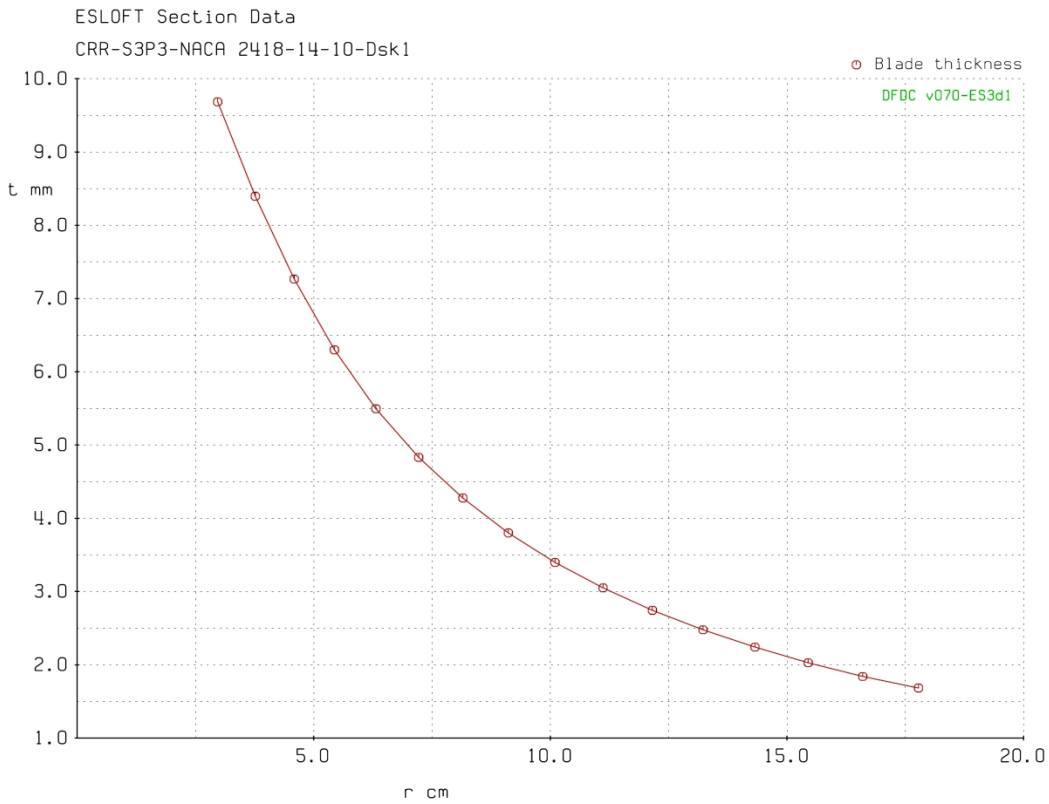

Figure D.8: Thickness distribution.

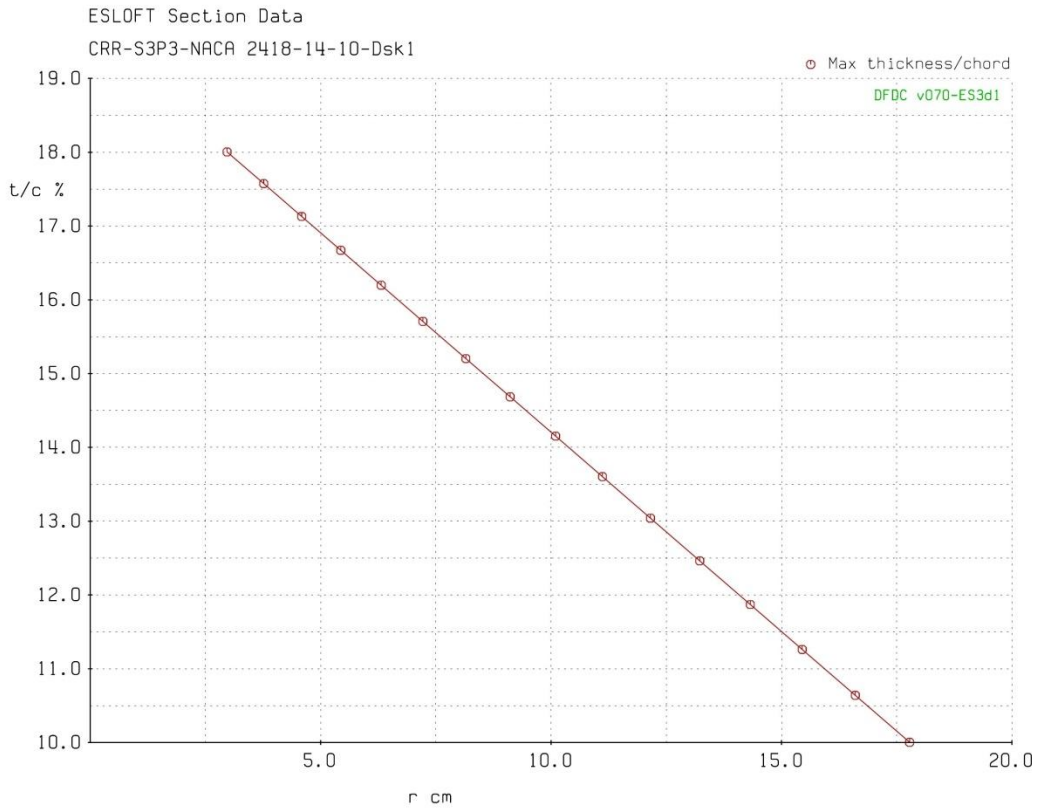

Figure D.9: Thickness/chord ratio.

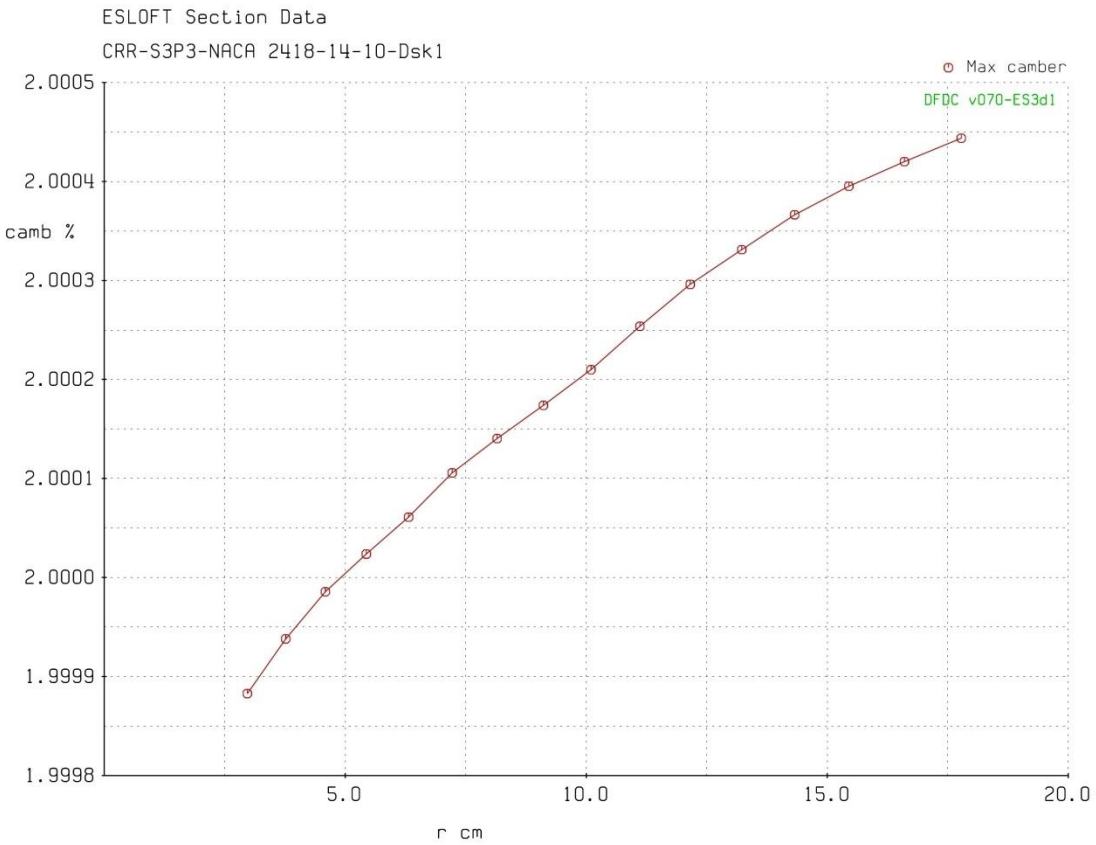

Figure D.10: Percentage camber.

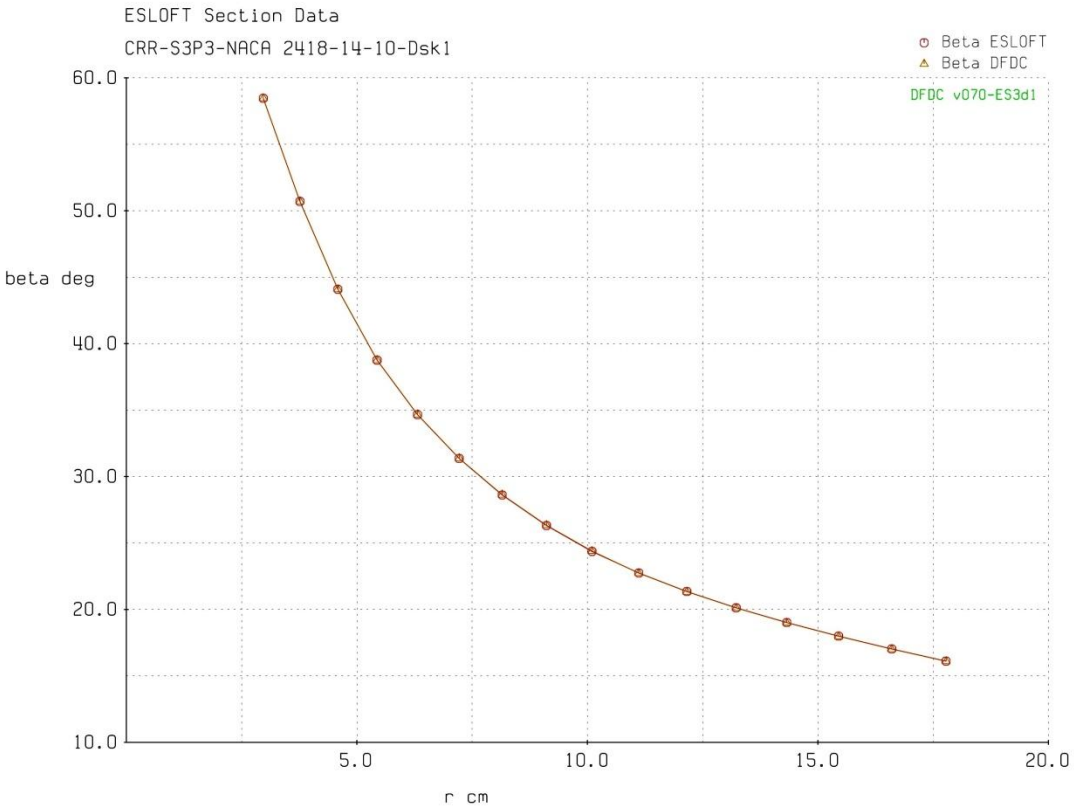

Figure D.11: Beta distribution.

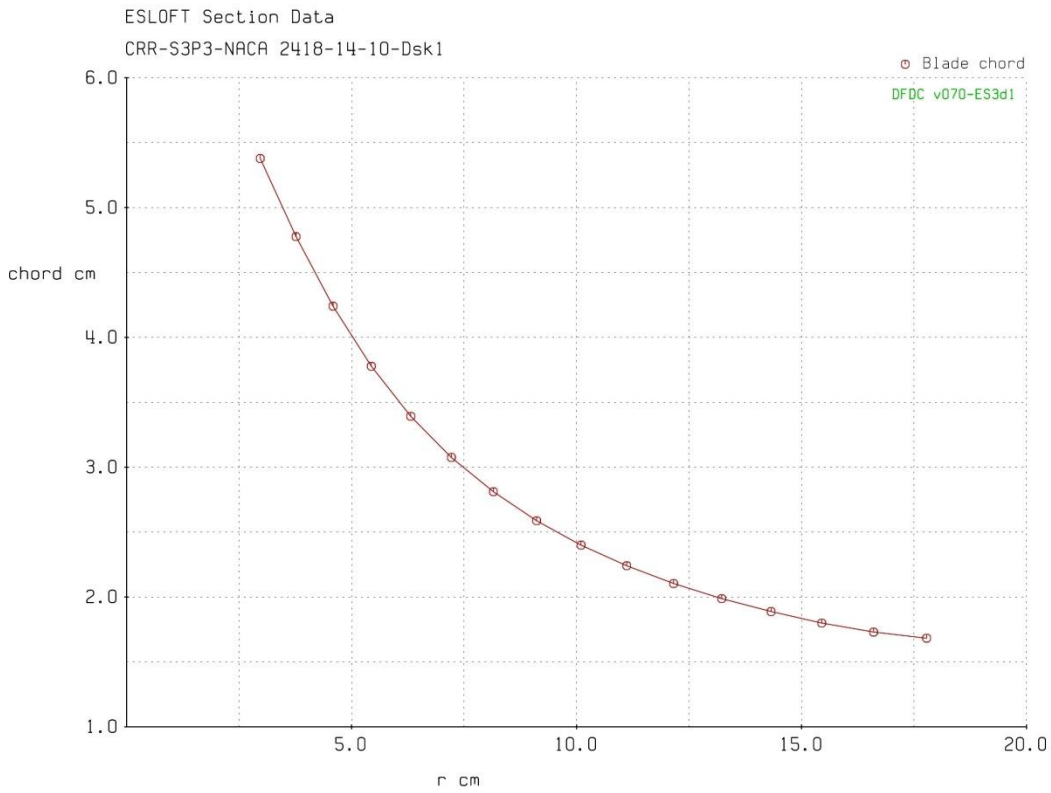

Figure D.12: Chord length distribution.